Computation of unsteady flow in turbomachinery

Wei Ning

University of Durham

School of Engineering

Computation of Unsteady Flow in Turbomachinery

Wei Ning

School of Engineering, University of Durham

A dissertation submitted for the degree of
Doctor of Philosophy

June 1998

Preface

This research programme is finally wrapped up and I have enjoyed most of time of about 3 years at Durham and two summers at European Gas Turbines, Lincoln. Although this thesis represents original work by myself, I have had many help and guidance from other people during the course of this study.

I would like first to thank my supervisor and friend, Li He. I am so fortunate to have him as my supervisor. My thanks are not only for his very constructive and sometimes very critical supervision on this work, but also the way he guided me to look at complex engineering problems. Surely I will benefit from his influence for my future career. I also appreciate all his time reading and commenting on this thesis.

I would like to mention some of my colleagues and friends, past and present: Dr Jerry Ismael, David Bell and Kenji Sato, I benefited from lively discussions with them on CFD and fluid mechanics; David Sims-Williams and Mark Tindale, who spent several nights digging out English errors in my thesis.

During this journey, I have always had love and encouragement from my family, especially from my wife, Chunlian Han. I am deeply indebted to them.

This research was sponsored by European Gas Turbines. I wish to acknowledge Roger Wells and Yansheng Li for many helpful discussions. Additional funding for this project was from ORS Award to me.

Abstract

Unsteady flow analysis has been gradually introduced in turbomachinery design systems to improve machine performance and structural integrity. A project on computation of unsteady flows in turbomachinery has been carried out.

A quasi 3-D time-linearized Euler/Navier-Stokes method has been developed for unsteady flows induced by the blade oscillation and unsteady incoming wakes. In this method, the unsteady flow is decomposed into a steady flow plus a harmonically varying unsteady perturbation. The coefficients of the linear perturbation equation are formed from steady flow solutions. A pseudo-time is introduced to make both the steady flow equation and the linear unsteady perturbation equation time-independent. The 4-stage Runge-Kutta time-marching scheme is implemented for the temporal integration and a cell-vertex scheme is used for the spatial discretization. A 1-D/2-D nonreflecting boundary condition is applied to prevent spurious reflections of outgoing waves when solving the perturbation equations. The viscosity in the unsteady Navier-Stokes perturbation equation is frozen to its steady value. The present time-linearized Euler/Navier-Stokes method has been extensively validated against other well-developed linear methods, nonlinear time-marching methods and experimental data.

Based upon the time-linearized method, a novel quasi 3-D nonlinear harmonic Euler/Navier-Stokes method has been developed. In this method, the unsteady flow is divided into a time-averaged flow plus an unsteady perturbation. Time-averaging produces extra nonlinear "unsteady stress" terms in the time-averaged equations and these extra terms are evaluated from unsteady perturbations. Unsteady perturbations are obtained by solving a first order harmonic perturbation equation, while the coefficients of the perturbation equation are formed from time-averaged solutions. A strong coupling procedure is applied to solve the time-averaged equation and the unsteady perturbation equation simultaneously in a pseudo-time domain. An approximate approach is used to linearize the pressure sensors in artificial smoothing

terms in order to handle the strong nonlinearity induced by the large amplitude of shock wave oscillation. The effectiveness of the present nonlinear harmonic method to include the nonlinear effects has been consistently demonstrated by calculations of unsteady transonic flows. The limitation of the nonlinear harmonic method has also been observed in calculations.

Some numerical efforts have been made to investigate trailing edge vortex shedding. The main issue which has been clarified is that a time-independent vortex shedding solution can be achieved by solving time-averaged equations with "unsteady stress" terms. The effectiveness of the unsteady stresses to suppress vortex shedding has been clearly demonstrated. Importantly, the time-independent solution is very close to the time-averaged solution which is generated from unsteady calculations of vortex shedding. The unsteady stresses in this investigation are worked out from vortex shedding unsteady solutions produced by a multi-block Navier-Stokes solver. The characteristics of the unsteady stresses have been analyzed. In this investigation, vortex shedding from a circular cylinder and a VKI turbine blade have been considered.

Contents

Nomenclature

Roman Symbols

A	Computational volume area; Amplitude; Channel height
A_{inlet}	Channel inlet height
C	Blade chord
C_p	Gas constant
c	Local sound speed
c_p	Pressure coefficient
c_f	Skin friction coefficient
c_1	Amplitude of entropy wave
c_2	Amplitude of vorticity wave
c_3	Amplitude of downstream running pressure wave
c_4	Amplitude of upstream running pressure wave
D	Blade trailing edge thickness; Circular cylinder radius; 4th order artificial smoothing
d	2nd order artificial smoothing
d_{lim}	Limit value of turbulence mixing length
e	fluid internal energy
F	Flux vector in x direction
f	Physical frequency
G	Flux vector in y direction
h	Streamtube height
h^*	throat height of diffuser
i	flow incidence angle
k	Reduced frequency; coefficient of heat conductivity; artificial smoothing coefficient
L	Reference length

M	Mach number
N_b	Blade numbers
n	wave numbers
P	pressure
r	Radius
Re	Reynolds number
S	Source term vector
St	Strouhal number
T	Temperature
t	Time
t'	Pseudo time
U	Reference velocity; Conservative variable vector
u	Velocity in x direction
u_g	Grid moving velocity in x direction
V	Viscous term vector
v	Velocity in y direction
v_g	Grid moving velocity in y direction
w	Relative velocity
x	Axial coordinate
y	Tangential coordinate
Y_{p1}, Y_{p2}	Blade or incoming wake pitch

Greek Symbols

ε	A small nondimensional parameter
ϕ	Phase angle
γ	Specific heat ratio; Stagger angle
κ	Von Karman constant

λ	Wave length
μ	Total viscosity
μ_l	Laminar viscosity
μ_t	Turbulence viscosity
ν	Dynamic viscosity
ρ	Density
σ	Inter-blade phase angle
δ^*	Boundary layer displacement thickness
ω	Angular frequency; Vorticity

Subscript

x	Variables in x direction
y	Variables in y direction
inl	Variable at inlet
exit	Variable at exit
i,j	Variable at grid point (i,j)
real	Real part of complex number
imag	Imaginary part of complex number
ref	Reference quantity
out	Variable at outlet
wake	Variable in a wake

Superscript

$\overline{(\cdot)}$	Time-averaged quantity
$(\ )'$	Unsteady perturbation
$\hat{(\ )}$	Steady-state quantity

$(\tilde{\ })$ Unsteady amplitude in complex number

Chapter 1. INTRODUCTION

1.1 Unsteady Flows in Turbomachinery

Unsteady flow is a natural phenomenon in a multistage turbomachine. The unsteadiness can be produced for different reasons, the major sources of unsteadiness in an axial flow turbomachine stage are depicted in Fig.1-1.

Firstly, the flow is inherently unsteady in a gas turbine machine due to the relative motion of adjacent stators and rotors. This unsteadiness is essential for a machine to do work on a fluid to increase its total enthalpy (Dean, 1959). Unfortunately, this stator/rotor interaction also produces aerodynamic loss, and undesirable aeroelastic and aeroacoustic consequences, such as blade vibration and noise. The bladerow interaction has two sides, wake/bladerow interaction and potential interaction. Wake/bladerow interaction is induced by the upstream fixed/rotating wakes chopped by a rotor/stator. The potential interaction is caused by the local bladerow sensing the nonuniform pressure fields in neighbouring bladerows. These two kinds of interactions become stronger as the gaps between bladerows are made smaller, consequently this produces a larger unsteady force on the blades. The demand for lighter and shorter engines causes a continuous reduction in the gaps between the bladerows. Currently, the study of unsteady flows induced by bladerow interactions are attracting many engineers and researchers.

Blade vibrations can also produce unsteady flows in a turbomachine. The vibration problems have received intensive attention in design procedures because of their dangerous potential to cause a blade or even whole engine failure. Aerodynamically induced blade vibration has two kinds: flutter and forced vibrations. Flutter is an aeroelastic instability, that once initiated cannot be stopped in most circumstances. Of all the problems that may cause blade failures, flutter is perhaps the most serious one. It is widely accepted that the turbomachinery blade flutter tends to

be a single-mode phenomenon, unlike the wing flutter in which different modes (bending and torsion) couple together. In an engine operation, the blades sometimes vibrate in their natural mode, which causes unsteady flows around the blades. If the unsteady flow does work on the blade, the amplitude of blade vibration will increase rapidly, and flutter then occurs. The occurrence of flutter can be judged based on whether the unsteady flow around the blade is doing work or damping the blade vibration. This is called the Energy Method. In this method, the objective is to predict the aerodynamic work or damping on the blade which is caused by the unsteady aerodynamic flows around oscillating blades. However, the coupling between different structural modes and aerodynamic forces in blade flutter can not be ruled out in modern designs where the blade tends to be thinner and more highly loaded. In modern axial fans and compressors, flutter can occur over a wide range of operation conditions, Figure 1.2 gives a guide to several regions on a axial-flow compressor map which are vulnerable to different types of flutter. This guide is evolved from engineering experience and understanding of the blade flutter. The aerodynamically forced blade vibration is caused by the unsteady nonuniform flows in the bladerow induced by the wake/bladerow/potential interactions, inlet distortion, rotating stall, and surge etc. In recent years, although considerable progress towards understanding blade vibrations has been made, efficiently and accurately predicting flutter boundaries and blade forced vibrations is still a challenging task because of the complexity of the unsteady flow environment.

Trailing edge vortex shedding is another major unsteadiness in turbomachinery when viscous flow passes a blunt blade trailing edge. This unsteadiness is particularly pronounced in turbines where a very thick trailing edge for turbine airfoils is needed to accommodate the blade cooling passages. Some experimental works (McCormick, Paterson and Weingold, 1988, Roberts and Denton, 1996, Gostelow and Solomon, 1996) suggest that the wake loss in a turbine is largely due to the formation of a vortex street. Denton (1993) estimates that wake loss is typically about 1/3 of the profile loss in gas turbines. Unfortunately the detailed mechanism of vortex shedding

loss production is still not quite clear. One observation is that, when vortex shedding occurs, the static pressure just downstream of the trailing edge (base region) is usually lower than that in the freestream, producing a base pressure loss. Predicting the base pressure is an important part of predicting the loss produced by the vortex shedding. Because vortex shedding in turbomachines has a small length scale and high frequency, the experimental and numerical investigations are difficult and expensive. However, understanding and predicting trailing edge vortex shedding is important to further reduce the total loss in a turbine design and is receiving more and more attention. A thorough review of experimental studies of trailing edge vortex shedding in turbomachniey is provided by a recent publication by Cicatelli and Sieverding (1995).

In turbomachinery, unsteady flows can also arise from other sources, such as rotating stall, surge, and shock/boundary layer interaction etc. The present study in this thesis is concentrated on the unsteady flows induced by blade oscillation and trailing edge vortex shedding, and is confined to purely numerical investigations.

1.2 Aspects of Unsteady Flows in Turbomachinery

1.2.1 Reduced Frequency

Among all the parameters for describing the unsteady flows in turbomachinery, the reduced frequency k is probably the most important one. It is defined as

$$k = \frac{\omega L}{U} \tag{1-1}$$

where $\omega = 2\pi f$ and f (Hz) is the physical frequency of the unsteadiness. U is a reference velocity, usually taken as the inlet velocity. L is a reference length scale. For

blade flutter problems, L is usually taken to be the blade chord length, on some occasions L is taken to be the blade semi-chord (0.5C). For bladerow interactions, L is taken to be blade chord length or blade pitch length. The reduced frequency can be interpreted as the ratio of the time taken for a fluid particle to flow past the length of a blade chord or pitch to the time taken for the flow to execute a cycle of unsteadiness. For small values of the reduced frequency, the flow is quasi-steady, while for large values, unsteady effects dominate. The value of the reduced frequency is an indicator of the temporal and spatial length scales of the unsteadiness.

In the early stages of a blade design, the reduced frequency is used as a criterion for avoiding the occurrence of the blade flutter. For the first bending mode, the design value of the reduced frequency usually should be bigger than 1.0, and for the first torsion mode, it usually should be above 1.5. For the unsteady flow induced by the blade oscillation, the time scale of the unsteadiness is decided by the blade oscillating frequency, the length scale is usually taken to be the blade chord length.

For the unsteady flow induced by bladerow interactions, the reduced frequency is normally one order magnitude larger than the reduced frequency of the blade flutter. The time scale of the unsteadiness in bladerow interactions is decided by the blade passing frequency, and the length scale is approximately the blade pitch or chord.

For trailing edge vortex shedding, the Strouhal number (St) is used to determines the unsteady flow instead of the reduced frequency. The Strouhal number is defined as

$$St = \frac{fD}{U} \tag{1-2}$$

The physical meaning of the Strouhal number is the same as the reduced frequency. The length scale for the vortex shedding is the blade trailing edge thickness which is

much smaller than the blade chord or blade pitch. The very small length scale determines that a fine mesh is required to resolve the trailing edge vortex shedding. The Strouhal numbers for flows over cylinders are constant (0.18~0.2) over a wide range of Reynolds number. The Strouhal numbers of turbomachinery flows are strongly dependent on flow conditions and the blade geometry (Cicatelli and Sieverding, 1995).

1.2.2 Inter-Blade Phase Angle

The concept of the Inter-Blade Phase Angle (IBPA) was first introduced by Lane (1956) in the field of turbomachinery aeroelasticity. For a blade flutter problem in a well-defined travelling wave mode, Lane proposed that all the blades vibrate in the same mode (bending or torsion, or those two combined) and same amplitude with a phase difference between neighbouring blades. This phase difference is called the Inter-Blade Phase Angle (IBPA). This concept is now widely accepted. The possible values of the inter-blade phase angle in a flutter analysis are defined by

$$\sigma = \frac{2\pi n}{N_b} \tag{1-3}$$

where N_b is the number of blades and n represents the wave number (n = 1,2... N_b). For a single blade passage as depicted in Fig. 1-3, the steady flow variables on the upper periodic boundary *ab* are identical to those on the lower boundary *cd*. For unsteady flows induced by blade oscillating, the amplitudes of flow variables are still identical on both the upper and lower periodic boundaries, but there is a phase difference between the upper and lower periodic boundaries. The value of this phase difference is the inter-blade phase angle. Due to the inter-blade phase angle, for an unsteady flow calculation in turbomachinery, a phase-shifted periodic boundary condition has to be applied when the calculation is carried out on a single blade

passage domain, or the unsteady calculation has to be carried out on a multiple blade passage domain.

Although the inter-blade phase angle was originally introduced for blade flutter problems, this concept can also be used to describe the unsteady flows induced by bladerow interactions(He, 1996a). For the bladerow interaction, the inter-blade phase angle is decided by the pitch ratio of neighbouring bladerows. For example, for a single compressor stage as depicted in Fig. 1-4, the reference blade row has a blade pitch Y_{p1}, the upstream neighbouring bladerow has a blade pitch Y_{p2}. Assuming that the upstream neighbouring bladerow is moving at a relative speed ωr, the inter-blade phase angle between the upper periodic boundary and lower periodic boundary is:

$$\sigma = 2\pi(1 - \frac{Y_{p1}}{Y_{p2}}) \qquad (1\text{-}4)$$

Usually the neighbouring bladerows have different blade numbers which results in non-zero inter-blade phase angles. Therefore the unsteady flow calculation for the bladerow interaction problem has to be carried out on a multiple blade passage domain, or shifted periodic boundary conditions have to be applied if the calculation is carried out on a single blade passage domain. The inter-blade phase angle in a wake/rotor or potential/bladerow problem can also be worked out by the formulation (1-4).

1.3 Advance of Numerical Methods for Unsteady Flows in Turbomachinery

In the last two decades, the development and application of numerical methods for steady flow analysis has made an enormous impact on the design of all types of turbomachines, from transonic axial fans to low speed centrifugal pumps.

The steady flow solver now has an important role in the toolkit of turbomachine designers. However, because of the unsteady nature of turbomachinery flows, introducing unsteady analysis in the design system is the key to further improve the aerodynamic performance and structural integrity of turbomachines. In recent years, considerable efforts have been made on the numerical calculation of unsteady flows in turbomachinery thanks to the significant advance of computer power and computational techniques.

1.3.1 Nonlinear Time-Marching Methods

The time-marching method is a revolutionary invention by Moretti and Abbett (1966) for the solution of transonic flow problems. Since then, a huge variety of numerical schemes based on the time-marching concept have been developed for solving steady transonic inviscid and viscous external and internal flows. Nowadays, time-marching methods are among the most popular numerical methods used in the turbomachinery design system for steady flow analysis in isolated and multiple blade row environments. Notable works were those by Denton (1982, 1990), Dawes (1988), and Ni (1989).

The time-marching method has been able to be used for unsteady flow calculation from its birth. The extension from a well-developed steady solver to an unsteady one is not a daunting task for an experienced CFD developer. In an unsteady time-marching calculation, the time domain has a real meaning in which the unsteady or time-dependent solution is marched. For a periodic unsteady flow, such as the unsteady flow induced by bladerow interaction or blade vibration, the solution must be stepped through many cycles of the transient solution until a periodic solution is reached. Usually, the time-marching unsteady calculation is much more CPU time consuming than its steady counterpart. The high computational cost severely constrains applications of unsteady flow analysis in turbomachinery designs. Nevertheless, significant development of time-marching methods for unsteady

turbomachine flows has been made in last two decades. This section is dedicated to reviewing the advance of the unsteady time-marching methods in three areas: bladerow interactions, flutter, and trailing edge vortex shedding. The term 'nonlinear' in the title of this section is used to be distinct from the linear methods. The nonlinearity of the unsteady flow is naturally included in the time-marching unsteady solutions by directly solving the nonlinear Euler/Navier-Stokes equations.

1.3.1.1 Bladerow Interactions

The numerical simulation of bladerow interactions was the earliest motivation driving the development of unsteady CFD methods in turbomachinery. In the time-marching unsteady calculation of bladerow interactions, a key constraint to the computational efficiency is the treatment of periodic boundaries. In a steady flow calculation, the simple repeating periodic condition is applied by equating flow variables at the lower and upper periodic boundaries in a single blade-blade passage domain. For an unsteady flow calculation of the bladerow interaction, the simple repeating periodic condition no longer exists in a single passage calculation due to non-zero inter-blade phase angles. One either has to carry out an unsteady calculation on a multiple passage domain which will significantly increase the computation time, or implement a phase-shifted periodic boundary condition in a single passage calculation. As far as the computational efficiency is concerned, it is desirable to carry out the unsteady flow calculation in a single passage domain. Therefore, developing phase-shifted periodic boundaries has played an important role in the development of time-marching unsteady methods in turbomachinery.

A milestone work on unsteady flow calculation by using the time-marching method in turbomachinery was made by Erdos et al (1977). In this work, the MacCormack(1969) predictor-corrector finite difference scheme was implemented to solve the 2-D Euler unsteady equations for calculating the unsteady flows in a fan stage. The first phase-shifted periodic boundary condition, the "Direct Store" method,

was proposed to make the unsteady flow calculation possible in a single blade passage. In this method, flow parameters on the periodic boundaries are stored at each time step in one unsteady period to update the solutions at the next corresponding period. This method was later extended by Koya and Kotake (1985) to a three-dimensional calculation of inviscid unsteady flow through a turbine stage. The main drawback of this "Direct Store" method is that a large computer storage is required in an unsteady calculation. This disadvantage is severe for three-dimensional viscous unsteady calculations, particularly for low frequency problems such as blade flutter. Furthermore, the solution by using "Direct Store" method has a slow convergence rate to get a final periodic solution because the solution procedure is heavily influenced by the flow initial guess.

To avoid the complexity of phase-shifted periodic conditions, Rai (1985) developed a 2-D Navier-Stokes solver for the stator/rotor interaction. In this method, calculations were carried out in a simple stator/rotor pitch ratio (1:1 or 3:4) by modifying the configuration of the rotor in a turbine stage. So the simple repeating periodic boundary condition can be used in a calculation. A good comparison of time-averaged quantities between the calculation and experimental data was achieved. The calculated unsteady pressure amplitudes largely depended on how close the stator/rotor pitch ratio used in calculation correlated to the real pitch ratio. Rai (1987) later extended his techniques to a three-dimensional viscous calculation of bladerow interactions. However, the influence of blade configuration modifications on unsteady flows needs to be carefully clarified.

In 1988, a novel phase-shifted periodic boundary treatment, "Time-Inclined" method, was proposed by Giles (1988) in a wake/rotor interaction calculation. In this method, the flow governing equations are firstly transformed from the physical time domain to a computational time domain. The computational domain is inclined along the blade pitchwise direction according to the time lag between neighbouring blades. In the computational domain, a direct repeating periodic condition can be

implemented at the lower and upper periodic boundaries in a single blade passage. Compared to Erdo's "Direct Store" method, Gile's method does not need extra computer storage. Giles (1990a) also used this technique to calculate the bladerow interactions in a turbine stage, an unsteady shock system was captured in the calculation. A computer program UNSFLO was developed by Giles(1991a) based on the "Time-Inclined" method. This programme is capable of handling many kinds of two-dimensional unsteady flows in turbomachinery, such as wake/rotor interaction, potential interaction, and flutter. However, this "Time-Inclined" method also has limitations. First of all, the time-inclination angles of the computational plane are restricted by the domain-of-dependence restrictions of the governing equations. These angles are determined by the pitch ratio of rotor/stator in bladerow interaction problems and the inter-blade phase angle in flutter problems. The lower the unsteady frequency is, the more severe the restriction is. For low frequency problems, such as flutter and some forced response problems, the multiple blade passage calculation has to be carried out to relax this restriction, consequently the computation time will be increased significantly (He, 1990a). Secondly, Gile's method was originally developed for inviscid flow calculations, but for viscous calculations, some simplifications have to be made in the space-time coordinate transformation. These simplifications can be justified for high Reynolds number flows (Giles, 1991a), for low Reynolds number flows, the validity needs to be justified.

It should be noted that both the "Direct Store" and the "Time-Inclined" methods can only handle a single frequency unsteadiness. They are not suitable for an unsteady flow calculation in a multi-stage environment because multiple frequencies are usually involved.

During the development of the methods for phase-shifted periodic conditions, other efforts have also been made to improve the computational efficiency of time-accurate unsteady calculations. One approach is to develop efficient time-marching implicit schemes in which a much larger time-step can be used compared to the

explicit schemes, some contributions are from works by Rai (1985), Krouthen and Giles (1988), and Coperhaver, Puterbauch and Hah (1993). Another is to use effective multigrid techniques, He (1993) developed a time-consistent two-grid method which can considerably speed up the convergence of unsteady calculations. This two-grid acceleration technique was successfully used by some researchers in a time-marching unsteady calculation for bladerow interactions (Jung, A. R. et al 1997). A recent advance in the use of multigrid in unsteady flow calculations in turbomachinery was achieved by Arnone (1996), in which an efficient time-accurate integration scheme proposed by Jameson (1991) was used. In this new scheme, a dual time-stepping in the physical time-domain and a non-physical time-domain is introduced. In the physical time-marching, an implicit scheme is used. In the non-physical time-marching, any efficient accelerating techniques which are widely used in steady calculations can be used to speed up the calculation, such as local time step, multigrid, implicit residual smoothing. Although significant progress has been made to make time-marching unsteady calculations more efficient in recent years, an unsteady calculation still needs weeks running on a powerful workstation (Gundy-Burlet and Dorney, 1997). This high computational cost hinders the application of time-marching unsteady analysis in a routine turbomachine design system.

As an alternative to the direct unsteady flow calculation, Adamczyk (1985) proposed a notable concept of modelling unsteady effects by solving an "average-passage" Navier-Stokes equation system. In this system, different averaging strategies were used to average out the unsteady effects due to random flow fluctuations (due to turbulence) and periodic flow fluctuations due to the bladerow interaction. The attraction of this concept is that solving an unsteady problem is replaced by simply solving a set of averaged equations. The averaged equations can be solved by any efficient steady flow solver, while the unsteady effects are included in a time-averaged solution. The difficulty in doing so is that averaging produces unknown "deterministic stress" terms in the averaged equations due to the nonlinearity of the original Navier-Stokes/Euler equations. Extra closure models are required to work

out all "deterministic stress" terms, similar to the turbulence models for modelling the Reynolds stress terms in the Reynolds averaged Navier-Stokes equations. Nevertheless, Adamczyk's concept has stimulated many research activities in turbomachniery unsteady CFD and some numerical methods have been developed (Celestina et al, 1986, Adamczyk et al, 1989, Rhie et al, 1995, Hall, 1997). However, all deterministic stress models so far have not been sufficiently practical, and the development in this area is expected to go further in the near future.

1.3.1.2 Flutter

As for bladerow interaction calculations, periodic boundary treatment is also a difficulty in unsteady flow calculations for blade flutter analysis. For flutter analysis, one has to calculate unsteady flows under all possible IBPAs to find the least stable one. For a non-zero inter blade phase angle, phase-shifted periodic boundary conditions have to be applied if the unsteady calculation is carried out in a single blade passage domain. Because of the large number of repeated calculations in the flutter analysis, there is a stringent requirement for computational efficiency.

The development of time-marching methods for blade flutter analysis in turbomachinery started in the 1980s with a pioneering effort made by Pandolfi (1980) using a finite difference scheme to compute two-dimensional unsteady subsonic flows around vibrating blades with the same phase. Later Pandolfi's work was extended by Fransson and Pandolfi (1986) using the "Direct Store" method to deal with non-zero inter-blade phase angles. A similar attempt was also made by Joubert (1984) and later it was extended by Gerolymos (1988) to a first fully three-dimensional unsteady inviscid flow analysis for flutter predictions. Because of the huge demand for computer storage by using the " Direct Store" method for low frequency flutter problems, the application of these time-marching methods was severely constricted. Although Giles (1991b) extended his "time-inclined" phase-shifted periodic conditions for blade flutter analysis, a multiple blade passage calculation usually has to be carried

out due to the strong restriction of inter-blade phase angles in the space-time coordinate transformation (He, 1990a).

To deal with the phase-shifted periodic boundary condition more flexibly, a "Shape Correction" method was proposed by He (1990b) in a 2-D time-marching solver for unsteady flows around oscillating blades. In this novel method, the periodic unsteady flow variables on the periodic boundaries are transformed into Fourier components by using a Fourier transformation. Compared with the " Direct Store" method, the computer storage is greatly reduced by only storing the Fourier coefficients. This method also overcomes the restriction of inter-blade phase angles in the "Time-Inclined" method. Furthermore, the "Shape Correction" method was later developed by He (1992) to be able to handle multiple perturbations with a single blade passage solution. He (1994a) later extended the 2-D method to a fully three-dimensional time-marching method for inviscid and viscous unsteady flows around vibrating blades. The 3-D unsteady viscous solutions were considerably accelerated by a two-grid time integration technique developed by He (1993a).

Due to the potential importance of the fluid and structure interaction for blade flutter, the time-marching methods are also used by many researchers for developing coupling methods for blade flutter analyses (Bendiksen, 1991, He, 1994, Marshall and Imregun, 1995, Chew et al, 1997). In the coupling method, both the nonlinear aerodynamic equations and the structural equations are solved by the time-marching schemes, at each time-step the data are transferred between the aerodynamic model and the structural model. The inter-blade phase angle at which the instability occurs in the coupling methods is a part of the solution, therefore the calculations are normally carried out on a multi-passage domain or ideally on a whole annulus. The drawback of the coupling methods is the computational cost, not only due to the time-marching but also to the coupling between the aerodynamic model and the structural model at each time-step.

Although the application of time-marching methods for flutter analysis is severely restricted by its large CPU time consumption, the active research activities in this sector have significantly improved the physical understanding of blade flutter. For example, the works by He (1990b) and Ayer and Verdon (1996) revealed the potential importance of the nonlinearity in the flutter analysis due to shock oscillation. To handle unsteady flows with strong nonlinearity, the nonlinear time-marching methods plays an irreplaceable role. Furthermore, the well-developed time-marching solvers provide reliable tools for the validation of other kinds of numerical methods, such as time-linearized methods which will be reviewed later in this Chapter.

1.3.1.3 Trailing Edge Vortex Shedding

Although trailing edge vortex shedding is an important part of blade profile loss in gas turbines, very few efforts have so far been made to predict vortex shedding in turbomachinery using numerical methods. Currently, the most popular methods for the prediction of the trailing edge loss are based on analytical models, such as the control volume analysis by Denton (1993). However, the base pressure is not calculable in the control volume method, therefore the loss due to the trailing edge vortex shedding is unlikely to be correctly predicted (Roberts, 1997). There are two main difficulties that are hindering the development of numerical methods for vortex shedding calculations by solving the unsteady Navier-Stokes equations. The first is the large number of mesh points required around the trailing edge to resolve the small length scale vortex shedding, which makes the computation prohibitively expensive. The second is the fact that vortex shedding is a highly non-isotropic phenomenon, the conventional turbulence models such as the mixing length and two-equation models are unlikely to predict the wake evolution (Cicatelli and Sieverding, 1995) correctly. Although applications of some sophisticated turbulence models such as Reynolds stress models and Large-Eddy Simulation models (LES) have demonstrated their ability to capture the wake mixing process, these models are unfortunately not feasible to be used yet.

For numerical calculations of trailing edge vortex shedding by using time-marching methods, an impressive work was done by Currie and Carscallen (1996). In this work, quasi-3D Reynolds averaged Navier-Stokes equations are solved by using a flux-difference splitting scheme of Roe(1981) in space and an implicit integration scheme in time, an extremely fine adaptive unstructured mesh near the blade surface and in the wake was used to resolve the boundary layer and the vortex shedding in the wake. A combination of $k-\omega$ and $k-\varepsilon$ turbulence zonal models (Menter, 1993) was used to model the turbulence. The vortex shedding structures and frequencies were very well predicted by the calculations under transonic flow conditions. The measured total pressure loss coefficients were reasonably predicted by calculations. However, the base pressures were poorly predicted, especially at the flow condition with an exit Mach number of 1.0. The excessive numerical dissipation in the calculations was blamed by the authors for the poor prediction of base pressures even in such a fine mesh.

A recent attempt at the numerical prediction of trailing edge vortex shedding was made by Arnone and Pacciani (1997). The vortex shedding behind a turbine blade, which was extensively tested (Cicatelli and Sieverding, 1996) at von Karman Institute(VKI), was numerically investigated. In the calculation, a simple two-layer mixing length turbulence model and the Baldwin-Lomax turbulence model (Baldwin and Lomax, 1978) were compared for the vortex shedding predictions. The authors found that the predicted shedding frequency and flow fluctuations can vary quite a lot by using different values of constant C_w in the Baldwin-Lomax models. This suggests that the unsteady calculation of trailing vortex shedding is sensitive to turbulence models. Another numerical effort by Roberts (1997) also found that vortex shedding predictions are strongly dependent on turbulence modelling. In the work by Arnone and Pacciani, although an efficient time-accurate integration scheme (Jameson, 1991) and a multigrid were used in their calculations, each 2-D calculation with 36,113 mesh points still took about **65** hours on an IBM 590 workstation to achieve a periodic vortex shedding. Although Currie and Carscallen (1996) did not

mention the computational time in the published paper, it is believed to be incredibly long.

Even if the arguments about the turbulence models are temporally excluded, the unsteady calculation of trailing edge vortex shedding is still unlikely to be used in turbomachine design systems because it is extremely CPU time consuming. However, the major concern of turbomachine designers with regard to vortex shedding is the loss produced by the vortex shedding, i.e. the time-averaged effects of the vortex shedding rather than its small scale unsteady details. It would be highly desirable to develop a numerical method which can produce a time independent ('steady' or time-averaged) solution in which the time-averaged vortex shedding effects can be included. It would be similar to Adamczyk's (1985) concept for handling bladerow interactions. The feasibility of this concept will be investigated in this thesis.

1.3.2 Time-Linearized Harmonic Methods

As an alternative to the nonlinear time-marching methods, the other kind of numerical methods widely used for unsteady flow analysis in turbomachinery, is the time-linearized harmonic method. In time-linearized harmonic methods, an unsteady flow is decomposed into a steady flow plus a linear, harmonically varying unsteady perturbation. The harmonic perturbation equation is a linear equation with coefficients based on the steady flow solution. Although the perturbation equation can only handle a single frequency unsteadiness in one solution, the more general solution can be linearly composed from the solution of different frequencies. The validity of the methods depends on the linearity of the unsteady flow problems. It is widely accepted that the onset of blade flutter is a linear aeroelastic phenomenon in most circumstances, therefore the time-linearized methods have been widely used for blade flutter analysis in turbomachinery.

The development of linearized methods for unsteady flows in turbomachinery started with the pioneering effort by Whitehead(1970) based on a flat plate analysis. In this analysis, the steady flow is assumed to be uniform and axially subsonic. The blade thickness and loading are neglected by using a flat plate cascade. The perturbation equation based on the uniform steady flow is solved by a semi-analytic method. Whitehead (1987) later developed this flat plate analysis into a well-known computer program LINSUB which can handle several kinds of unsteady inviscid flows around a flat plate cascade, i.e. wake/rotor and potential/rotor interactions and blade oscillation. The solution from LINSUB is extremely quick and accurate. Although its application is limited due to the flat plate and uniform steady flow assumptions, this method provides an invaluable tool to validate other numerical methods.

The second stage in the development of time-linearized methods is the development of time-linearized potential methods with notable works by Verdon and Caspar (1984), and Whitehead (1982). The important advance in this kind of method is that the steady flow is obtained by solving nonlinear potential equations and real airfoils can be dealt with in the analysis. The unsteady perturbation is firstly assumed to be harmonically varying and the linear superposition can be used for unsteady flows with different frequencies. To handle transonic flows, shock fitting techniques were used in Verdon and Caspar's methods, and a shock capturing technique was used in Whitehead's work. Engineering practice (Verdon and Caspar, 1984) has demonstrated that time-linearized potential methods are effective in predicting subsonic and some transonic flutters. The limitation of linearized potential methods is due to the isentropic and irrotational assumptions of potential flows, for transonic problems they are only suitable for flows with weak shocks.

A significant advance in the time-linearized methods has been made by the active development of time-linearized Euler methods in recent years. Actually, the time-linearized Euler method was firstly proposed by Ni (1974). An important idea in

Ni's work was to make the perturbation amplitude time dependent in a pseudo time, so the perturbation equation can be solved by a conventional steady time-marching method. Unfortunately the time-linearized method did not receive much attention until a recent development by Hall and Crawley (1989). In Hall and Crawley's work, the steady flow solution was obtained by solving the unsteady Euler equations and the linear harmonic Euler equations were solved by a finite element method. This work importantly demonstrated the validity of the linear approximation up to quite substantial levels of unsteadiness. In their work, a shock-fitting technique was used to handle oscillating shock waves in a transonic duct. Unfortunately shock fitting techniques are not practical due to the complex shock system in turbomachniery flows. It is preferable to use the flexible shock capturing techniques in the time-linearized methods. An important contribution was made by Linquist and Giles (1991) to show that shock capturing can be used in the time-linearized Euler methods to predict blade unsteady loading correctly provided that the time-marching scheme is conservative and the steady shock is sufficiently smeared. Since then the shock capturing technique has been widely used in the time-linearized Euler methods (Holmes and Chung, 1993, Hall, Clark and Lorence, 1994).

Currently the time-linearized methods are being actively developed in three aspects. The first is to develop the 2-D time-linearized Euler methods into fully three-dimensional methods (Giles, 1991b, Hall and Lorence, 1992, Marshall and Giles, 1997). The calculation results by Hall and Lorence (1992) have shown the three-dimensional effects can be significant for correctly predicting the blade loading. The second aspect is to extend the Euler methods to Navier-Stokes methods (Holmes and Lorence, 1997). The Navier-Stokes methods are more realistic for the flutter analysis, especially for the subsonic stall flutter prediction in which the oscillation of the flow separation region is the dominant phenomenon. The third area of interest is to include the interaction effects from other blade rows in a single bladerow calculation. A work by Buffum (1995) has shown the strong effects of the interaction from other bladerows on a blade flutter prediction produced by an isolated bladerow calculation.

Preliminary results from a recent study by Silkowski and Hall (1997) have shown that "the aerodynamic damping of a blade row in part of a multistage machine can be significantly different than that predicted using an isolated blade row model".

The main feature of the time-linearized methods is high computational efficiency. One reason is that, in the linearized methods a nonlinear unsteady equation is decomposed into two equations, i.e. a steady flow equation and a linearized perturbation equation. By introducing a pseudo-time technique, the time-linearized Euler/Navier-Stokes perturbation equations can be solved by using any well-developed time-marching schemes. Another reason is that the phase-shifted periodic condition is no longer a difficulty and the solution can be easily realised in a single blade passage domain. However, although the time-linearized analyses meet the needs of turbomachinery designers for efficient unsteady flow predictions, their limitation should not be underestimated. The drawback of the time-linearized methods is that nonlinear effects are completely neglected due to the linear assumption . The nonlinear effects can be potentially important in turbomachniery unsteady flows associated with the shock oscillation, finite amplitude excitation, flow separation etc.

1.3.3 Nonlinear Harmonic Methodology

The strength of the nonlinearity of unsteady flows is represented by the difference between the steady flow and the time-averaged flow (He, 1996a). A typical nonlinear example is a shock oscillating in a transonic duct as shown in Fig.1-5, the time-averaged shock could be very different from the steady one because the time-averaged shock is smeared by the unsteadiness due to shock oscillation. In the linear method, the time-averaged flow is identical to the steady flow, therefore the unsteady perturbation cannot be predicted correctly if the time-averaged flow is very different to the steady one. To handle the shock oscillation in a time-linearized Euler/NS method by using the shock capturing technique, the steady shock has to be smeared by artificial smoothing to get a better prediction of blade aerodynamic

loading (Linquist and Giles, 1991). However, this treatment has little physical insight and cannot be justified for large amplitude shock oscillations which could happen in turbomachinery flows (He,1990b , Ayer and Verdon ,1996). It is highly desirable to develop a method which has a high computational efficiency like the conventional linear methods, but which can account for nonlinear effects like the nonlinear time-marching methods. Recently, a novel nonlinear harmonic approach was proposed by He (1996a). In this approach, the **TIME-AVERAGED** flow (instead of steady flow) is used to be the base of unsteady perturbations. The nonlinear effects are to be included in a **COUPLING SOLUTION** between the time-averaged flow and unsteady perturbations. To illustrate this approach in a simple way, a 1-D convection model equation is used here:

$$\frac{\partial u}{\partial t}+\frac{1}{2}\frac{\partial uu}{\partial x}=0 \tag{1-5}$$

The time-dependent flow variable is composed by:

$$u(x,t)=\bar{u}(x)+u'(x,t) \tag{1-6}$$

where $\bar{u}$ is the time-averaged quantity, u' is a periodic unsteady perturbation. Substituting equation (1-6) into the equation (1-5), we have:

$$\frac{\partial u'}{\partial t}+\frac{1}{2}\frac{\partial}{\partial x}(\bar{u}\bar{u}+2\bar{u}u'+u'u')=0 \tag{1-7}$$

The time-averaged equation can be obtained by time-averaging equation (1-7):

$$\frac{\partial \bar{u}\bar{u}}{\partial x}+\frac{\partial}{\partial x}(\overline{u'u'})=0 \tag{1-8}$$

Compared to equation (1-5), time-averaging generates an extra term in the time-averaged equations. This extra term $\frac{\partial}{\partial x}(\overline{u'u'})$ is a nonlinear term which is similar to the turbulence (Reynolds) stress term. Here it is called "unsteady stress" because it is generated by a periodic unsteadiness.

The unsteady perturbation equation can be obtained by the difference between the basic unsteady flow equation (1-5) and the time-averaged equation (1-8), e.g.

$$\frac{\partial u'}{\partial t} + \frac{1}{2}\frac{\partial}{\partial x}(2\bar{u}u' + u'u' - \overline{u'u'}) = 0 \qquad (1\text{-}9)$$

However, the equation (1-9) is not readily solvable if a frequency-domain harmonic approach is to be used. It is assumed that the unsteady perturbation is dominated by the first order term. Then the second order terms in the unsteady perturbation equation (1-9) can be neglected. The resultant first order equation is given by:

$$\frac{\partial u'}{\partial t} + \frac{\partial}{\partial x}(\bar{u}u') = 0 \qquad (1\text{-}10)$$

The unsteady perturbation equation (1-10) is of the same form as the perturbation equation in the conventional time-linearized Euler method. However, equation (1-10) is no longer linear, because the time-averaged variable $\bar{u}$ is unknown, which in turn depends on the unsteady perturbation. Because of the interaction between the time-averaged and the unsteady perturbation equations, the nonlinear effects due to the unsteadiness can be included in a time-averaged flow and unsteady perturbation coupling solution. The coupling solution procedure is the key to this nonlinear harmonic approach.

The important part of the present work in this thesis is to develop this novel nonlinear harmonic methodology into a nonlinear harmonic Euler/Navier-Stokes method, and to identify its effectiveness by numerical tests in the calculation of unsteady flows around oscillating blades.

1.4 Overview of Thesis

The principal objective of the work in this thesis is to develop efficient frequency domain Euler/Navier-Stokes numerical methods for unsteady flows around oscillating blades. The emphasis is on the development of a novel quasi 3-D frequency domain Euler/Navier-Stokes method based on the nonlinear harmonic methodology (He, 1996a).

To start with, a conventional quasi 3-D time-linearized Euler/Navier-Stokes method is developed for blade flutter and forced response analysis, as described in Chapter 2. In this baseline method, the unsteady flow is decomposed into a steady flow plus a linear harmonically varying unsteady perturbation. Both the steady flow equation and the unsteady perturbation equation are spatially discritized using a cell-vertex finite volume scheme and are integrated using the 4-stage Runge-Kutta scheme in the pseudo-time domain. A moving grid is used to avoid the extrapolation of the flow variables from the boundary of the grid to the instantaneous location of the vibrating blade. At the inlet and outlet boundaries of the computational domain, non-reflecting boundary conditions are implemented to prevent spurious reflections of outgoing pressure, entropy, and vorticity waves back into the computational domain. This quasi-3D time-linearized Euler/Navier-Stokes solver is extensively validated against experimental data and other well-developed numerical methods in the calculation of blade flutter and forced response problems, the numerical results are presented in Chapter 3.

Based upon the developed conventional time-linearized method, a novel nonlinear harmonic Euler/Navier-Stokes method is developed, as described in Chapter 4, by following the nonlinear harmonic approach proposed by He (1996a). In this method, the time-averaged flow (instead of a steady flow in linear methods) is used as the base for the harmonic unsteady perturbations. Due to the nonlinearity of the momentum and energy equations, the time-averaging generates extra "unsteady stress" terms in the time-averaged equations which are evaluated from the unsteady perturbation solutions. A strong coupling technique is used to solve the time-averaged equations and harmonic perturbation equations simultaneously in a pseudo-time domain because of the strong interaction between them. The effectiveness of including nonlinear effects by this novel method is assessed in Chapter 5 by calculating transonic unsteady flows.

Having achieved the primary objective of this thesis, some efforts are made towards a numerical investigation of trailing edge vortex shedding, as presented in Chapter 6. The main objective of this work is to investigate the feasibility of producing a time-independent solution including time-averaged effects of trailing edge vortex shedding by solving time-averaged equations. For either a linear analysis or a nonlinear harmonic analysis, a time-independent solution is needed for the base of the unsteady perturbations. In this investigation, the time-averaged equations about the vortex shedding with known unsteady stresses are solved. The unsteady stresses are worked out from the vortex shedding unsteady calculation results. The structures of the vortex shedding unsteady stresses are analyzed. In this work, two kinds of vortex shedding are considered, one is for a circular cylinder, the other is for a VKI turbine blade.

Finally, this thesis is concluded by Chapter 7 and suggestions for future work are also presented.

Chapter 2 Time-Linearized Harmonic Method

In this chapter, the methodology of a quasi 3-D time-linearized Euler/Navier-Stokes method for unsteady flows induced by blade oscillating and incoming wakes is presented. This method is developed from a well-developed 2-D nonlinear time-marching solver, VIB2D, which was originally developed by He (1994b) for flutter prediction by using an aerodynamic and aeroelastic coupling method. He (1997a, 1997b) later used this programme for rotating stall and partial admission analyses in turbomachinery. The emphasis in this chapter is on the derivation of the time-linearized Navier-Stokes/Euler perturbation equations and the numerical solutions.

2.1 Governing Equations

The integral form of the quasi 3-D unsteady Navier-Stokes equations over a moving finite area ΔA is

$$\frac{\partial}{\partial t}\iint_{\Delta A} U dA + \oint_S [(F - V_x)dy + (G - V_y)dx] = \iint_{\Delta A} S dA \qquad (2\text{-}1)$$

where

$$U = h\begin{pmatrix} \rho \\ \rho u \\ r\rho v \\ \rho e \end{pmatrix} \qquad F = h\begin{pmatrix} \rho u - \rho u_g \\ \rho uu + P - \rho uu_g \\ r(\rho uv - \rho vu_g) \\ (\rho e + P)u - \rho eu_g \end{pmatrix}$$

$$G = h\begin{pmatrix} \rho v - \rho v_g \\ \rho uv - \rho uv_g \\ r(\rho vv + P - \rho vv_g) \\ (\rho e + P)v - \rho ev_g \end{pmatrix} \qquad S = \begin{pmatrix} 0 \\ P\dfrac{\partial h}{\partial x} \\ 0 \\ 0 \end{pmatrix}$$

To close the equation system, a flow state equation is needed to define the pressure P. For an ideal gas it is defined by

$$P = (\gamma - 1)\left(\rho e - \frac{1}{2}\rho(u^2 + v^2)\right) \tag{2-2}$$

The quasi 3-D effects are introduced by allowing specified variations of radius r and streamtube height h in the axial direction. u_g and v_g are the grid velocities used to accommodate the grid movement due to blade rotating and vibration. The viscous effects are introduced by the viscous terms:

$$V_x = h\begin{pmatrix} 0 \\ \tau_{xx} \\ r\tau_{xy} \\ -q_x + u\tau_{xx} + v\tau_{xy} \end{pmatrix} \qquad V_y = h\begin{pmatrix} 0 \\ \tau_{xy} \\ r\tau_{yy} \\ -q_y + u\tau_{xy} + v\tau_{yy} \end{pmatrix}$$

where:

$$\tau_{xx} = \frac{2}{3}\mu(2\frac{\partial u}{\partial x} - \frac{\partial v}{\partial y}), \quad \tau_{yy} = \frac{2}{3}\mu(2\frac{\partial v}{\partial y} - \frac{\partial u}{\partial x}), \quad \tau_{xy} = \mu(\frac{\partial u}{\partial y} + \frac{\partial v}{\partial x})$$

$$q_x = -k\frac{\partial T}{\partial x}, \qquad q_y = -k\frac{\partial T}{\partial y}$$

The viscosity is $\mu = \mu_l + \mu_t$. The laminar viscosity μ_l is obtained from the Sutherland's law with a reference viscosity coefficient being calculated from a fixed Reynolds number at the inlet flow condition. The turbulence viscosity μ_t is worked out by the standard Baldwin-Lomax algebraic mixing length model (Baldwin and Lomax, 1978). The coefficient of heat conductivity, k, is related to the viscosity coefficient through a Prantl number.

The Euler version of governing equation (2-1) for inviscid flows can be easily obtained by switching off the viscous terms V_x and V_y.

2.2 Time-Linearized Perturbation Equations

The equation (2-1) can be linearized, provided the temporal change of a flow variable is small enough compared to the steady value. Assume that the flow can be divided into two parts: a **steady** flow plus a small harmonic perturbation part, i.e.

$$U(x,y,t) = \hat{U}(x,y) + \tilde{U}(x,y)e^{i\omega t} \tag{2-3}$$

The detailed form of $\tilde{U}$ can be expressed by

$$\tilde{U} = h\begin{pmatrix} \tilde{\rho} \\ \tilde{(\rho u)} \\ \tilde{r(\rho v)} \\ \tilde{(\rho e)} \end{pmatrix} \tag{2-4}$$

Meanwhile, the unsteady grid moving velocities u_g and v_g are also assumed to change in a harmonic form,

$$u_g(x,y,t) = \tilde{u}_g(x,y)e^{i\omega t}, \qquad v_g(x,y,t) = \hat{v}_g + \tilde{v}_g(x,y)e^{i\omega t} \tag{2-5}$$

For a rotor, $\hat{v}_g$ is the bladerow rotating speed.

Substituting the relationships (2-3) to (2-5) into the convective fluxes F and G, and neglecting all the 2nd order terms, the complex amplitudes of fluxes F and G can be given by

$$\tilde{F} = h\begin{pmatrix} \tilde{(\rho u)} - \tilde{(\rho u_g)} \\ \hat{(\rho u)}(\tilde{u} - \tilde{u}_g) + \tilde{(\rho u)}\hat{u} + \tilde{P} \\ r[\hat{(\rho v)}(\tilde{u} - \tilde{u}_g) + \tilde{(\rho v)}\hat{u}] \\ [\hat{(\rho e)} + \hat{P}]\tilde{u} + [\tilde{(\rho e)} + \tilde{P}]\hat{u} - \hat{(\rho e)}\tilde{u}_g \end{pmatrix} \tag{2-6}$$

$$\tilde{G} = h\begin{pmatrix} \tilde{(\rho v)} - \tilde{(\rho v_g)} \\ \hat{(\rho u)}(\tilde{v} - \tilde{v}_g) + \tilde{(\rho u)}(\hat{v} - \hat{v}_g) \\ r[\hat{(\rho v)}(\tilde{v} - \tilde{v}_g) + \tilde{(\rho v)}(\hat{v} - \hat{v}_g) + \tilde{P}] \\ [\hat{(\rho e)} + \hat{P}]\tilde{u} + [\tilde{(\rho e)} + \tilde{P}]\hat{u} - \hat{(\rho e)}\tilde{v}_g - \tilde{(\rho e)}\hat{v}_g \end{pmatrix} \tag{2-7}$$

where the non-conservative variable perturbations can be worked out from conservative variable perturbations, i.e.

$$\tilde{u} = \tilde{(\rho u)}/\hat{\rho} - \tilde{\rho}\hat{(\rho u)}/\hat{\rho}^2$$

$$\tilde{v} = \tilde{(\rho v)}/\hat{\rho} - \tilde{\rho}\hat{(\rho v)}/\hat{\rho}^2$$

$$\tilde{P} = (\gamma - 1)\{\tilde{(\rho e)} - \hat{u}\tilde{(\rho u)} - \hat{v}\tilde{(\rho v)} + \frac{1}{2}[\hat{u}^2 + \hat{v}^2]\tilde{\rho}\}$$

Similarly, the perturbation of viscous terms in Eq.(2-1) can be given by linearizing the V_x and V_y, as

$$\tilde{V}_x = h\begin{pmatrix} 0 \\ \tilde{\tau}_{xx} \\ r\tilde{\tau}_{xy} \\ -\tilde{q}_x + \tilde{u}\hat{\tau}_{xx} + \tilde{v}\hat{\tau}_{xy} + \hat{u}\tilde{\tau}_{xx} + \hat{v}\tilde{\tau}_{xy} \end{pmatrix} \tag{2-8}$$

$$\tilde{V}_y = h\begin{pmatrix} 0 \\ \tilde{\tau}_{xy} \\ r\tilde{\tau}_{yy} \\ -\tilde{q}_y + \tilde{u}\hat{\tau}_{xy} + \tilde{v}\hat{\tau}_{yy} + \hat{u}\tilde{\tau}_{xy} + \hat{v}\tilde{\tau}_{yy} \end{pmatrix} \qquad (2\text{-}9)$$

where

$$\tilde{\tau}_{xx} = \frac{2}{3}\hat{\mu}(2\frac{\partial\tilde{u}}{\partial x} - \frac{\partial\tilde{v}}{\partial y}), \quad \tilde{\tau}_{yy} = \frac{2}{3}\hat{\mu}(2\frac{\partial\tilde{v}}{\partial y} - \frac{\partial\tilde{u}}{\partial x}), \quad \tilde{\tau}_{xy} = \hat{\mu}(\frac{\partial\tilde{u}}{\partial y} + \frac{\partial\tilde{v}}{\partial x})$$

$$\tilde{q}_x = -k\frac{\partial\tilde{T}}{\partial x}, \qquad \tilde{q}_y = -k\frac{\partial\tilde{T}}{\partial y}$$

In this method, the perturbation of viscosity due to unsteadiness is neglected simply by freezing the viscosity to its steady value in the perturbation equations. Although the turbulent viscosity perturbation could be obtained by linearizing turbulence models, doing so will significantly increase the computation time and make the code writing much more complex. Under the Boussinesq approximation, the primary role of the turbulence is to provide enhanced diffusivities intended to mimic the turbulent mixing. The interaction between the turbulence and the steady flow is minor compared to the added diffusivity introduced by the eddy viscosity. The validity of frozen viscosity in the linear methods has been investigated by some researchers (Holmes and Lorence, 1997). In a comparison of predicted unsteady pressures from both a frozen turbulence model and a fully linearized turbulence model, only a minor difference was found at an extremely low frequency case (reduced frequency of 0.034), the results are nearly identical at normal blade flutter frequencies.

To linearize Eq.(2-1), the computational grid is also assumed to undergo a small harmonic deformation about its steady position, i.e.,

$$x = \hat{x} + \tilde{x}e^{i\omega t}, \quad y = \hat{y} + \tilde{y}e^{i\omega t}$$

The source term S in Eq.(2-1) can also be decomposed into a steady part plus a harmonic perturbation, the perturbation part can be given by

$$\tilde{S} = \begin{pmatrix} 0 \\ \tilde{P}\dfrac{\partial h}{\partial x} \\ 0 \\ 0 \end{pmatrix} \tag{2-10}$$

Substituting all the perturbation series into the integral unsteady Navier-Stokes equations (2-1) and collecting zero and first order terms, the original equation can be divided into two equations: a steady equation and a linearized perturbation equation. The steady equation is given by

$$\oint_s [(\hat{F} - \hat{V}_x)d\hat{y} + (\hat{G} - \hat{V}_y)d\hat{x}] = \iint_{\Delta A} \hat{S}d\hat{A} \tag{2-11}$$

The integral form of the time-linearized Navier-Stokes perturbation equation is

$$\oint_s [(\tilde{F} - \tilde{V}_x)d\hat{y} + (\tilde{G} - \tilde{V}_y)d\hat{x} + (\hat{F} - \hat{V}_x)d\tilde{y} + (\hat{G} - \hat{V}_y)d\tilde{x}]$$
$$= \iint_{\Delta\hat{A}} (\tilde{S}d\hat{A} + \hat{S}d\tilde{A}) - i\omega \iint_{\Delta\hat{A}} \tilde{U}d\hat{A} - i\omega \iint_{\Delta\hat{A}} \hat{U}d\tilde{A} \tag{2-12}$$

Note that all the variables in both Eq.(2-11) and Eq.(2-12) are only space-dependent, time does not appear. The coefficients in Eq.(2-12) are obtained from the solution of the steady flow equation (2-11).

2.3 Solution Method

The solution procedure for a time-linearized Navier-Stokes/Euler method is straightforward, as depicted in Fig.2-1. Firstly a steady flow solution is produced by solving the steady Navier-Stokes/Euler equation (2-11). Then, for a flutter problem, the grid moving velocities are prescribed according to a blade vibrating mode (bending or torsion). Finally for a given frequency and inter-blade phase angle, the coefficients in the time-linearized Navier-Stokes/Euler equation (2-12) are formed from the steady flow solution and the time-linearized perturbation equation is solved. By linearization, solving a time-dependent unsteady problem in the time-domain is effectively transformed to solving two steady equations. Therefore, the time-linearized method normally is much more computationally efficient than the nonlinear time-marching methods.

2.3.1 Pseudo Time Dependence

In order to fully take advantage of the efficient time-marching methods, a pseudo time variable (t') is introduced to make the steady equation (2-11) and the time-linearized perturbation equation (2-12) time-dependent, so Eq.(2-11) and (2-12) can be re-written as

$$\frac{\partial}{\partial t'}\iint_{\Delta A}\hat{U}d\hat{A}+\oint_S[(\hat{F}-\hat{V}_x)d\hat{y}+(\hat{G}-\hat{V}_y)d\hat{x}]=\iint_{\Delta A}\hat{S}d\hat{A} \qquad (2\text{-}13)$$

and

$$\frac{\partial}{\partial t'}\iint_{\Delta\hat{A}}\tilde{U}d\hat{A}+\oint_S[(\tilde{F}-\tilde{V}_x)d\hat{y}+(\tilde{G}-\tilde{V}_y)d\hat{x}+(\hat{F}-\hat{V}_x)d\tilde{y}+(\hat{G}-\hat{V}_y)d\tilde{x}]$$

$$=\iint_{\Delta\hat{A}}(\tilde{S}d\hat{A}+\hat{S}d\tilde{A})-i\omega\iint_{\Delta\hat{A}}\tilde{U}d\hat{A}-i\omega\iint_{\Delta\hat{A}}\hat{U}d\tilde{A} \qquad (2\text{-}14)$$

Now both the steady equation and linear perturbation equation are hyperbolic in pseudo time, any well-developed time-marching scheme can be used to solve them. Since only a 'steady-state' solution for steady flow and unsteady perturbation amplitude are desired, any efficient acceleration techniques like local time-stepping and multigrid can be used to speed up the convergence of a solution. This pseudo time-marching idea was originally proposed by Ni (1974).

2.3.2 Spatial and Temporal Discretization

The spatial discretization for both Eq.(2-13) and Eq.(2-14) is made by using a cell-vertex finite volume scheme. Consider a H-type mesh consisting of $I \times J$ quadrilateral cells. For each mesh cell, Eq.(2-13) and (2-14) can be written in a semi-discrete form, e.g. for a cell with an index (i,j):

$$\frac{d}{dt'}(\hat{U}\Delta\hat{A})_{ij} = (\hat{FLUX}_I + \hat{FLUX}_v)_{ij} + (\hat{S}\Delta\hat{A})_{ij}$$

$$= \hat{R}_{ij} \qquad (2\text{-}15)$$

and

$$\frac{d}{dt'}(\tilde{U}\Delta\hat{A})_{ij} = (\tilde{FLUX}_I + \tilde{FLUX}_v)_{ij} + (\tilde{S}\Delta\hat{A} + \hat{S}\Delta\tilde{A})_{ij}$$

$$-i\omega(\tilde{U}\Delta\hat{A} + \hat{U}\Delta\tilde{A})_{ij}$$

$$= \tilde{R}_{ij} \qquad (2\text{-}16)$$

where

$$\hat{FLUX}_I = -\sum_1^4 [\hat{F}\Delta\hat{y} + \hat{G}\Delta\hat{x}]$$

$$\hat{FLUX}_v = \sum_1^4 [\hat{V}_x \Delta\hat{y} + \hat{V}_y \Delta\hat{x}]$$

$$\tilde{FLUX}_I = -\sum_1^4 [\tilde{F}\Delta\hat{y} + \tilde{G}\Delta\hat{x} + \hat{F}\Delta\tilde{y} + \hat{G}\Delta\tilde{x}]$$

$$\tilde{FLUX}_v = \sum_1^4 [\tilde{V}_x \Delta\hat{y} + \tilde{V}_y \Delta\hat{x} + \hat{V}_x \Delta\tilde{y} + \hat{V}_y \Delta\tilde{x}]$$

The summation is taken along the four boundary surfaces of the cell. The fluxes across each surface are evaluated using the flow variables stored at the corners of the cell. For viscous fluxes, the first order spatial derivatives are evaluated by using the Gauss theorem on auxiliary cells (He, 1993). Once the temporal change is evaluated, it is equally distributed to the each corner of the cell.

This cell-vertex finite volume scheme is a spatial second order centre difference scheme. There are no even order dissipative terms in the scheme itself. In order to suppress the numerical oscillation and capture the steady shock waves in a steady flow calculation and the shock impulse in a perturbation solution, a 2nd and 4th order adaptive smoothing (Jameson et al, 1981) is applied in both streamwise and pitchwise directions. So Eq.(2-15) and (2-16) become:

$$\frac{d}{dt'}(\hat{U}\Delta\hat{A})_{ij} = \hat{R}_{ij} + (\hat{d}_x)_{ij} + (\hat{d}_y)_{ij} - (\hat{D}_x)_{ij} - (\hat{D}_y)_{ij} \qquad (2\text{-}17)$$

and

$$\frac{d}{dt'}(\tilde{U}\Delta\hat{A})_{ij} = \tilde{R}_{ij} + (\tilde{d}_x)_{ij} + (\tilde{d}_y)_{ij} - (\tilde{D}_x)_{ij} - (\tilde{D}_y)_{ij} \qquad (2\text{-}18)$$

where the $\hat{d}_x$ and $\hat{d}_y$ are the second order steady artificial smoothing in x and y directions, $\hat{D}_x$ and $\hat{D}_y$ are the fourth order artificial smoothing terms. $\tilde{d}_x$ and $\tilde{d}_y$

are the amplitudes of the second order artificial smoothing, $\hat{D}_x$ and $\hat{D}_y$ are the amplitudes of fourth order artificial smoothing terms.

For the steady flow equation, $\hat{d}_x$ and $\hat{D}_x$ can be given by

$$\hat{d}_x = \varepsilon_{ij}^{(2)}(\hat{U}_{i+1j} - 2\hat{U}_{ij} + \hat{U}_{i-1j})\Delta\hat{A}_{ij} / dt' \tag{2-19}$$

$$\hat{D}_x = \varepsilon_{ij}^{(4)}(\hat{U}_{i+2j} - 4\hat{U}_{i+1j} + 5\hat{U}_{ij} - 4\hat{U}_{i-1j} + \hat{U}_{i-2j})\Delta\hat{A}_{ij} / dt' \tag{2-20}$$

where

$$\varepsilon_{ij}^{(2)} = k^{(2)}\theta_{ij}^{(2)} \tag{2-21}$$

$$\theta_{ij}^{(2)} = \left|\frac{\hat{P}_{i+1j} - 2\hat{P}_{ij} + \hat{P}_{i-1j}}{\hat{P}_{i+1j} + 2\hat{P}_{ij} + \hat{P}_{i-1j}}\right| \tag{2-22}$$

$$\varepsilon_{ij}^{(4)} = \max\{0, (k^{(4)} - \varepsilon_{ij}^{(2)})\} \tag{2-23}$$

where $k^{(2)}$ is the 2nd order smoothing coefficient, typically it is about 1/2. The $k^{(4)}$ is the 4th order smoothing coefficient and about 1/32. $\hat{d}_y$ and $\hat{D}_y$ can be given similarly.

For the unsteady perturbation equation, $\tilde{d}_x$ and $\tilde{D}_x$ can be given by

$$\tilde{d}_x = \varepsilon_{ij}^{(2)}(\tilde{U}_{i+1j} - 2\tilde{U}_{i,j} + \tilde{U}_{i-1j})\Delta\hat{A}_{ij} / dt' \tag{2-24}$$

$$\tilde{D}_x = \varepsilon_{ij}^{(4)}(\tilde{U}_{i+2j} - 4\tilde{U}_{i+1j} + 5\tilde{U}_{ij} - 4\tilde{U}_{i-1j} + \tilde{U}_{i-2j})\Delta\hat{A}_{ij} / dt' \tag{2-25}$$

In order to avoid linearizing the pressure sensor (2-22), here the smoothing coefficients for the unsteady amplitudes are frozen at their steady values, effectively the unsteady fluctuation of the pressure sensor is neglected. The validity of this practice for linear problems is validated by other authors (Linquist and Giles, 1991) . $\tilde{d}_y$ and $\tilde{D}_y$ can be given in a similar manner.

The pseudo time-marching for both Eq.(2-17) and (2-18) is performed by using the 4-stage Runge-Kutta scheme. The formulation of the 4-stage Runge-Kutta time marching from time step n to n+1 is:

$$\hat{U}_{ij}^{n+\alpha_k} = \hat{U}_{ij}^{n} - \alpha_k \frac{\Delta t'}{\Delta A}\{\hat{R}_{ij} + (\hat{d}_x)_{ij} + (\hat{d}_y)_{ij} - (\hat{D}_x)_{ij} - (\hat{D}_y)_{ij}\}^{n+\alpha_{k-1}} \tag{2-26}$$

and

$$\tilde{U}_{ij}^{n+\alpha_k} = \tilde{U}_{ij}^{n} - \alpha_k \frac{\Delta t'}{\Delta A}\{\tilde{R}_{ij} + (\tilde{d}_x)_{ij} + (\tilde{d}_y)_{ij} - (\tilde{D}_x)_{ij} - (\tilde{D}_y)_{ij}\}^{n+\alpha_{k-1}} \tag{2-27}$$

where

k=1~4

and

$$\alpha_0 = 0, \quad \alpha_1 = 1/4, \quad \alpha_2 = 1/3, \quad \alpha_3 = 1/2, \quad \alpha_4 = 1$$

For stability of the explicit time-marching scheme, the size of $\Delta t'$ can be defined by

$$\Delta t' \le CFL \cdot \min\{[\min(\Delta\hat{x}, \Delta\hat{y}) / (\sqrt{\hat{u}^2 + \hat{v}^2} + \hat{c})]_{ij}\} \qquad (2\text{-}28)$$

$$(i = 1, 2, ..., I,\ j = 1, 2, ..., J)$$

where CFL stands for the Courant-Friedrichs-Lewy number. The stability limit for the steady state equation gives $CFL < 2\sqrt{2}$ for the 4-stage Runge-Kutta scheme. A stability analysis for the time-linearized perturbation Euler equation by Lindquist (1991) has shown that the limit of $\Delta t'$ size is very close to the steady state equation. In this method, a uniform time step is used in both steady and perturbation solutions.

To enhance the computational efficiency for viscous flow calculations, the two-grid acceleration technique proposed by He (1993a) is used for solving both steady and time-linearized perturbation Navier-Stokes equations, although this technique was originally developed for speeding up nonlinear unsteady calculations.

2.3.3 Boundary Conditions

For a single blade passage domain as shown in Fig.1-3, there are four kinds of boundary conditions, i.e. inlet, outlet, periodic and solid wall boundary conditions.

For steady flow calculations, the conventional boundary conditions are implemented. At inlet, the total pressure, total temperature and inlet flow angle for subsonic flow or inlet Mach Number for supersonic flow are prescribed, and the static pressure at inlet is extrapolated from the interior domain. At outlet, the static back pressure is given and other flow variables are extrapolated from the interior domain. For periodic boundaries, a direct repeating condition is applied on both the

upper and the lower periodic boundaries *ab* and *cd*, as depicted in Fig.1-3. On the blade surface, zero flux is applied across the finite volume boundaries for inviscid flow calculation, either a non-slip wall or slip wall boundary treatment can be chosen for viscous flow calculations. For the non-slip wall boundary condition, the velocities on the blade surface are set to be zero, and the wall shear stress is evaluated according to the local velocity gradients. Usually a very fine mesh near the wall is required for the non-slip wall condition to resolve the boundary layer. For slip-wall condition, the velocities on the wall are allowed to slip, the wall shear stress for turbulent flows is approximated by a log-law formulation (Denton, 1990), as

$$\hat{\tau}_w = \frac{1}{2}\hat{c}_f \hat{\rho}_2 \hat{w}_2^2 \tag{2-29a}$$

and

$$\hat{c}_f = \begin{cases} 2/\hat{Re}_2, \hat{Re}_2 < 125 \\ -0.001767 + \dfrac{0.03177}{\ln(\hat{Re}_2)} + \dfrac{0.25614}{[\ln(\hat{Re}_2)]^2}, \hat{Re}_2 \geq 125 \end{cases} \tag{2-29b}$$

where the subscript "2" represents the mesh point one grid away from the wall and

$$\hat{Re}_2 = \hat{\rho}_2 \hat{w}_2 \Delta y_2 / \mu_l$$

with $\hat{w}_2 = \sqrt{\hat{u}_2^2 + (\hat{v}_2 - \hat{v}_g)^2}$. The slip wall condition needs fewer mesh points in the near wall region than the non-slip wall condition, and therefore can save the computation time.

The boundary conditions for solving the time-linearized Navier-Stokes/Euler perturbation equations are much more complex than those for solving steady flow equations, and are presented in the following sections.

2.3.3.1 Phase-Shifted Periodic Conditions

For a single blade passage, as shown in Fig.1-3, if the upper boundary *ab* has an inter-blade phase angle (IBPA) σ lead to the lower boundary *cd*, a phase-shifted periodic condition has to be applied for solving the perturbation equation (2-16), i.e.

$$\tilde{U}^u = \tilde{U}^l e^{i\sigma} \tag{2-30}$$

where the superscript "u" refers to the upper boundary *ab* and "l" represents the lower boundary *cd*. The perturbations in the time-linearized Navier-Stokes/Euler equations are complex numbers, the real and imaginary parts can be updated by

$$(\tilde{U}^u_{real})^{new} = \frac{1}{2}\left(\tilde{U}^u_{real} + \tilde{U}^l_{real}\cos\sigma - \tilde{U}^l_{imag}\sin\sigma\right)^{old} \tag{2-31a}$$

$$(\tilde{U}^u_{imag})^{new} = \frac{1}{2}\left(\tilde{U}^u_{imag} + \tilde{U}^l_{real}\sin\sigma + \tilde{U}^l_{imag}\cos\sigma\right)^{old} \tag{2-31b}$$

$$(\tilde{U}^l_{real})^{new} = \frac{1}{2}\left(\tilde{U}^l_{real} + \tilde{U}^u_{real}\cos\sigma + \tilde{U}^u_{imag}\sin\sigma\right)^{old} \tag{2-31c}$$

$$(\tilde{U}^l_{imag})^{new} = \frac{1}{2}\left(\tilde{U}^l_{imag} + \tilde{U}^u_{imag}\cos\sigma - \tilde{U}^u_{real}\sin\sigma\right)^{old} \tag{2-31d}$$

where the subscript "real" refers to the real part of a complex number and "imag" refers to the imaginary part.

2.3.3.2 Inlet and Outlet Boundary Conditions

For an unsteady flow calculation in a finite extent computational domain as shown in Fig.1-3, inlet and outlet boundary conditions have to be properly constructed to prevent spurious reflections from far-field boundaries (inlet and outlet). Otherwise the outgoing pressure, entropy, and vorticity waves can be reflected back into the computational domain to corrupt the solution. The development of nonreflecting boundary conditions for nonlinear and linear unsteady flow calculations in turbomachinery is active in recent years. A notable nonreflecting far-field boundary condition for 2-D Euler equations is made by Giles (1990b). In this method, the nonlinear Euler method is linearized and the steady flow at inlet and outlet is assumed to be uniform. By using the Fourier analysis, the amplitudes of four characteristic waves (downstream running and upstream running pressure waves, vorticity wave, and entropy wave) can be expressed by the sum of four complex amplitudes (pressure, density, velocities in x and y directions) and vice versa. According to the characteristics of these four waves, the nonreflecting boundary conditions can be constructed at the inlet and outlet boundaries. The error in this boundary condition is mainly introduced by the linearization of Euler equations and nonuniformity of inlet and outlet steady flows.

In the present time-linearized Navier-Stokes/Euler method, two kinds of nonreflecting boundaries developed by Giles (1990b) are implemented in solving the time-linearized perturbation equations, one is the 1-D unsteady boundary condition, another is the exact 2-D single-frequency boundary condition. In order to reduce the error in the nonreflecting boundaries induced by the wakes in viscous flow calculations, the steady flow at outlet is circumferentially averaged to give an 'uniform' steady flow base for implementing the boundary conditions.

To implement the nonreflecting boundary conditions, firstly the transformation between the amplitudes of four characteristic waves and amplitudes of pressure, density, velocities in x and y directions are given by

$$\begin{pmatrix} \tilde{c}_1 \\ \tilde{c}_2 \\ \tilde{c}_3 \\ \tilde{c}_4 \end{pmatrix} = \begin{pmatrix} -\hat{c}^2 & 0 & 0 & 1 \\ 0 & 0 & \hat{\rho}\hat{c} & 0 \\ 0 & \hat{\rho}\hat{c} & 0 & 1 \\ 0 & -\hat{\rho}\hat{c} & 0 & 1 \end{pmatrix} \begin{pmatrix} \tilde{\rho} \\ \tilde{u} \\ \tilde{v} \\ \tilde{P} \end{pmatrix} \tag{2-32}$$

and

$$\begin{pmatrix} \tilde{\rho} \\ \tilde{u} \\ \tilde{v} \\ \tilde{P} \end{pmatrix} = \begin{pmatrix} -\frac{1}{\hat{c}^2} & 0 & \frac{1}{2\hat{c}^2} & \frac{1}{2\hat{c}^2} \\ 0 & 0 & \frac{1}{2\hat{\rho}\hat{c}} & -\frac{1}{2\hat{\rho}\hat{c}} \\ 0 & \frac{1}{\hat{\rho}\hat{c}} & 0 & 0 \\ 0 & 0 & \frac{1}{2} & \frac{1}{2} \end{pmatrix} \begin{pmatrix} \tilde{c}_1 \\ \tilde{c}_2 \\ \tilde{c}_3 \\ \tilde{c}_4 \end{pmatrix} \tag{2-33}$$

where $\tilde{c}_1$, $\tilde{c}_2$, $\tilde{c}_3$, and $\tilde{c}_4$ are the amplitudes of four characteristic waves (entropy , vorticity, downstream running pressure, upstream running pressure waves). $\hat{c}$ is the local sound speed.

In order to handle the forced response problems induced by incoming wakes, the transformation relationships of (2-32) and (2-33) at inlet can be re-written as

$$\begin{pmatrix} \tilde{c}_1 \\ \tilde{c}_2 \\ \tilde{c}_3 \\ \tilde{c}_4 \end{pmatrix} = \begin{pmatrix} -\hat{c}^2 & 0 & 0 & 1 \\ 0 & 0 & \hat{\rho}\hat{c} & 0 \\ 0 & \hat{\rho}\hat{c} & 0 & 1 \\ 0 & -\hat{\rho}\hat{c} & 0 & 1 \end{pmatrix} \begin{pmatrix} \tilde{\rho} - \tilde{\rho}_{inl} \\ \tilde{u} - \tilde{u}_{inl} \\ \tilde{v} - \tilde{v}_{inl} \\ \tilde{P} - \tilde{P}_{inl} \end{pmatrix} \tag{2-34}$$

and

$$\begin{pmatrix} \tilde{\rho}-\tilde{\rho}_{inl} \\ \tilde{u}-\tilde{u}_{inl} \\ \tilde{v}-\tilde{v}_{inl} \\ \tilde{P}-\tilde{P}_{inl} \end{pmatrix} = \begin{pmatrix} -\frac{1}{\hat{c}^2} & 0 & \frac{1}{2\hat{c}^2} & \frac{1}{2\hat{c}^2} \\ 0 & 0 & \frac{1}{2\hat{\rho}\hat{c}} & -\frac{1}{2\hat{\rho}\hat{c}} \\ 0 & \frac{1}{\hat{\rho}\hat{c}} & 0 & 0 \\ 0 & 0 & \frac{1}{2} & \frac{1}{2} \end{pmatrix} \begin{pmatrix} \tilde{c}_1 \\ \tilde{c}_2 \\ \tilde{c}_3 \\ \tilde{c}_4 \end{pmatrix} \qquad (2\text{-}35)$$

where $\tilde{\rho}_{inl}$, $\tilde{u}_{inl}$, $\tilde{v}_{inl}$, and $\tilde{P}_{inl}$ are amplitudes of the prescribed incoming wake profile. The incoming wake can be prescribed by different ways such as a simple sinusoidal distribution or superposition of different Fourier harmonic components for a more accurate expression. For superposition of different harmonic components to model a wake, the linear perturbation equations have to be solved for each harmonic components.

According to the characteristics of travelling waves, the 1-D unsteady nonreflecting boundary condition for an axial subsonic flow can be given

At inlet:
$$\begin{pmatrix} \tilde{c}_1 \\ \tilde{c}_2 \\ \tilde{c}_3 \end{pmatrix} = 0 \qquad (2\text{-}36a)$$

At outlet:
$$\tilde{c}_4 = 0 \qquad (2\text{-}36b)$$

The 1-D nonreflecting boundary condition, which ignores all variations in the y directions, is very simple and easy to implement, but it is not accurate enough for some cut-off conditions (Giles, 1991b).

To be more accurate, a two-dimensional nonreflecting boundary condition is also implemented in the present time-linearized method. This boundary condition can be given by

$$\text{At inlet:} \qquad \frac{\partial}{\partial t'}\begin{pmatrix}\tilde{c}_1\\ \tilde{c}_2\\ \tilde{c}_3\end{pmatrix} = \alpha\begin{pmatrix} -\tilde{c}_1 \\ \dfrac{(\hat{c}-\hat{u})\lambda}{(1+S)(\hat{c}-\hat{v}\lambda)}\tilde{c}_4 - \tilde{c}_2 \\ \dfrac{(\hat{c}-\hat{u})^2\lambda^2}{(1+S)^2(\hat{c}-\hat{v}\lambda)}\tilde{c}_4 - \tilde{c}_3 \end{pmatrix} \qquad \text{(2-37a)}$$

$$\text{At outlet:} \qquad \frac{\partial \tilde{c}_4}{\partial t'} = \alpha\left(\frac{2\hat{u}\lambda}{(\hat{c}-\hat{v}\lambda)(1+S)}\tilde{c}_2 + \frac{1-S}{1+S}\tilde{c}_3 - \tilde{c}_4\right) \qquad \text{(2-37b)}$$

where λ is the wave length defined by

$$\lambda = \frac{\hat{c}b}{\omega}$$

and

$$S = \sqrt{1 - \frac{(\hat{c}^2 - \hat{u}^2)\lambda^2}{(\hat{c}-\hat{v}\lambda)^2}}$$

where $b = \sigma / \Delta y_{pitch}$ is the wave number, σ is the inter-blade phase angle and Δy_{pitch} is the blade pitch. (2-37a) and (2-37b) can be time-marched in the same manner as the interior domain by using the 4-Stage Runge -Kutta scheme. α is the relaxing coefficient, choosing a too large value may lead to a numerical instability, choosing too small value will lead to a poor convergence rate, typically it is to be $1/\Delta y_{pitch}$.

2.3.3.3 Solid Wall Boundary Conditions

For solving the time-linear Euler equations, the perturbations of fluxes are simply set to be zero on the blade surface.

To be consistent with solving the steady Navier-Stokes equations, there are two kinds of solid wall boundary conditions implemented to solve the time-linearized Navier-Stokes perturbation equations, non-slip wall and slip-wall conditions. For the non-slip wall boundary condition, the relative velocity perturbations on the solid wall are simply set to zero and the perturbation of wall shear stress is evaluated according to the local velocity gradients.

For the slip-wall condition, the perturbation of shear stress is obtained by linearizing the nonlinear relationship

$$\tau_w = \frac{1}{2} c_f \rho w_2^2 \tag{2-38}$$

to give,

$$\tilde{\tau}_w = \frac{1}{2}[\tilde{c}_f \rho \hat{w}_2^2 + \hat{c}_f (\rho \tilde{w}_2^2)] \tag{2-39}$$

where $\hat{c}_f$ can be obtained by the relationship (2-29b) and the $\tilde{c}_f$ can be given by linearizing the relationship (2-29b).

An interesting issue related to the solid wall boundary condition is, what would happen if a time-linearized Euler perturbation equation is solved based on a steady viscous flow field generated by a Navier-Stokes solver? This issue might be of practical interest since some linearized Euler methods have been already developed

and it would be practically beneficial if these methods can be directly applied based on a steady flow provided by a separate well-developed steady viscous flow solver. Numerical tests were carried out in the present work by switching off all the viscous perturbation terms and solving the Euler perturbation equations based on a viscous flow field. The numerical tests show that for some test cases, doing this reveals serious convergence problems. This can be explained by comparing the unsteady perturbation equations with original unsteady Navier-Stokes equations. The original unsteady viscous flow model requires that tangential velocities must be constrained either by a non-slip wall condition or by applying a wall shear stress. This constraint is effectively lost if the Euler perturbation equations are used for the unsteady part of the flow, regardless of the condition applied in the steady viscous flow part. Therefore, solving the Euler perturbation equations on the viscous steady flow field does not seem reliable. This issue is also discussed in a work by Holmes and Lorence (1997).

2.4 Summary

In this chapter, a quasi 3-D time-linearized Navier/Stokes method has been developed. In this method, an unsteady flow is decomposed to be a steady flow plus a harmonically varying small perturbation. By the linearization, the original unsteady flow governing equation is divided into two equations: a steady flow equation and a linear perturbation equation. A pseudo-time technique is introduced to make these two equations time-dependent. Both the steady flow and perturbation equations are spatially discritized by a cell-vertex finite volume scheme and temporally integrated by the 4-stage Runge-Kutta time-marching scheme in a pseudo-time domain. The grid moving velocities are explicitly included in the original flow governing equations and it is easy to handle the moving grids. To prevent spurious reflections of outgoing waves, a 1-D/2-D nonreflecting boundary condition is implemented. To enhance the computational efficiency, a 2-grid acceleration technique is applied to speed up the time-linearized viscous calculations. To be consistent with the solid wall conditions

used in the steady flow solver, a slip-wall boundary condition has been developed in solving the Navier-Stokes unsteady perturbation equations.

By linearization, solving an unsteady flow equation in a real time-domain is effectively equivalent to solving two time-independent equations, therefore the time-linearized method normally is much more efficient than the nonlinear time-marching methods.

Chapter 3 Validations for Time-Linearized Method

A quasi 3-D time-linearized Navier-Stokes/Euler method has been developed for unsteady flows in turbomachinery, as described in Chapter 2. In this Chapter, the computational results by this time-linearized method for the unsteady flows induced by the blade oscillation and unsteady incoming wakes will be presented. In order to validate the method, the calculated results will be compared to the numerical results produced by other well-developed linear methods, nonlinear time-marching methods, and experimental data. The calculations are carried out in two parts: inviscid flow calculations for validating the time-linearized Euler method, and viscous flow calculations for validating the time-linearized Navier-Stokes method.

3.1 Euler Solutions

3.1.1 Oscillating Flat Plate Cascade

The first case for the validation on the time-linearized Euler method is made by calculating the unsteady flows around an oscillating flat plate cascade. The geometry of this cascade is

Chord:	C = 0.076m
Solidity:	C / Pitch = 1.3
Stagger angle:	$\gamma = 30^0$

and the flow has a Mach number of 0.65 and zero incidence.

The unsteady flows are introduced by the blade oscillation in a torsion mode around its leading edge with 1 degree amplitude and -90^0 inter-blade phase angle. The calculations are carried out under two different reduced frequencies (based on

the blade chord and flow inlet velocity), one is a lower frequency of 0.57, another is a higher frequency of 1.714.

In this flat plate cascade test case, the nonlinear effect is negligible. The calculated unsteady pressure jumps as defined later by the present time-linearized Euler method are compared to those generated by a well-established linear solver LINSUB. The programme LINSUB was described by Whitehead (1987) based on a semi-analytical linear method and it can handle several kinds of turbomachine unsteady flows in a flat plate cascade induced by the blade oscillation, incoming wakes, and inlet or outlet pressure waves. The solution of LINSUB is very accurate so that it is widely used to validate numerical methods. The unsteady pressure coefficient jump is defined by

$$\Delta(\tilde{c}_p) = (\tilde{c}_p)^u - (\tilde{c}_p)^l \tag{3-1}$$

where the unsteady pressure coefficient, $\tilde{c}_p$, is defined by

$$\tilde{c}_p = \frac{\tilde{p}}{0.5\hat{\rho}_{inl}\hat{w}^2{}_{inl}A_m} \tag{3-2}$$

where A_m is the amplitude of blade torsion, in this case is given by 1 degree, and the superscript "u" represents the upper surface of a reference blade and "l" refers the blade lower surface.

The computational mesh used in the present time-linearized Euler calculation is 90×30 and the mesh in axial direction is slightly squeezed around the blade leading and trailing edges in order to give a better flow resolution. The calculated real part and imaginary part of the unsteady pressure coefficient jump for the lower frequency case (k=0.57) is compared to the results produced by LINSUB in Fig.3-1,

and an excellent comparison has been achieved even at the leading and trailing edges of the blade. A similar good comparison has also been obtained for the higher frequency case (k=1.714), as shown in Fig.3-2.

3.1.2 High Frequency Incoming Wakes

In order to assess the ability of the present time-linearized Euler method for handling the forced response problems in turbomachinery, the unsteady flows around flat plate induced by unsteady incoming wakes have been calculated.

In this calculation, the cascade geometry is

Chord:	C = 0.1m
Solidity:	C / Pitch = 2.0
Stagger angle:	$\gamma = 30^0$

and the steady flow has a Mach number of 0.7 and zero incidence.

The unsteady flow in this forced response problem is induced by an unsteady incoming wake. The wake has a pitch which is 90% of the blade pitch. In the present calculations, the unsteady flows induced by the wakes from two different incoming angles are considered, one is 0^0, the other is -30^0. For the 0^0 case, it produces a reduced frequency (based on axial velocity and axial chord) of 6.98 . For the -30^0 case, it produces a reduced frequency of 13.96. According to the Eq. (1-4), the pitch ratio between the wake and cascade in this calculation produces an inter-blade phase angle of -40^0.

The wake in this calculation is prescribed by assuming a uniform static pressure, uniform total enthalpy and a simple sinusoidal form of velocity defect across

the wake, so the unsteady perturbation amplitude of the incoming wake can be given by

$$\tilde{P}_{inl} = 0.0$$

$$\tilde{u}_{inl} = A_m \sqrt{\hat{u}_{inl}^2 + \hat{v}_{inl}^2}\cos(\beta_{wake})$$

$$\tilde{v}_{inl} = A_m \sqrt{\hat{u}_{inl}^2 + \hat{v}_{inl}^2}\sin(\beta_{wake})$$

where β_{wake} is the angle of incoming wake and it is 0^0 or -30^0 for current two cases. A_m is the amplitude of the wake velocity defect and is given by 1% in the calculation. The amplitude of the wake density, $\tilde{\rho}_{inl}$, can be worked out by linearizing the following nonlinear relationship

$$\rho_{inl} = \frac{\gamma}{\gamma - 1}\frac{P_{inl}}{\left(C_p T^*_{inl} - \frac{1}{2}(u_{inl}^2 + v_{inl}^2)\right)} \tag{3-3}$$

where T^*_{inl} is the total temperature and is constant in the wake frame. For the wake in this calculation, $\tilde{\rho}_{inl}$ is given by

$$\tilde{\rho}_{inl} = \frac{\gamma}{\gamma - 1}\frac{\hat{P}_{inl}}{C_p \hat{T}_{inl}}(\hat{u}_{inl}\tilde{u}_{inl} + \hat{v}_{inl}\tilde{v}_{inl}) \tag{3-4}$$

where C_p is the gas constant and γ is the ratio of gas specific heat. $\hat{T}_{inl}$ is the amplitude of the unsteady temperature at the inlet.

In this validation, the predicted amplitudes of the unsteady pressure coefficient jump by the time-linearized Euler method are also compared to the results produced by LINSUB. In this calculation the unsteady pressure coefficient is defined by

$$\tilde{c}_p = \frac{\tilde{P}}{\hat{\rho}_{inl}\hat{w}_{inl}w_{ref}} \tag{3-5}$$

where w_{ref} is the velocity which would be induced at the leading edge of the blade by inlet wakes (positive up), if the cascade were removed,

In order to resolve the high frequency unsteadiness, a fine mesh with a size of 350×40 is used in this calculation. For the first case with the wake angle of 0^0 degree, a contour map of the first harmonic entropy is presented in Fig.3-3. The contour map of the first harmonic pressure is presented in Fig.3-4. It can be clearly seen that the incoming wake propagates downstream. The complex amplitudes of unsteady pressure coefficient jump predicted by the present linear method are compared with LINSUB in Fig.3-5, and the comparison is good. The computational results for the case with wake angle of -30^0 degrees are given in Fig.3-6 to Fig.3-8. It can be seen that the unsteady wake propagation is well predicted by the presented calculation, a reasonable comparison between current calculation and LINSUB is also achieved even for the unsteady flow with a very high frequency. For both cases, their first harmonic pressure contours suggest that the non-reflection of outgoing pressure waves is well kept at the inlet by applying the 2-D nonreflecting boundary conditions, but at the outlet some reflections can be seen. The reason is not quite clear. This problem is noted in Giles' computational results as well (Giles, 1990b).

3.1.3 Fourth Standard Configuration

To validate the present quasi 3-D time-linearized Euler method in a more practical condition, an unsteady flow through an oscillating turbine cascade has been calculated. This is the fourth standard configuration in the Aeroelasticity Workshop (Bölcs and Fransson, 1986). In this workshop, nine standard configurations about the

unsteady flows around oscillating blades were collected, and experimental data are available in the first seven configurations. For each configuration, different numerical methods were used to calculate the unsteady flows and the numerical results were compared to the experimental data. Because of the difficulty for the experimental study of unsteady flows in turbomachinery, especially for the blade flutter, the Aeroelasticity Workshop is invaluable for understanding blade flutter and validating numerical methods.

The fourth standard configuration is a case in which a turbine cascade oscillated in a bending mode under different frequencies and inter-blade phase angles at high subsonic or transonic flow conditions. The cascade in this experiment is an annual turbine cascade and inlet guide vanes were used to induce swirl in the flow to produce the prescribed inlet flow angles. The cascade has a stagger angle of 56.6^0, hub to tip ratio of 0.8, aspect ratio of 0.538, and has 20 blades. In order to produce 2-D results, the blade profile is the same from hub to tip. In the present numerical study, the experimental Case 3 is considered. The flow condition in this case is given by

Inlet flow angle:	$\beta_{inl} = -45.0^0$
Inlet Mach number:	$M_{inl} = 0.28$
Outlet flow angle:	$\beta_{out} = -71.0^0$
Outlet Mach number:	$M_{out} = 0.9$

First, the steady flow is calculated by solving the steady flow equations. Numerical tests have shown that a linear variation of the streamtube height in the blade passage with a ratio of 1.1 has to be given to match the experimental time-averaged static pressure distribution on the blade surfaces. A good comparison between the calculated steady isentropic Mach number distribution and experimental data is shown in Fig.3-9.

Having calculated the steady flow, the unsteady flow due to blade bending in a direction nearly perpendicular to the chord line is calculated by solving the time-linearized perturbation equations. The reduced frequency of the blade oscillating is 0.12 (based on the blade semi-chord and inlet flow velocity). Here the unsteady flows under three different inter-blade phase angles, i.e. -90^0, 180^0, and 90^0 are calculated. The predicted amplitudes and phase angles of unsteady pressure coefficients on the blade surface are compared to the experimental data and the comparisons are given in Fig. 3-10 to Fig. 3-12. The comparisons have shown that the amplitudes in the front part of the suction surface are over-predicted under all three inter-blade phase angles and the trend of phase angle variations is reasonably predicted. The reason for the discrepancy between the predicted and experimental data is not known and it might be due to the three-dimensional effects in the experiment. A three-dimensional linear analysis by Hall and Lorence (1992) of this standard configuration has shown marked 3-D effects on the unsteady flow calculations, especially on the unsteady amplitudes, although this standard configuration was designed to be a two dimensional test case. Nevertheless, the predicted results by the present time-linearized Euler method are very similar to those produced by a nonlinear time-marching method (He, 1990b).

3.1.4 Tenth Standard Configuration

In order to validate the present time-linearized Euler method for transonic unsteady flows around oscillating compressor blades, the tenth standard configuration is calculated. This standard configuration was recently proposed by Fransson and Verdon (1993), in which a compressor cascade oscillates either in a torsion or a bending mode under different reduced frequencies and inter-blade phase angles. The airfoils of this cascade have a circular arc camber distribution with a maximum height of 5% of the chord. The thickness distribution is slightly modified from a NACA 5506 airfoil so that the trailing edge is wedged. The cascade has a stagger angle of 45^0 and a pitch/chord ratio of 1.0. The cascade operates in a subsonic flow condition or a

transonic flow condition with a weak shock on the blade suction surface. This standard configuration was extensively investigated by a time-linearized potential method (Verdon, 1993) and nonlinear time-marching methods (Huff, 1991, Ayer and Verdon, 1996). The comparison between the linear results and nonlinear results have shown that the nonlinear effects can be neglected in subsonic flow conditions but the nonlinear effects associated with the shock oscillation at transonic flow conditions could be potentially important.

In the present work, the transonic flow condition is considered with an inlet free stream Mach number of 0.8 and an inlet flow angle of 58^0. This flow condition is such that there is a supersonic patch on the suction surface of the blade. The steady flow Mach number contours at this flow condition are given in Fig. 3-13 and the steady isentropic Mach number distribution on the blade surfaces is shown in Fig.3-14. The supersonic patch and a weak shock at the end of the patch on the blade suction surface can be seen.

The unsteady flow in this case is induced by the blades bending with an inter-blade phase angle of -90 degree and a reduced frequency (based on the blade chord and upstream velocity) of 1.287. The calculated complex amplitudes of unsteady pressure coefficients are shown in Fig.3-15 and the unsteady shock impulse due to the shock oscillation can clearly be seen. The present results are compared to the results produced by a nonlinear time-marching method (Huff, 1991). The comparison is very good except the shock impulse predicted by the present linear method is slightly higher than that predicted by the nonlinear method. The present results are very similar to those predicted by other linear methods (Hall et al, 1994). This calculation shows that the time-linearized Euler methods are able to predict the unsteady shock impulse well as long as the nonlinear effects of shock oscillating are negligible.

3.2 Navier-Stokes Solutions

3.2.1 Unsteady Laminar Boundary Layer on Flat Plate

To validate the present linearized Navier-Stokes method, an unsteady laminar flow on a flat plat is numerically analysed. In this work, a model problem which was originally analytically studied by Lighthill (1954) is chosen. In this model problem, the unsteady incompressible laminar boundary layer is introduced by a small periodic fluctuation of the main stream velocity about a constant mean value, i.e.

$$U = U_0(1 + \varepsilon e^{i\omega t}) \tag{3-7}$$

where U_0 is the mean velocity of the main stream, ε is a small nondimensional parameter and it is much smaller than 1. This model problem later was investigated by Ackerberg and Philips (1972) by using a semi-analytic method, and was calculated by Cebeci (1977) by solving boundary layer equations using a finite difference method. For this model problem, Cebeci found that nonlinear effects are negligible if $\varepsilon \leq 0.15$.

To simulate this model problem, the unsteady laminar flow through a channel with a length of three times the half height of the channel is calculated by using the time-linearized Naiver-Stokes method. The unsteadiness in the calculation is introduced by the back pressure oscillation of a small amplitude in a harmonic form while holding the inlet flow quantities fixed. To resolve the boundary layer, a fine mesh is arranged near the wall so that there are approximately 25 mesh points across the boundary layer near the channel exit. The non-slip wall boundary condition is applied in the calculations. In order to reduce the effect of compressibility of the flow, the main stream Mach number in the current investigation is kept to 0.1. The Reynolds number in the calculation is 150,000 based on the upstream velocity and the channel length.

In the present numerical analysis, the steady laminar boundary is obtained by solving the steady flow equations in the channel. The calculated steady laminar boundary layer profiles are compared to the analytical Balsius laminar boundary solutions in Fig. 3-16. The comparison shows that the laminar boundary layer in the present calculation is well resolved.

Having obtained the steady flow, the unsteady flow is introduced by prescribing a small amplitude of back pressure oscillation. It is noticed that the instantaneous main stream flow is uniform and there is no streamwise phase lag in the original analytical model. The numerical tests have shown that if the reduced frequency of the excitation is smaller than 2.5, the phase lag in the main stream in the present linear analysis can be neglected. The calculated unsteady velocity perturbation profiles at three different reduced frequencies are shown in Fig. 3-17. The reduced frequency here is defined by $\omega x / U_0$. In these figures, the boundary layer coordinate is defined by $y\sqrt{\rho U_0 / \mu x}$. The comparison with a semi-analytic solution by Ackerberg and Philips (1972) is good, importantly the "overshoots" of the real part of the unsteady velocity profiles, where the real part of U / U_e is bigger than 1.0 (U_e is the velocity on the boundary edge), are captured by the time-linearized Navier-Stokes method. The overshoots are produced by the boundary layer thins and then thickens as the outer flow speeds up and slows down. When the boundary layer thins, the outer inviscid flow is brought closer to the wall producing what appears to be a bulge in the perturbation velocity profile.

Fig.3-18 shows the calculated distribution of unsteady wall stress amplitudes and phase angles with the reduced frequency. The results are in a satisfactory agreement with Lighthill's (1954) results for both low and high frequencies, and with the numerical solutions by Cebeci (1977). The wall shear stress in Fig. 3-18 is defined by τ_1 / τ_0, where

$$\tau = \tau_0 + \varepsilon\tau_1 \cos(\omega t + \phi)$$

where τ_0 is the wall shear for Blasius flow.

3.2.2 Unsteady Turbulent Boundary Layer on Flat Plate

To check the present time-linearized Navier-Stokes method for unsteady turbulent flows, an unsteady turbulent boundary layer on the flat plate is calculated. This low speed unsteady turbulent flow has zero mean pressure gradient in the flow direction and was experimentally studied by Karlsson (1959) in a boundary layer wind tunnel. The mean velocity in the experiment was very low and was about 5.33 m/s. The measurements were made at the location where the Reynolds number was about 3.6×10^3. Here the Reynolds number is based on the free stream mean velocity and boundary layer displacement thickness, defined by

$$Re_{\delta^*} = U_0\delta^* / \nu \qquad (3\text{-}9)$$

where

$$\delta^* = \int_0^\infty \left(1 - \frac{U}{U_0}\right) dy$$

In the experiment, the turbulent boundary layer thickness was about 0.00762 m at the measuring section, the local skin friction coefficient, c_f, was approximately 0.0034. The free stream fluctuations were obtained by a shutter consisting of four parallel rotating vanes driven by an electric motor at the exit of the wind tunnel. The unsteady boundary measurements were carried out under several frequencies, i.e. 0 (quasi-steady), 0.33, 0.66, 1.0, 3.3, 2.0, 4.0, 7.68 and 48 Hz. At each frequency, except 0

and 48 Hz, the free stream velocity fluctuation amplitudes varies from about 8% ~ 34% of the free stream mean velocity. The experiment observed that the nonlinear effects were very small, even for fluctuation amplitudes as large as 34 %. The linear method can be used to analyse this experimental case. Because only limited experimental data for unsteady turbulent boundary layers are available, Karlsson's experiment is valuable for validating the numerical methods. This test case was numerically studied by Cebeci (1977).

In the present linear analysis by the time-linearized Navier-Stokes method, the unsteady flow is introduced by prescribing a back pressure unsteady perturbation at the channel exit. A fine mesh is also used to resolve the boundary layer. In the calculation, the free stream Mach number is 0.1 and a quite high input Reynolds number (based on the channel length and free stream mean velocity) is given to match the experimental Reynolds number Re_{δ^*}. Fig.3-19 gives the calculated turbulent boundary layer profile and it is compared to the experimental time-mean data. In order to compare with experimental data for unsteady flows, the unsteady perturbation equations are solved at three reduced frequencies which are identical to the experimental reduced frequencies under three physical frequencies (0.33, 1.0, and 4.0 Hz). Fig.3-20 to Fig. 3-22 have shown the comparisons between calculated and experimental unsteady turbulent profiles in three different reduced frequencies. The experiment data have shown that the "over-shoots" of in-phase components of velocity fluctuation amplitudes exist in all three frequencies, and the peak of the "over-shoot" gets closer to the wall with the increase of frequency. In the region close to the wall, the out-of-phase (imaginary part) components are always positive for all the frequencies. The comparisons between the calculated results and the experimental data show that the unsteady turbulent boundary layers are reasonably well predicted.

3.2.3 Fifth Standard Configuration

This configuration is a subsonic compressor cascade oscillating in a torsion mode around its mid-chord under a subsonic flow condition. In the experiment, the flow incidences are from 2^0 up to 6^0 and the unsteady pressured were measured. This standard configuration was numerically investigated by two time-linearized potential methods (Whitehead, 1982, Verdon and Caspar, 1984). In this configuration, the viscous effects could be important when the flow has a very high incidence. In the time-linear potential analysis by Verdon and Caspar(1984), the calculation had to be carried out at a different flow incidence from the experimental one in order to match the experimental data, the reason might be due to that the viscous effect was ignored in the calculations. In the present work, the time-linearized Navier-Stokes method is validated by calculating this standard configuration.

In the fifth standard configuration, the blade has a chord of 0.09 m, stagger angle of 59.3^0, and zero camber. The flow condition for the present numerical calculation is

Inlet Mach number: $M_{inl} = 0.5$

Flow incidence: $i = 4^0$

The unsteady flow is introduced by blade oscillating in torsion mode around its mid-chord with an amplitude of 0.0052 radian under a 180^0 inter-blade phase angle. The unsteady calculations are carried out at two reduced frequencies (based on the semi-chord and inlet flow velocity), 0.14 and 1.02. In the calculation, the input flow incidence is kept the same as the experimental incidence(4^0) and the flow is assumed to be fully turbulent from the leading edge. The slip-wall boundary condition is imposed for solving both the steady and time-linearized Navier-Stokes equations.

For the steady flow calculation, the predicted steady pressure coefficients are compared with experimental data in Fig. 3-23. Because of the high incidence, it can be seen that the aerodynamic loading concentrates around the blade leading edge. For the unsteady flow calculation at the reduced frequency of 0.14, the calculated amplitudes and phase angles of unsteady pressure coefficients are given in Fig. 3-24 and they are in a very good agreement with the experimental data. For the case with the reduced frequency of 1.02, the results are shown in Fig.3-25 and it can be seen that the amplitudes of unsteady pressure are well predicted, but there is a marked discrepancy of phase angles between the calculated and the experimental data, especially around the trailing edge on the pressure surface. It should be noted that the present calculation results are very similar to those produced by time-linearized potential methods.

3.3 Summary

In this chapter, the validations of the time-linearized Navier-Stokes/Euler method described in Chapter 2, are presented. In the first part, the calculations of inviscid unsteady flows in a flat plate cascade induced by blade oscillation and incoming unsteady wakes have shown excellent agreements with the results produced by a well-established semi-analytical linear method LINSUB. A fair comparison with the experimental data is achieved for the calculation of the fourth standard configuration, and the 3-D effects are likely to be blamed for the discrepancy. For the computation of a transonic compressor oscillating cascade, the comparison of computational results between the present time-linearized Euler method and a well-developed nonlinear time-marching Euler method is very good. For the validation of the time-linearized Navier-Stokes method, calculated results for an unsteady laminar and a turbulent boundary layer are compared well with analytical solutions, experimental data and other numerical methods. Finally the validation is carried out by calculating the fifth standard configuration using the time-linearized Navier-Stokes method, and the results compare reasonably well with the experimental data.

It should be pointed out that all the test cases considered here have no or little nonlinear effects. An important issue of the nonlinear effects and the validity of the linear analysis has not been addressed. More test cases concerning this issue will be presented in Chapter 4.

Chapter 4 Nonlinear Harmonic Method

As presented in last two chapters, a time-linearized Navier-Stokes/Euler method is developed and validated. The main feature of the time-linearized method is its high computational efficiency compared to the nonlinear time-marching methods. However, the application of the linear methods is restricted to the linear problems due to the linear assumption. Although the onset of flutter in turbomachinery is widely accepted to be a linear aeroelastic phenomenon in most circumstances, the nonlinear effects with the shock oscillation, finite amplitude excitation, and flow separations can be potentially important. The forced response of blade unsteady forces to nonuniformity of unsteady flow fields(e.g. incoming wake, potential interaction, and inlet distortion etc.) is not necessarily a linear phenomenon. It is highly desirable to develop a numerical method which has a high computational efficiency like the conventional time-linearized methods, while can include the nonlinear effects like the nonlinear time-marching methods.

The work in this chapter is based on the nonlinear harmonic approach proposed by He (1996a) which is introduced in Chapter 1. The emphasis in this chapter is to develop this approach into a new quasi-3D nonlinear harmonic Navier-Stokes/Euler method in which the nonlinear effects can be effectively included.

4.1 Time-Averaged Equations

Compared to the conventional time-linearized method, an important change in the nonlinear harmonic method is that the **time-averaged flow** field (instead of **steady**) is used to be the base of unsteady perturbations. The unsteady flow is assumed to be a time-averaged flow plus a small perturbation, i.e.

$$U = \overline{U} + U' \tag{4-1}$$

where

$$\overline{U} = h\begin{pmatrix} \overline{\rho} \\ (\overline{\rho u}) \\ r(\overline{\rho v}) \\ (\overline{\rho e}) \end{pmatrix} \tag{4-2}$$

and

$$U' = h\begin{pmatrix} \rho' \\ (\rho u)' \\ r(\rho v)' \\ (\rho e)' \end{pmatrix} \tag{4-3}$$

where the $\overline{U}$ is the vector of the time-averaged conservative variables, U' is the vector of the perturbations to the time-averaged variables. The viscous terms can also be assumed to be a steady part plus a perturbation.

Similarly, assuming that the computational grid can be expressed by its steady or mean position plus a small perturbations, i.e.

$$x = \overline{x} + x', \quad y = \overline{y} + y' \tag{4-4}$$

The grid moving velocities are also divided to be a mean part plus a perturbation, i.e.

$$u_g = \overline{u}_g + u'_g, \quad v_g = \overline{v}_g + v'_g \tag{4-5}$$

Substituting the expression of (4-1), (4-4) and (4-5) into the original nonlinear Navier-Stokes/Euler integral equation (2-1), and time-averaging it, the resultant time-averaged Navier-Stokes/Euler Equation can be given by:

$$\oint_s[(\overline{F}-\overline{V}_x)d\overline{y}+(\overline{G}-\overline{V}_y)d\overline{x}+\overline{(F'dy')}+\overline{(G'dx')}-\overline{(v'_x dy')}-\overline{(v'_y dx')}]$$

$$=\iint_{\Delta A}(\overline{S}d\overline{A}+\overline{(S'dA')} \tag{4-6}$$

where

$$\overline{F}=h\begin{pmatrix}\overline{\rho u}-\overline{\rho u_g}\\ (\overline{\rho u}-\overline{\rho u_g})\overline{u}+\overline{P}+\overline{(\rho u)'u'}-\overline{(\rho u_g)'u'}\\ r[(\overline{\rho u}-\overline{\rho u_g})\overline{v}+\overline{(\rho u)'v'}-\overline{(\rho u_g)'v'}]\\ (\overline{\rho u}-\overline{\rho u_g})\overline{e}+\overline{P}\overline{u}+\overline{P'u'}+\overline{(\rho u)'e'}-\overline{(\rho u_g)'e'}\end{pmatrix} \tag{4-7}$$

$$\overline{G}=h\begin{pmatrix}\overline{\rho v}-\overline{\rho v_g}\\ (\overline{\rho v}-\overline{\rho v_g})\overline{u}+\overline{(\rho v)'u'}-\overline{(\rho v_g)'u'}\\ r[(\overline{\rho v}-\overline{\rho v_g})\overline{v}+\overline{P}+\overline{(\rho v)'v'}-\overline{(\rho v_g)'v'}]\\ (\overline{\rho v}-\overline{\rho v_g})\overline{e}+\overline{P}\overline{v}+\overline{P'v'}+\overline{(\rho v)'e'}-\overline{(\rho v_g)'e'}\end{pmatrix} \tag{4-8}$$

and

$$\overline{V}_x=h\begin{pmatrix}0\\ \overline{\tau}_{xx}\\ r\overline{\tau}_{xy}\\ -\overline{q}_x+\overline{u}\overline{\tau}_{xx}+\overline{v}\overline{\tau}_{xy}+\overline{u'\tau'_{xx}}+\overline{v'\tau'_{xy}}\end{pmatrix} \tag{4-9}$$

$$\overline{V}_y=h\begin{pmatrix}0\\ \overline{\tau}_{xy}\\ r\overline{\tau}_{yy}\\ -\overline{q}_y+\overline{u}\overline{\tau}_{xy}+\overline{v}\overline{\tau}_{yy}+\overline{u'\tau'_{xy}}+\overline{v'\tau'_{yy}}\end{pmatrix} \tag{4-10}$$

where

$$\bar{\tau}_{xx} = \frac{2}{3}\mu(2\frac{\partial \bar{u}}{\partial x} - \frac{\partial \bar{v}}{\partial y}), \quad \bar{\tau}_{yy} = \frac{2}{3}\mu(2\frac{\partial \bar{v}}{\partial y} - \frac{\partial \bar{u}}{\partial x}), \quad \bar{\tau}_{xy} = \mu(\frac{\partial \bar{u}}{\partial y} + \frac{\partial \bar{v}}{\partial x})$$

$$\bar{q}_x = -k\frac{\partial \bar{T}}{\partial x}, \qquad \bar{q}_y = -k\frac{\partial \bar{T}}{\partial y}$$

The non-conservative time-averaged variables in the above equations can be worked out from the conservative time-averaged variables by following formulations,

$$\bar{u} = \left[\overline{\rho u} - \overline{\rho' u'}\right] / \bar{\rho} \tag{4-11}$$

$$\bar{v} = \left[\overline{\rho v} - \overline{\rho' v'}\right] / \bar{\rho} \tag{4-12}$$

$$\bar{e} = \left[\overline{\rho e} - \overline{\rho' e'}\right] / \bar{\rho} \tag{4-13}$$

$$\bar{P} = (\gamma - 1)\left[\overline{\rho e} - \frac{1}{2}(\overline{\rho u}\bar{u} + \overline{\rho v}\bar{v}) - \frac{1}{2}\overline{(\rho u)' u'} - \frac{1}{2}\overline{(\rho v)' v'}\right] \tag{4-14}$$

The comparison between the time-averaged equation (4-6) and the steady form of the original unsteady equation (2-1) shows that the time-averaging generates extra terms. There are two kinds of extra terms, one kind is generated by the computational grid movement such as $\overline{F' dy'}$, the other kind is produced due to the nonlinearity of flow governing equations such as $\overline{(\rho u)' v'}$, which is similar to the turbulence (Reynolds) stress terms. The second kind of extra terms is called "unsteady stress" terms in the present work and they only exist in the momentum and energy equations. The effects of the "unsteady stress" terms depend on the spatial gradients of the unsteady disturbances.

Normally the amplitude of grid motion in a blade flutter analysis is very small, the extra terms produced by grid movement in the equation (4-6) are assumed to be

small quantity terms and are neglected in the present method. So the time-averaged form of the governing equation can be re-written by:

$$\oint_s[(\overline{F}-\overline{V}_x)d\overline{y}+(\overline{G}-\overline{V}_y)d\overline{x}]=\iint_{\Delta A}\overline{S}d\overline{A} \qquad (4\text{-}15)$$

Comparing the time-averaged equation (4-6) to the steady form of the governing equation (2-1), the mass continuity equation remains unchanged, the "unsteady stress" terms appear in the time-averaged momentum and energy equations. To solve the time-averaged equation (4-15), the extra relationships or models are required to make the equation closed, similar to that the turbulence models are needed to close the Reynolds-averaged Navier-Stokes equations. If these unsteady stress terms are zero, the time-averaged equation (4-15) is reduced to the conventional steady flow equation.

4.2 First Harmonic Perturbation Equations

Substituting the equations (4-1), (4-4) , and (4-5) into the original flow governing equation (2-1) and then subtracting the time-averaged equation (4-6), the unsteady perturbation equation is given by

$$\frac{\partial}{\partial t}\iint_{\Delta A}(\overline{U}dA'+U'd\overline{A})+\oint_s\left[(\overline{F}-\overline{V}_x)dy'+(\overline{G}-\overline{V}_y)dx'+(F'-V_x')d\overline{y}+(G'-V_y')d\overline{x}\right]$$
$$=\iint_{\Delta A}(S'd\overline{A}-\overline{S}dA') \qquad (4\text{-}16)$$

where

$$F' = h\begin{pmatrix} (\rho u)' - (\rho u_g)' \\ (\overline{\rho u} - \overline{\rho u_g})u' + [(\rho u)' - (\rho u_g)']\bar{u} + P' - \overline{(\rho u)'u'} + \overline{(\rho u_g)'u'} \\ r[(\overline{\rho v} - \overline{\rho v_g})u' + [(\rho v)' - (\rho v_g)']\bar{u} - \overline{(\rho v)'u'} + \overline{(\rho v_g)'u'}] \\ [\overline{\rho e} + \bar{P}]u' + [(\rho e)' + P']\bar{u} - \overline{\rho e}u'_g - (\rho e)'\bar{u}_g - \overline{(\rho e)'u'} - \overline{P'u'} + \overline{(\rho e)'u'_g} \end{pmatrix} \tag{4-17}$$

$$G' = h\begin{pmatrix} (\rho v)' - (\rho v_g)' \\ (\overline{\rho v} - \overline{\rho v_g})u' + [(\rho v)' - (\rho v_g)']\bar{u} - \overline{(\rho v)'u'} + \overline{(\rho v_g)'u'} \\ r[(\overline{\rho v} - \overline{\rho v_g})v' + [(\rho v)' - (\rho v_g)']\bar{v} + P' - \overline{(\rho v)'v'} + \overline{(\rho v_g)'v'}] \\ [\overline{\rho e} + \bar{P}]v' + [(\rho e)' + P']\bar{v} - \overline{\rho e}v'_g - (\rho e)'\bar{v}_g - \overline{(\rho e)'v'} - \overline{P'v'} + \overline{(\rho e)'v'_g} \end{pmatrix} \tag{4-18}$$

and

$$V'_x = h\begin{pmatrix} 0 \\ \tau'_{xx} \\ r\tau'_{xy} \\ -q'_x + u'\bar{\tau}_{xx} + v'\bar{\tau}_{xy} + \bar{u}\tau'_{xx} + \bar{v}\tau'_{xy} - \overline{u'\tau'_{xx}} - \overline{v'\tau'_{xy}} \end{pmatrix} \tag{4-19}$$

$$V'_x = h\begin{pmatrix} 0 \\ \tau'_{xy} \\ r\tau'_{yy} \\ -q'_y + u'\bar{\tau}_{xy} + v'\bar{\tau}_{yy} + \bar{u}\tau'_{xy} + \bar{v}\tau'_{yy} - \overline{u'\tau'_{xy}} - \overline{v'\tau'_{yy}} \end{pmatrix} \tag{4-20}$$

The complete form of the unsteady perturbation equation (4-16) is not readily solvable if a frequency-domain harmonic approach is to be used. It is assumed that the unsteady perturbation is dominated by the 1st order terms. Effectively, the second order terms in the unsteady perturbation equation (4-16) are neglected. The resultant first order form of fluxes (4-17) to (4-20) can be re-written into

$$F' = h\begin{pmatrix} (\rho u)' - (\rho u_g)' \\ (\overline{\rho u} - \overline{\rho u_g})u' + [(\rho u)' - (\rho u_g)']\overline{u} + P' \\ r[(\overline{\rho v} - \overline{\rho v_g})u' + [(\rho v)' - (\rho v_g)']\overline{u}] \\ [\overline{\rho e} + \overline{P}]u' + [(\rho e)' + P']\overline{u} - \overline{\rho e}u'_g - (\rho e)'\overline{u}_g \end{pmatrix} \tag{4-21}$$

$$G' = h\begin{pmatrix} (\rho v)' - (\rho v_g)' \\ (\overline{\rho v} - \overline{\rho v_g})u' + [(\rho v)' - (\rho v_g)']\overline{u} \\ r[(\overline{\rho v} - \overline{\rho v_g})v' + [(\rho v)' - (\rho v_g)']\overline{v} + P'] \\ [\overline{\rho e} + \overline{P}]v' + [(\rho e)' + P']\overline{v} - \overline{\rho e}v'_g - (\rho e)'\overline{v}_g \end{pmatrix} \tag{4-22}$$

and

$$V'_x = h\begin{pmatrix} 0 \\ \tau'_{xx} \\ r\tau'_{xy} \\ -q'_x + u'\overline{\tau}_{xx} + v'\overline{\tau}_{xy} + \overline{u}\tau'_{xx} + \overline{v}\tau'_{xy} \end{pmatrix} \tag{4-23}$$

$$V'_y = h\begin{pmatrix} 0 \\ \tau'_{xy} \\ r\tau'_{yy} \\ -q'_y + u'\overline{\tau}_{xy} + v'\overline{\tau}_{yy} + \overline{u}\tau'_{xy} + \overline{v}\tau'_{yy} \end{pmatrix} \tag{4-24}$$

In order to use a frequency domain method, it is further assumed that the unsteady perturbation varies in a harmonic mode in time, i.e.

$$U' = \tilde{U}e^{i\omega t} \tag{4-25}$$

where $\tilde{U}$ is the vector of conservative variable amplitudes. The moving grid and moving velocities have similar harmonic forms.

Substituting all the harmonic expressions into the unsteady perturbation equation (4-16), the first order harmonic perturbation equation becomes

$$\oint_s \left[(\overline{F} - \overline{V}_x)d\tilde{y} + (\overline{G} - \overline{V}_y)d\tilde{x} + (\tilde{F} - \tilde{V}_x)d\overline{y} + (\tilde{G} - \tilde{V}_y)d\overline{x} \right]$$

$$= \iint_{\Delta A} (\tilde{S}d\overline{A} + \overline{S}d\tilde{A}) - i\omega \iint_{\Delta A} \tilde{U}d\overline{A} - i\omega \iint_{\Delta A} \overline{U}d\tilde{A} \qquad (4\text{-}26)$$

where

$$\tilde{F} = h \begin{pmatrix} (\tilde{\rho u}) - (\tilde{\rho u_g}) \\ (\overline{\rho u} - \overline{\rho u_g})\tilde{u} + [(\tilde{\rho u}) - (\tilde{\rho u_g})]\overline{u} + \tilde{P} \\ r[(\overline{\rho v} - \overline{\rho v_g})\tilde{u} + [(\tilde{\rho v}) - (\tilde{\rho v_g})]\overline{u}] \\ [\overline{\rho e} + \overline{P}]\tilde{u} + [(\tilde{\rho e}) + \tilde{P}]\overline{u} - \overline{\rho e}\tilde{u}_g - (\tilde{\rho e})\overline{u}_g \end{pmatrix}$$

$$\tilde{G} = h \begin{pmatrix} (\tilde{\rho v}) - (\tilde{\rho v_g}) \\ (\overline{\rho v} - \overline{\rho v_g})\tilde{u} + [(\tilde{\rho v}) - (\tilde{\rho v_g})]\overline{u} \\ r[(\overline{\rho v} - \overline{\rho v_g})\tilde{v} + [(\tilde{\rho v}) - (\tilde{\rho v_g})]\overline{v} + \tilde{P}] \\ [\overline{\rho e} + \overline{P}]\tilde{v} + [(\tilde{\rho e}) + \tilde{P}]\overline{v} - \overline{\rho e}\tilde{v}_g - (\tilde{\rho e})\overline{v}_g \end{pmatrix}$$

and

$$\tilde{V}_x = h \begin{pmatrix} 0 \\ \tilde{\tau}_{xx} \\ r\tilde{\tau}_{xy} \\ -\tilde{q}_x + \tilde{u}\overline{\tau}_{xx} + \tilde{v}\overline{\tau}_{xy} + \overline{u}\tilde{\tau}_{xx} + \overline{v}\tilde{\tau}_{xy} \end{pmatrix}$$

$$\tilde{V}_y = h\begin{pmatrix} 0 \\ \tilde{\tau}_{xy} \\ r\tilde{\tau}_{yy} \\ -\tilde{q}_y + \tilde{u}\overline{\tau}_{xy} + \tilde{v}\overline{\tau}_{yy} + \overline{u}\tilde{\tau}_{xy} + \overline{v}\tilde{\tau}_{yy} \end{pmatrix}$$

Actually the first order harmonic perturbation equation (4-26) has the same form as the unsteady perturbation equation (2-12) in the time-linearized method. However, the equation (4-26) is only quasi-linear, i.e. the perturbations are linear for a given time-averaged flow field. Indeed, if the time-averaged flow is the same as the steady flow, the above first harmonic perturbation equation reduces to the conventional time-linearized perturbation equation.

4.3 Pseudo Time Dependence and Spatial Discretization

Similar to the time-linearized Navier-Stokes/Euler method in Chapter 2, the pseudo-time (t') is introduced to make both the time-averaged equation (4-11) and the first harmonic perturbation equation (4-26) time-dependent. The modified time-averaged equation and the first order perturbation equation can be given by:

$$\frac{\partial}{\partial t'}\iint_{\Delta A}\overline{U}d\overline{A} + \oint_s[(\overline{F}-\overline{V}_x)d\overline{y} + (\overline{G}-\overline{V}_y)d\overline{x}] = \iint_{\Delta A}\overline{S}d\overline{A} \qquad (4\text{-}27)$$

and

$$\frac{\partial}{\partial t'}\iint_{\Delta A}\tilde{U}d\overline{A} + \oint_s\left[(\overline{F}-\overline{V}_x)d\tilde{y} + (\overline{G}-\overline{V}_y)d\tilde{x} + (\tilde{F}-\tilde{V}_x)d\overline{y} + (\tilde{G}-\tilde{V}_y)d\overline{x}\right]$$
$$= \iint_{\Delta A}(\tilde{S}d\overline{A} + \overline{S}d\tilde{A}) - i\omega\iint_{\Delta A}\tilde{U}d\overline{A} - i\omega\iint_{\Delta A}\overline{U}d\tilde{A} \qquad (4\text{-}28)$$

Now both the time-averaged equation (4-27) and the first order harmonic perturbation equation (4-28) are hyperbolic in a pseudo-time domain. They can be solved by any time-marching integration schemes.

The cell-vertex finite volume scheme is used again to descretize both the time-averaged equation and the first order harmonic perturbation equation spatially. To suppress numerical oscillations and capture the time-averaged shock and the shock impulse in the calculations, a 2nd order and 4th order adaptive smoothing is used. The semi-discrete forms of the time-averaged equation and the 1st order harmonic equation are in similar forms as Eq.(2-15) and Eq.(2-16) in the time-linearized method. The only modification in this nonlinear harmonic method is the treatment of the pressure sensor in the artificial smoothing terms. The pressure sensor as shown in (2-22) is a nonlinear term and its nonlinearity is neglected in the time-linearized Navier-Stokes/Euler method. However, its nonlinearity cannot be ignored in the cases with strong nonlinear effects, so it is desirable to linearize the pressure sensor. However, it is recognised that an accurate way to linearize the pressure sensor is not easy to achieve(Linguist, 1991). In the present work, an approximate approach is used to partially linearize the pressure sensor (He, 1997c). The modified form of the pressure sensor is given by

$$\theta_{ij}^{(2)} = \left|\frac{\overline{P}_{i-1j} - 2\overline{P}_{ij} + \overline{P}_{i+1j}}{\overline{P}_{i-1j} + 2\overline{P}_{ij} + \overline{P}_{i+1j}}\right| + 0.5\frac{\left|\tilde{P}_{i+1j} - 2\tilde{P}_{ij} + \tilde{P}_{i-1j}\right|}{\overline{P}_{i+1j} + 2\overline{P}_{ij} + \overline{P}_{i+1j}} \qquad (4\text{-}29)$$

It can be seen that the modified pressure sensor is proportional to the local unsteadiness and the time-averaged effects of the nonlinear behaviour of pressure sensor can be included.

4.4 Coupling Between Time-averaged Flow and Unsteady Perturbations

So far, the time-averaged equation (4-27) is not closed, the extra relationships are needed to work out the "unsteady stress" terms. For a periodically unsteady flow, these terms can be directly evaluated in terms of the phase and amplitude of the unsteady perturbations. For example, u' and v' are two unsteady quantities changing in the harmonic forms, i.e.

$$u' = A_u \sin(\omega t + \phi_u)$$

and

$$v' = A_v \sin(\omega t + \phi_v)$$

Time-averaging $u'v'$ over one unsteady period T or $\omega t = 2\pi$ is:

$$\begin{aligned}\overline{u'v'} &= \frac{1}{T}\int_0^T u'v'dt \\ &= \frac{1}{2\pi}\int_0^{2\pi} A_u A_v \sin(\omega t + \phi_u)\sin(\omega t + \phi_v)d(\omega t) \\ &= \frac{1}{2}A_u A_v \cos(\phi_u - \phi_v) \qquad (4\text{-}30)\end{aligned}$$

where A_u and A_v are the amplitudes of the u' and v'. By using the relationship (4-30), the "unsteady stress" terms can be easily worked out if the unsteady perturbations are already known. The unsteady perturbations are obtained by solving the first order harmonic perturbation equations which the coefficients are formed from the time-averaged solution. Therefore, the time-averaged equation and the first order harmonic perturbation equation interact each other. For solving time-averaged equation, the extra terms are evaluated from the solution of the first order

perturbation equation, while the coefficients of the perturbation equation are evaluated from the solution of the time-averaged equation. Because of this interaction, these two equations now cannot be solved separately and a coupling procedure has to be used to integrate these two equations in a pseudo-time domain.

There two kinds of coupling methods can be used, one is the loose coupling, another is the strong coupling. In a loose coupling procedure, the time-averaged equation and the perturbation equation are solved alternately. For example, a steady flow field is firstly obtained by solving the steady equation and the linearized perturbation equation is solved on the steady flow. Then the "unsteady stress" terms are worked out by unsteady perturbations and they are put into the time-averaged equations, the time-averaged flow is generated by solving the time-averaged equation. Finally the perturbation equation is solved again on the time-averaged flow base. This loose coupling procedure is simple but only suitable for unsteady flows with weak nonlinearity.

For the flow with strong nonlinearity, the strong coupling has to be used. The key point is that the time-averaged equation and the first order harmonic perturbation equation have to be solved without any hierarchy. In the present work, a strong coupling technique proposed by He (1994b) for a fluid-structure coupling is implemented to time-march both the time-averaged equation (4-27) and the first order harmonic equation (4-28) simultaneously in a pseudo-time domain. The final converged solution includes a time-averaged flow field and the unsteady perturbations. Numerical tests (He, 1994b) have shown that the strong coupling is important in terms of solution convergence and accuracy when the interaction between two sets of equations becomes strong.

For the time integration for both the time-averaged equation and the first harmonic perturbation equation, again the 4-stage Runge-Kutta time-marching scheme is used. The formulations of the this scheme are the same as that introduced in

Chapter 2. The strong coupling procedure by using the 4-stage Runge-Kutta time-marching scheme for solving the time-averaged and first harmonic perturbation equations is illustrated in Fig. 4-1.

The boundary conditions applied in this nonlinear harmonic Navier-Stokes/Euler method are the same as those used in the time-linearized method as presented in Chapter 2, the only difference is that the steady flow variables in the boundary conditions are replaced by the time-averaged variables.

4.5 Summary

In this Chapter, a novel quasi-3D nonlinear harmonic Navier-Stokes/Euler method has been developed based on a nonlinear harmonic methodology proposed by He (1996a). Compared to the time-linearized method as presented in Chapter 2, the nonlinear harmonic method has three distinctive features. First of all, the time-averaged flow is used to be the base of the unsteady perturbations. Due to the nonlinearity of original unsteady flow governing equations, time-averaging generates extra nonlinear "unsteady stress" terms in the momentum and energy equations. Secondly, a strongly coupling method has to be used to solve the time-averaged equation and the first order harmonic equation simultaneously in a pseudo-time domain. The coupled solution includes time-averaged flow quantities and unsteady perturbations. The unsteady stress terms in time-averaged equations are produced from the unsteady perturbation solutions, while the coefficients of first order harmonic perturbation equations are formed from time-averaged solutions. Finally, for the unsteady transonic flows with strong nonlinearity induced by the shock oscillation, an approximate method is applied to linearize the pressure sensors in the artificial smoothing terms. The time-averaged effects of the nonlinear pressure sensors can be included.

The solution methods for this nonlinear harmonic method are the same as those used in the time-linearized method developed in Chapter 2. It implies that it is very straightforward to extend a well-developed time-linearized Navier-Stokes/Euler method into a nonlinear harmonic method. Compared to the linear methods, the extra CPU time for the nonlinear harmonic analysis is for evaluation of unsteady stress terms and it is relatively small, therefore it is still much more computational efficient than the nonlinear time-marching methods.

Chapter 5 Validations for Nonlinear Harmonic Method

5.1 Introduction

A novel quasi 3-D nonlinear harmonic Navier-Stokes/Euler method has been presented in Chapter 4. Compared to the conventional time-linearized methods, the fundamental difference is that the time-averaged flow is used to be the base of the unsteady perturbations in the nonlinear harmonic analysis. Therefore the nonlinear effects can be included in a coupling solution between the time-averaged flow and the unsteady perturbations. However, the solution methods of the nonlinear harmonic method are very similar to those used in the time-linearized method described in Chapter 2. In the present work, both methods are incorporated in the same computer code. To do the linear analysis, one simply switches off the extra unsteady stress terms in the time-averaged equations, so that the time-averaged equation becomes a steady equation and the first order harmonic equation reduces to a time-linearized perturbation equation. The validation of the baseline time-linearized code has been presented in Chapter 3. In this Chapter, the numerical results by the nonlinear harmonic method will be presented and compared to the numerical results produced by the time-linearized method, a nonlinear time-marching method, and experimental data. The time-linearized method in this chapter refers to the method described in Chapter 2.

Although the major objective in this chapter is to assess the effectiveness of the novel nonlinear harmonic analysis, the limitation of the conventional linear analysis will also be addressed and demonstrated by the numerical results.

5.2 Inviscid Transonic Unsteady Channel Flow

To test the present nonlinear harmonic Euler method, the unsteady inviscid transonic flow through a diverging channel is considered. This case is presented to

demonstrate the ability of the nonlinear harmonic analysis for capturing the nonlinear effects associated with considerably large amplitudes of shock oscillation. To assess the nonlinear harmonic analysis, the unsteady flows are also calculated by the time-linearized Euler method, and a nonlinear time-marching Euler method (He, 1990b). In the comparison between different numerical methods, the nonlinear time-marching analysis is the benchmark of the comparisons because of its good accuracy and nonlinear nature.

The diverging channel considered in the test case has a height of A, and its distribution along the axial direction is given by

$$A(x) = A_{inlet}\left\{1.10313 + 0.10313\tanh\left[10(x-\frac{1}{2})\right]\right\} \qquad (5\text{-}1)$$

where

$$0 \le x \le 1$$

(The units may be taken to be any consistent set of units). In the present study, A_{inlet} is taken to be 0.2 m. The flow at inlet is supersonic with a Mach number of 1.093. The ratio between the exit back pressure, P_{exit}, and the inlet total pressure, P_0, is 0.7422, so that the supersonic flow is terminated by a normal shock around the location of $x = 0.5\,m$. In the calculation, the mesh has 129×10 nodes, and the mesh is slightly squeezed around the location where x is around 0.5m in order to give a good shock resolution. For the calculations by the time-linearized method and nonlinear time-marching method, the same channel configuration, flow condition, and mesh size are used. A steady flow calculation for this transonic flow is carried out by solving the steady flow equations, the steady pressure distribution along the channel wall is given in Fig. 5-1. The steady result is compared well with an one-dimensional analytical solution as shown in Fig. 5-1. In this test case, two-dimensional effect is negligible.

The unsteady flow in this test case is introduced by a fluctuation of the back pressure at the channel exit in a harmonic form, i.e.

$$P_{exit} = \overline{P}_{exit}(1 + A_m \sin 2\pi ft) \tag{5-2}$$

where A_m is the amplitude of the back pressure fluctuation, and $\overline{P}_{exit}$ is the steady value of the back pressure in the linear analysis and time-averaged value in the nonlinear harmonic analysis. In the present calculations, two cases with an amplitude A_m of 1% and 7% are considered in order to produce a smaller amplitude and a larger amplitude of shock oscillation in the channel. f in the relationship (5-2) is the frequency of the back pressure fluctuation and is 167 Hz in the present calculations. The reduced frequency based on the inlet velocity and the channel inlet height is 0.63.

For the case with an amplitude of 1%, the unsteady flow is calculated by the present nonlinear harmonic method. The time-averaged pressure distribution along the channel wall by the nonlinear harmonic analysis is presented by marks in Fig. 5.1. It can be seen that the time-averaged solution and the steady solution are nearly identical. The shock oscillation is very small due to the small amplitude of back pressure fluctuation. As introduced in Chapter 1, the nonlinear effect in the unsteady flow is represented by the difference between the steady flow and the time-averaged flow. In this case, the nonlinear effect is apparently negligible. For the unsteady part, the calculated complex amplitudes of unsteady pressure coefficients by both the time-linearized method and the nonlinear harmonic method are presented in Fig.5-2. The difference between these two analyses is not apparently visible. Here the unsteady pressure coefficient is defined by

$$\tilde{c}_p = \frac{\tilde{P}}{\overline{P}_{exit} A_m} \tag{5-3}$$

This case is also calculated by the nonlinear time-marching method, and the periodic unsteady results are Fourier transformed and the first harmonic complex amplitudes of the unsteady pressure coefficients are given in Fig. 5-2. It can be seen the comparison between these three numerical methods is very good, the shock impulses predicted by the linear and the nonlinear harmonic methods are slightly higher than that predicted by the nonlinear time-marching method.

The amplitude of the back pressure fluctuation is then increased to 7% and the shock wave is oscillating at a much larger amplitude in the channel. First, this unsteady flow is calculated by the nonlinear time-marching method, the unsteady pressure is time-averaged and its distribution on the channel wall is given in Fig.5-3. It can be seen that the time-averaged flow field around the shock position is very different from the steady flow, and the time-averaged shock is much smeared due to the large amplitude of shock oscillation. The significant difference between the time-averaged flow and the steady flow suggests the important nonlinear effects. This is confirmed by checking the first and second harmonics of the unsteady pressure produced by the nonlinear time-marching analysis as shown in Fig.5-4, it can be seen that the second harmonic quantities are not small compared to the first harmonic quantities.

This unsteady flow is then calculated by the nonlinear harmonic method. The time-averaged pressure distribution is presented in Fig.5-3. The comparison with the nonlinear time-marching method shows the excellent agreement and the smeared time-averaged shock is very well predicted. It demonstrates that the nonlinear effects are well captured by the nonlinear harmonic analysis. The unsteady pressure amplitudes by the nonlinear harmonic method are given in Fig.5-5 and compared to the results produced by the time-linearized method and the nonlinear time-marching method. Because the unsteady perturbation in the linear method is based on the steady flow field, the predicted unsteady shock impulse by the linear analysis is much

higher and narrower than that predicted by the nonlinear time-marching method. The comparison between the nonlinear harmonic method and the nonlinear time-marching method is considerably improved. It should be noted that the shock wave in the nonlinear harmonic method is mainly smeared by the unsteadiness due to the shock oscillation. But in the time-linearized Euler/Navier-Stokes methods, the shock waves are only smeared by the artificial smoothing (Linquist and Giles, 1990).

The calculations of this transonic channel unsteady flows have shown that the time-linearized method can correctly predict the unsteady shock impulse if the nonlinear effects are very small. The nonlinear harmonic method can considerably improve the results over a linear analysis when the nonlinearity is important.

5.3 Oscillating Biconvex Cascade

In order to check the effectiveness of the nonlinear harmonic Euler method for unsteady flows in turbomachinery, the unsteady flows around an oscillating biconvex cascade are calculated. This case was initially investigated by a nonlinear time-marching Euler method (He, 1990b) and a strong nonlinear effect due to a remarkable shock oscillation under a high pressure ratio was demonstrated in the nonlinear analysis. This case is a good test to the present nonlinear harmonic Euler method. Although this is an inviscid case, calculations of unsteady transonic flows using the Euler equations are particularly useful because they can be used to address the issue of nonlinearity associated with shock oscillation without being confused with the viscous effects.

In this test case, the geometry of the biconvex cascade is given by

Blade chord:	C = 0.1524m
Stagger angle:	$\gamma = 0^0$
Relative thickness:	0.076 (maximum thickness/chord)

Solidity: 1.3

The flow condition is given by

Inlet total pressure:	$P_0 = 100000$pa
Inlet total temperature:	$T_0 = 288$K
Inlet flow angle:	$\beta = 0^0$

In the calculations, two back pressure conditions are specified to set up distinctively different steady shock positions, one is $P_{exit} / P_0 = 0.7$, another is $P_{exit} / P_0 = 0.725$. For a lower pressure ratio, a fairly strong shock is situated near the exit of the cascade passage, while for the higher pressure ratio, there is a weak shock just downstream of the cascade throat. The unsteady flows are introduced by the blade oscillation in a torsion mode around its leading edge. The reduced frequency which is based on the blade chord is 1.3 in the present investigation. The unsteady flows under different torsion amplitudes are investigated in the calculations.

First, the lower pressure ratio case is investigated. A steady flow solution is obtained by solving the steady flow equations. The steady Mach number contour map is given in Fig. 5-6 and the steady isentropic Mach number distribution is presented in Fig. 5-7. The steady solution confirms that a fairly strong shock with an upstream Mach number of 1.3 is situated in the blade passage at about 85% of blade chord. For the unsteady flow, the amplitude of blade torsion is given to be 2 degrees. The unsteady calculations are carried out by the time-linearized Euler method, nonlinear time-marching method (He, 1990b), and the nonlinear harmonic Euler method. In this lower pressure ratio case, even though the blade torsion amplitude is very big, the shock oscillation is confined in a relatively small region, as indicated by the unsteady pressure impulses shown in Fig. 5-8. The calculated amplitudes and phase angles of the unsteady pressures on blade surface produced by these three methods agree very

well. The time-averaged Mach number distributions by the nonlinear time-marching and nonlinear harmonic methods are very close to the steady solution as shown in Fig.5-7. The computational results for this fairly strong shock case suggest a very weak nonlinear effect. Therefore, the conventional time-linearized method should be sufficiently adequate for this case.

The pressure ratio is then increased to 0.725 to push the shock forward. The steady Mach contour map is shown in Fig. 5-9. It can be seen that a steady weak shock with upstream Mach number of about 1.15 is located at around 65% of the blade chord, just downstream of the cascade throat. This can also be seen from the steady isentropic Mach number distribution on blade surface as presented in Fig. 5-10. In this calculation, a quite small artificial smoothing coefficient is used to give a sharper steady shock, the small oscillation of the steady isentropic Mach number distribution before the shock, as shown in Fig. 5-10, is due to the small artificial smoothing. For the unsteady calculations, the blade torsion amplitude is specified to be 0.75 degree. Again, the unsteady calculations are carried out by above three numerical methods. The time-averaged Mach number distribution by the nonlinear time-marching method is shown in Fig. 5-10. Under this pressure ratio, the time-averaged flow around the shock is very different to the steady one. The shock oscillates in a much wider range around its mean position when the blades are oscillated. This smeared time-averaged pressure jump due to the shock oscillation is very well predicted by the nonlinear harmonic method as shown in Fig.5-10. In this case, the unsteady shock impulse predicted by the time-linearized Euler method is much higher and narrower than that predicted by the nonlinear time-marching method. The comparison between the nonlinear time-marching method and the nonlinear harmonic method is excellent. These comparisons demonstrate the effectiveness of the novel nonlinear harmonic approach, since the nonlinear time-marching solutions are normally much more time consuming than the frequency domain harmonic solutions. In the calculations, it is found that the computational time

for a nonlinear harmonic analysis is typically 60% more than that for a conventional time-linearized analysis.

At the same pressure ratio of 0.725, further numerical investigations are carried out at a blade torsion amplitude of 2 degrees. From the nonlinear time-marching calculations, it is found that the unsteady shock behaves very differently from that in the case with the torsion amplitude of 0.75 degree. In this case, when the blade oscillates, the shock moves to the throat and does not decay into a compression wave as expected in a quasi-steady sense. The unsteady inertia makes the shock move into the subsonic region. Once entering the subsonic region, the shock has to propagate upstream and eventually disappears around the blade leading edge. Then the new shock appears again around the throat. The dramatic shock movement can be clearly seen from a space-time contour of relative static pressure which was produced by the nonlinear time-marching method (He, 1990b). It can also be clearly seen from a flow animation which was made by the author on a HP workstation. This remarkable shock movement produces very strong nonlinear effects. As a result, the time-averaged Mach number distribution generated by the nonlinear time-marching method is very different from the steady one even in the subsonic region, as shown in Fig.5-12. Due to the strong nonlinearity, the predicted unsteady pressure by the time-linearized method is distinctively different to that predicted by the nonlinear time-marching method, as given in Fig. 5-13. Although a considerable improvement can be seen from the results by the nonlinear harmonic analysis, there is a marked discrepancy from the nonlinear time-marching analysis. This indicates the limit of the applicability of the present nonlinear harmonic method in the extreme nonlinear circumstances. The limitation arises likely due to the quasi-linear form of the first harmonic perturbation equations. Furthermore, in the nonlinear harmonic method, only those nonlinear terms due to the production of the harmonics (such as $\overline{(\rho u)'v'}$) are included, physically they are just part of the nonlinearity.

The calculations of unsteady flows around the oscillating biconvex cascade suggest whether the shock oscillation in turbomachinery can be modelled by the linear method does not much depend on the strength of the shock, while the location of the shock seems to be crucial. This finding in this study is consistent to what is observed in a nonlinear time-marching analysis (He,1990b).

5.4 Unsteady Turbulent Flow in Transonic Diffuser

To check the validity of the present nonlinear harmonic Navier-Stokes method for predicting the unsteady turbulent flows, the unsteady turbulent flows in a transonic diffuser are numerically investigated by the nonlinear harmonic Navier-Stokes method. This diffuser unsteady flow was experimentally studied at McDonnell-Douglas and a wide range of time-mean and unsteady experimental data are available (Bogar et al, 1983, Salmon et al, 1983, Sajben et al, 1984). The experimental studies included both self-induced and forced oscillations of the diffuser flow field. Because of the limited experimental data available for unsteady turbulent flows in turbomachinery, this test case has been widely used for the validation of numerical methods (Hseih et al, 1984, Allmaras, 1989, He and Denton, 1993).

The diffuser model is a convergent/divergent channel with a flat bottom and a contoured top wall. The definition of the top wall profile can be found in a reference by Bogar et al (1983). In the diffuser, the subsonic flow accelerates in the convergent part to supersonic, then the supersonic flow is terminated by a normal shock wave locating just downstream of the diffuser throat. In the experiment, several diffuser configurations with different exit-to-throat area ratios were investigated. The shock and boundary layer interaction may or may not induce the flow to separate on the top wall, depending on the diffuser configuration and the Mach number immediately before the normal shock ($M_{\sigma u}$). In the present study, the diffuser configuration is such that it has a throat height, h^*, of 44.0 mm , and exit-to throat area ratio of 1.52

as depicted in Fig.5-14. For this configuration, if $M_{\sigma u}$ is less than 1.28, the turbulent boundary layers on both the top and bottom walls are attached, while if $M_{\sigma u}$ is above than 1.28, the shock/boundary layer interaction induces the boundary layer on the top wall to separate and the boundary layers on both walls merge together near the end of the diffuser, as depicted in Fig. 5-15.

In the present numerical investigation, a weak shock case is considered and the flow condition is given so that the $M_{\sigma u}$ is 1.235. To match this flow condition, a pressure ratio (P_{exit} / P_0, exit static pressure to inlet total pressure) of 0.826 is prescribed and the flow is assumed to be fully turbulent at the diffuser inlet on both bottom and top walls. In the previous numerical studies (Hsieh et al, 1984, Allmaras, 1989, He and Denton, 1993), a flat plate turbulent profile in the inlet upper and lower wall boundary layers was specified and the boundary layer thicknesses were given. In the present calculations, no inlet boundary layer thickness is specified. The mesh used in the calculations is 122×45 as shown in Fig.5-16. In all the present viscous steady and unsteady calculations, the slip-wall boundary condition is specified.

The steady flow at this flow condition is calculated by the present steady solver. A predicted steady Mach number contour map is shown in Fig.5-17 and a normal shock can be clearly seen. The boundary layer on both top and bottom walls are attached and they do not merge together at the exit of the diffuser. The predicted steady static pressure distribution on the top wall by the present steady flow solver is presented in Fig. 5-18 and compares well with the experimental data. It can be seen that the shock situates at x / h^* of about 1.4, where x is the axial distance from the location of the diffuser throat. Meanwhile, an inviscid flow result by the Euler solver is also presented in Fig. 5-18, the shock wave predicted by the inviscid calculation is located much behind that predicted by the viscous calculations. Apparently, the viscous effects are very important to predict this experimental case correctly. The predicted boundary layer displacement and momentum thickness distributions

compare reasonably well with the experimental measurements on both the top and bottom walls as shown in Fig. 5-19.

In the experiment, two kinds of unsteady flows were investigated: one is a natural unsteadiness identified as longitudinal acoustic modes induced by the interactions of the shock and diffuser exit, the other was forced unsteady flows produced by rotating a triangular, prism-shaped rotor partially embedded in the bottom wall and driven by a variable-speed motor. The mechanism of the natural unsteadiness in this experiment is rather complex. It should be mentioned that no self-excited unsteady flows have been observed in the present numerical calculations. A work by Allmaras (1989) suggested that a very fine mesh near both the top and bottom wall boundaries has to be used to resolve the self-excited unsteadiness. The interest of the current work in this diffuser case is only on the forced unsteady flows.

To model the forced unsteady flows, the unsteady flow in calculations is introduced by prescribing a static pressure oscillation at the diffuser exit in a harmonic form as

$$P_{exit} = \overline{P}_{exit}(1 + A_m \sin 2\pi ft) \qquad (5\text{-}4)$$

In the experimental studies, the unsteady pressures were measured by Sajben et al (1984) under two forced unsteady frequencies, 300 Hz, 150 Hz. According to the experimental measurements, the amplitudes of the back pressure oscillation under these two frequencies are 0.0085, 0.011, respectively. Unfortunately the unsteady pressure measurements were only carried out downstream of the shock wave, the experimental data in the shock wave oscillating region is not available where unsteady flow is most active and important. In order to assess the time-linearized and nonlinear harmonic methods, the unsteady flows are also calculated by a nonlinear time-marching method (He, 1994b) and the time-linearized Navier-Stokes method.

For the unsteady flow with a frequency of 300 Hz and the back pressure oscillating amplitude of 0.0085, the predicted amplitude and phase distributions of the unsteady pressure on the top wall by these three numerical methods are shown in Fig. 5-20. In this case, the shock wave just slightly oscillates around its time-mean position, the nonlinear effect due to the shock oscillation is very small. The numerical results produced by these three methods compare quite well and they are in a good agreement with the experimental data.

For the case with a frequency of 150 Hz and the back pressure fluctuation amplitude of 0.011, both the experiment and a nonlinear time-marching analysis confirm that the shock wave oscillates in a much bigger region compared to the 300 Hz case. The time-averaged pressure distribution on the top wall produced by the nonlinear time-marching method is quite different to the steady distribution around the shock wave oscillating region, as shown in Fig. 5-21. The time-averaged shock is much smeared by the unsteadiness due to the shock oscillation. This smeared time-averaged shock wave is very well predicted by the nonlinear harmonic Navier-Stokes method. The predicted amplitude and phase of the unsteady pressure on top wall of the diffuser by the time-linearized, nonlinear harmonic and nonlinear time-marching methods are presented in Fig.5-22 and they are also compared to the experimental data. In this case, the linear method overpredicts the peak amplitude of the unsteady shock impulse by a factor of more than 2 compared to the nonlinear time-marching analysis. The comparison between the present nonlinear harmonic method and the nonlinear time-marching method is excellent. Although all the numerical results compare well to the experimental data, the experimental data are only available downstream of the shock wave and do not reveal the important nonlinear behaviour of the shock oscillation.

For the numerical method in turbomachinery, the mesh-dependence is one of the major concerns. To investigate the mesh-dependence of the present nonlinear harmonic method, a much finer mesh with a size of 245×45 is generated as shown in

Fig. 5-23. It can be seen that the mesh points in axial direction around the diffuser throat is roughly tripled. The case with the frequency of 150 Hz and the back pressure fluctuation amplitude of 0.011 is calculated again by the nonlinear harmonic Navier-Stokes method. The time-averaged static pressure distribution on the top wall of the diffuser is compared to the one obtained with previous coarser mesh, as shown in Fig. 5-24. The difference between them is very small and acceptable. The comparison of the unsteady pressure distributions generated from the coarse and fine meshes are good, as presented in Fig. 5-25. This calculation has suggested that the mesh-dependence of the present nonlinear harmonic method is small.

5.5 Oscillating Transonic Compressor Cascade

The final validation for the nonlinear harmonic Navier-Stokes method is made by calculating unsteady flows around an oscillating transonic compressor cascade. The blade has a biconvex profile and the geometry of the cascade is given by

Chord (C):	0.0762m
Maximum Relative Thickness:	2% C
Stagger Angle:	59^0
Solidity (C/Pitch):	1.11

And the flow condition is

Inlet Mach number:	1.25
Reynolds number:	1.5×10^6
Incidence:	3^0
Back pressure ratio(P_{exit} / P_0):	0.5926

The flow in the cascade is assumed to be fully turbulent from the leading edge. The unsteady flow in this case is induced by the blades oscillation in a torsion mode around the mid-chord with an amplitude of 1 degree and a reduced frequency of 0.5 (based on the blade chord and inlet flow velocity), and an inter-blade phase angle of 180 degrees. In the numerical studies, the unsteady flows are calculated by the present nonlinear harmonic Navier-Stokes method, again the results are compared to those by the time-linearized Navier-Stokes method, and the nonlinear time-marching method (He, 1994b). The mesh used in the calculations is 115×27, and the slip-wall condition is imposed in all the steady and unsteady calculations.

First the steady flow in this transonic cascade is investigated by using the steady Navier-Stokes solver. Fig. 5-26 gives the steady static pressure distributions on the blade surfaces. Fig. 5-27 shows the steady Mach number contours. It can be seen that the cascade is subject to a strong passage shock wave near the leading edge, typical of a modern transonic fan at a near peak efficiency condition. The amplitude and phase angle distributions of the unsteady pressure coefficients on blade surfaces predicted by three numerical methods are shown in Fig. 5-28. Again the amplitude of the unsteady shock impulse captured by the linear method is much higher than that produced by the nonlinear time-marching method, while the present nonlinear harmonic and the nonlinear time-marching analyses are in a good agreement. It should be emphasised that for blades oscillating in a torsion mode, a detailed (rather than integral) unsteady loading distribution is important for calculations of blade flutter characteristics.

Finally, some comments should be made with regard to the computing time. In this cascade case, a nonlinear harmonic solution requires about 1.5 hours CPU time on a single SGI R10000 processor, which is about 60% more than that required by a pure linear solution. This CPU time consumed by the nonlinear harmonic solution is comparable to that by a nonlinear time-marching solution for a single blade passage. However, a single passage domain can always be adopted for the nonlinear harmonic

method, whilst a multiple-passage domain has to be adopted by conventional nonlinear time-marching methods. A numerical test has shown that for an annulus with 20 blade passages, the present nonlinear harmonic solution with one harmonic disturbance is about 20 times faster that a 20 blade passage nonlinear time-marching solution. It should be mentioned that no acceleration technique is applied in this test case. A further speed-up of the nonlinear harmonic solution by a factor of 5 or more would be expected if a multi-grid technique is used.

5.6 Summary

In this chapter, the numerical results by the novel nonlinear harmonic Navier-Stokes/Euler method have been presented. The validity of this method has been demonstrated by comparing its numerical results to those produced by the nonlinear time-marching method, time-linearized method, and experimental data. Although the primary aim of the work is to validate the novel nonlinear harmonic method, the time-linearized method presented in Chapter 2 is further checked and its limitation subject to nonlinear effects has been clearly demonstrated. The nonlinear harmonic method can considerably improve results over the linear analysis when the nonlinearity is important, due to its capability of capturing the nonlinear effects by the coupling between the time-averaged flow and the unsteady perturbations. The numerical tests have shown that computational time required for a nonlinear harmonic analysis is typically 60% more than that for a conventional linear analysis. Therefore the nonlinear harmonic method is still much more efficient than the nonlinear time-marching method. However, the limitation of the nonlinear harmonic analysis has also been observed in the calculations of the unsteady flows in a biconvex cascade. The limitation is probably due to the quasi-linear form of the first harmonic perturbation equations.

Chapter 6 Numerical Investigations of Trailing Edge Vortex Shedding

6.1 Introduction

In the last several chapters, the development and validation of a time-linearized Navier-Stokes/Euler method and a nonlinear harmonic Navier-Stokes/Euler method have been presented. For both methods, a time-independent (steady or time-averaged) flow field is required to be the base for a linear or a nonlinear harmonic analysis. However, the time-independent solution cannot be achieved once any self-excited aerodynamic instabilities occur. Trailing edge vortex shedding is one of the self-excited aerodynamic instabilities in turbomachinery occurring when viscous flows pass a blade with a blunt trailing edge. Producing a time-independent solution is problematic if the trailing edge vortex shedding is resolved in the calculation. Although the time-averaged flow field of a vortex shedding case could be produced by solving unsteady Navier-Stokes equations, the calculation is too expensive because the vortex shedding has a very small length and time scale. Therefore, a natural question is: can we produce a time-independent solution which can include time-averaged effects of trailing edge vortex shedding without carrying out an unsteady calculation? Solving the time-averaged equation is probably one of the answers. The difficulty in doing so is that extra closure models are required to model the unsteady stress terms in the time-averaged equations, just as turbulence models are needed to solve the Reynolds averaged Navier-Stokes equations. The modelling issues associated with unsteady flows induced by the bladerow interaction and the blade flutter have been addressed by some other researchers (Adamczyk, 1985, Giles, 1992, He, 1996a). The modelling of trailing edge vortex shedding has not been investigated so far. In this chapter, some efforts towards the modelling of vortex shedding will be presented. **The main issue to be addressed in this work is: can we achieve a time-**

independent solution for trailing edge vortex shedding by solving time-averaged Navier-Stokes equations?

Although this part of the work originally arises from the consideration of a linear and nonlinear harmonic analysis for the blade flutter, it actually concerns a general issue in turbomachinery. As introduced in Chapter 1, understanding and predicting the trailing edge vortex shedding is of great importance in turbomachinery for further improvement of machine performance. Unfortunately, in the current turbomachine design systems, trailing edge vortex shedding is usually missed for some unavoidable reasons, such as the computational meshes are too coarse, numerical schemes are too dissiaptive, or time steps are too big etc. However, as far as a turbomachine designer is concerned, it is highly desirable to take account of the time-averaged effects of trailing edge vortex shedding in a design procedure. An efficient way to do so is to solve the time-averaged equation. But the modelling issues have to be addressed before solving the time-averaged equations. Recently there has been increasing interest in modelling rather than calculating unsteady flows for turbomachine design (Chen, Celestina and Adamczyk, 1994, Hall, 1997).

Similar to the nonlinear harmonic approach as descried in the first part of this thesis, in this work the unsteady flow induced by vortex shedding is decomposed into a time-averaged flow plus an unsteady perturbation. The time-averaged equations can be produced by time-averaging the unsteady Navier-Stokes equations, consequently extra unsteady stress terms are generated in the time-averaged equations. Here the unsteady stresses are produced due to trailing edge vortex shedding. Whether or not these unsteady stresses can suppress vortex shedding is the key question. The present work starts with unsteady calculations of trailing edge vortex shedding by using an unsteady Navier-Stokes solver. The time-averaged flow fields are produced by time-averaging unsteady results, and the unsteady stress terms induced by trailing edge vortex shedding are obtained. Then the time-averaged equations with known unsteady

stresses are solved. The effectiveness of the unsteady stresses to suppress trailing edge vortex shedding will be checked from the solution of time-averaged equations.

In this work, the investigations start with vortex shedding from a circular cylinder. Then a case with realistic turbine blading (VKI turbine blades) is extensively examined.

6.2 Multi-Block Unsteady Navier-Stokes Solver

In the present study, the baseline numerical solver is a multi-block unsteady Navier-Stokes solver originally developed by He (1996b) for flows past a set of cylinders. This code is used for the unsteady calculation of trailing edge vortex shedding in this work. In the code, the flow governing equation is a 2-D unsteady Reynolds averaged Navier-Stokes equation.

The original code can only handle laminar flows. In the present work, a turbulence model is implemented for handling turbulent flows. For vortex shedding prediction, it is arguable which turbulence model can or cannot be used. In this work, a mixing-length turbulence model in its simplest form is implemented for turbulent flows. In this model, the turbulent viscosity is given by

$$\mu_t = \rho l_{mix}^2 |\omega| \tag{6-1}$$

where $|\omega|$ is the magnitude of the vorticity given by

$$|\omega| = \left| \frac{\partial u}{\partial y} - \frac{\partial v}{\partial x} \right|$$

In the near wall region, the mixing length is given by

$$l_{mix} = \kappa \min(d_n, d_{lim}) \tag{6-2}$$

where κ is the Von Karman constant and is 0.41; d_n is the distance to the wall and d_{lim} is a limiting value input by the user. In the wake, the mixing length is taken as κd_{lim}. It is recognised that vortex shedding unsteady calculations are sensitive to turbulence models (Manna and Mulas, 1994, Arnone and Pacciani, 1997). In this work, the sensitivity issue will be investigated by simply specifying different d_{lim} values in calculations.

In order to give a better resolution for the vortex shedding, the solver uses a multi-block mesh. In a calculation, the unsteady Navier-Stokes equation is simultaneously integrated on each block by using the 4-stage Runge-Kutta time-marching scheme. At the end of each fractional time-step, the communication between different blocks is carried out by averaging conservative flow variables $(\rho, \rho u, \rho v, \rho e)$ at connecting points of different blocks. For example, the point (i,j) is a connecting point between the block I and II, the updated value of the density at the end of each fractional time-step at point (i,j) can be given by

$$\rho_{ij}^{new} = 0.5(\rho_{ij}^{I} + \rho_{ij}^{II}) \tag{6-3}$$

where ρ_{ij}^{I} is obtained from the calculation on block I, and ρ_{ij}^{II} is obtained from the calculation on block II at the end of each fractional time step. The unsteady Navier-Stokes equation is again spatially discretized by a cell-vertex scheme. The details of the numerical schemes can be found in Chapter 2.

6.3 Time-Averaged Navier-Stokes Equation and Solution Method

The unsteady flow induced by the trailing edge vortex shedding is assumed to be a time-averaged flow plus a periodic unsteady perturbation, i.e.

$$U = \overline{U} + U' \tag{6-4}$$

Substituting this expression into the unsteady Navier-Stokes equation and time-averaging it over a vortex shedding period, the time-averaged equation can be obtained. The form of the time-averaged equation is the same as Eq.(4-6), except in this study it is in a 2-D form. The unsteady stress terms in the time-averaged equation are produced by the trailing edge vortex shedding. It should be mentioned that in the time-averaged equation, the unsteady stresses contributed by the random unsteadiness (turbulence) are modelled by the turbulence model. The random fluctuation and periodic vortex shedding perturbation are assumed to be uncorrelated in a global-mean sense (Reynolds and Hussain, 1972, Cantwell and Coles, 1983).

The key to solving the time-averaged equation is to know the unsteady stress terms produced by the vortex shedding. The major objective of the present study is to investigate the feasibility of achieving a time-independent solution by solving the time-averaged equations. The unsteady stress terms in the time-averaged equation are obtained from unsteady solutions. For instance, the unsteady stress $\overline{(\rho u)'v'}$ can be worked out from

$$\overline{(\rho u)'v'} = \frac{1}{N_p}\sum_{1}^{N_p}[\rho u - \overline{\rho u}][v - \overline{v}] \tag{6-5}$$

where the time-averaged variables $\overline{\rho u}$ and $\overline{v}$ can be obtained by

$$\overline{\rho u} = \frac{1}{N_p}\sum_{1}^{N_p}\rho u \qquad \overline{v} = \frac{1}{N_p}\sum_{1}^{N_p} v$$

where ρu and v are instantaneous variables obtained from unsteady calculations; N_p is the number of time steps in one vortex shedding period, it can be determined from the vortex shedding frequency f and the size of time-step Δt in an unsteady calculation by

$$N_p = \frac{1}{f\Delta t} \tag{6-6}$$

The vortex shedding frequency f can be obtained by analysing the unsteady flow results using a Fourier transformation.

6.4 Unsteady Calculation of Trailing Edge Vortex Shedding

The first step of the present work is to calculate the trailing edge vortex shedding by solving the unsteady Navier-Stokes equation. The calculations are conducted for flows past a circular cylinder and a VKI turbine cascade. The time-averaged flow fields and unsteady stress terms are calculated from the unsteady solutions.

6.4.1 Laminar Vortex Shedding behind a Circular Cylinder

In this calculation, the cylinder has a diameter (D) of 0.2m. The flow has a free stream Mach number of 0.27 and Reynolds number (based on the cylinder diameter and free stream velocity) of 3,000. In this case the flow is assumed to be fully laminar. The present calculation is carried out in a domain which is made up by two cylinders. In order to avoid the interference of the vortex shedding from the two cylinders, the pitch of the computational domain is set to be 6.5D. The mesh in this calculation has 4 blocks, the layout of the blocks is shown in Fig.6-1. The mesh in the first block is an O-type mesh with 101×21 points, and the mesh in other three blocks is a simple H-type mesh, as shown in Fig.6-2. The mesh has a total of 13,549 points.

In order to accelerate convergence of the unsteady calculation, a time-consistent two-grid technique (He, 1993a) is applied in the first block.

Fig.6-3 shows an instantaneous static pressure history at point C on the cylinder which corresponds to an angle of -45^0. It can be seen that the unsteady Navier-Stokes equation needs to be time-marched about 25 shedding cycles to achieve a periodic trailing edge vortex shedding. In this calculation, there are about 850 time steps in one vortex shedding period. For one shedding period, it takes about 415 seconds CPU time on a single SGI R10000 processor. Once periodic vortex shedding is achieved, the instantaneous static pressure history at point C is analyzed by a Fourier transformation and the pressure spectrum is given in Fig.6-4, it can be seen that the predicted vortex shedding frequency is 90 Hz. This shedding frequency is equivalent to a Strouhal number of 0.192. For the vortex shedding behind the circular cylinder, the Strouhal numbers can be calculated by an empirical formula (Massey, 1983) as

$$\mathrm{St} = 0.198(1 - 19.7 / \mathrm{Re}) \qquad (6\text{-}7)$$

for $250 < \mathrm{Re} < 2 \times 10^5$. In this investigation, the empirical value of Strouhal number is 0.197. The predicted Strouhal number (0.192) by the present unsteady calculation is very close to the empirical value. The contours of instantaneous static pressure, Mach number and entropy are presented in Fig.6-5 ~ Fig.6-7. It can be seen that the structure of the Von Karman vortex street behind the circular cylinder has been very well captured by the present unsteady calculation.

Once periodic vortex shedding is achieved, the unsteady solution is time-averaged over several shedding periods to produce a time-averaged flow field. The time-averaged static pressure and entropy contours are shown in Fig.6-8 and Fig.6-9, they are symmetric along the wake centreline. It can be seen that vortex shedding is averaged out in the time-averaged flow field. Fig.6-10 presents a time-averaged static

pressure distribution along the cylinder surface and the wake centreline. The static pressure in the region of separated flow just downstream of the cylinder (the base region) is lower than that in the freestream. This produces a component of the total loss known as the base loss.

As introduced in the last section, to solve the time-averaged equations, it is necessary to know the unsteady stresses. In this work, the unsteady stress terms are calculated from the present unsteady solutions. The contours of three primary unsteady stresses ($\overline{(\rho u)'u'}$, $\overline{(\rho v)'v'}$, $\overline{(\rho u)'v'}$) are presented in Fig.6-11 to Fig.6-13, all the stresses are non-dimensionized by the inlet dynamic head ($0.5\rho_{inl}u_{inl}^2$). As shown in Fig.6-11, the streamwise normal stress $\overline{(\rho u)'u'}$ is symmetric along the wake centre and exhibits double peaks near the end of the vortex formation region, the stress then decays rapidly along the wake direction. The stress $\overline{(\rho u)'u'}$ mainly remains bimodal throughout the near wake and makes very little contribution on the wake centreline. The structure of the stress $\overline{(\rho u)'v'}$ is quite similar to the $\overline{(\rho u)'u'}$, but it is anti-symmetric along the wake centre and the two peaks are closer to the wake centreline, as shown in Fig.6-12. For the pitchwise normal stress $\overline{(\rho v)'v'}$, as shown in Fig.6-13, only a single peak exists on the wake centreline approximately at the end of the vortex formation region.

Generally speaking, the structures of these three unsteady stresses are not very complex. All of the unsteady stresses reach their peak values near the end of the vortex formation region, at about $x/D \approx 1.0 \sim 1.5$ (x=0 corresponds to the centre of the cylinder), then decay rapidly with increasing values of x along the downstream of the wake. The topologies of these three unsteady stresses predicted by the present unsteady calculation are very similar to those produced by an experiment (Cantwell and Coles, 1983). In Cantwell and Coles' work, the unsteady flows around a circular cylinder induced by random turbulence and periodic vortex shedding at $Re = 1.4 \times 10^5$ were extensively measured.

6.4.2 Vortex Shedding from a VKI Turbine Cascade

To investigate the trailing edge vortex shedding from turbomachine blades, the unsteady flow in a VKI turbine cascade is calculated. This cascade consists of 3 low cambered two-dimensional turbine nozzle blades. The blade in the middle has a thick rounded trailing edge to accommodate a pressure transducer for the measurement of the base pressure. Some blade geometry characteristics are

Chord:	279.99 [mm]
Stagger angle:	-49.833 [deg.]
Blade height:	200 [mm]
Pitch:	195 [mm]
Trailing edge thickness:	15 [mm]

The trailing edge vortex shedding from this turbine blade has recently been experimentally studied at VKI (Cicatelli, Siverding and Fevrier, 1994, Cicatelli and Siverding,1996). This test case has been numerically investigated by some researchers (Manna and Mulas, 1994, Arnone and Pacciani, 1997). The flow conditions in the test were

Inlet total pressure:	17462 Pa
Inlet total temperature:	293 K
Reynolds number:	2.5×10^6
Outlet isentropic Mach number:	0.409

To calculate this test case, the mesh is required to be carefully generated. There are several important aspects to the mesh generation for the vortex shedding unsteady calculations in turbomachinery. Firstly, a fine mesh is needed near the blade surface and in the wake to resolve the boundary layer and the small length scale

vortex shedding. Secondly, the mesh needs to minimise as much as possible skewness and distortion to give a good resolution of the unsteady flows. Finally, care also must be taken to ensure the high degree of uniformity of the mesh near the blade surface and in the wake. According to these requirements, a 4-block mesh is generated for this VKI turbine cascade. In the first block, an O-type mesh is generated with a mesh size of 271×35, there are about 45 mesh points around the trailing edge semi-circle. A preliminary calculation shows that there are about 15 points in the boundary layer near the trailing edge and the value of y^+ is about 25 under the test flow conditions. In the other three blocks, a simple H-type mesh is generated. The 4-block mesh has a total of 41879 points. The layout of blocks of the mesh is shown in Fig.6-14. The mesh is presented in Fig.6-15 and an enlarged view of the mesh near the blade trailing edge is shown in Fig.6-16.

Once the mesh is generated, the unsteady flow induced by trailing edge vortex shedding is calculated by solving the unsteady Navier-Stokes equations. But before we carry out the calculation under the test flow conditions, a low Reynolds number laminar vortex shedding from this VKI turbine cascade is calculated. The main purpose of doing this is to create a case without any turbulence effects in order to avoid any uncertainties due to turbulence models. In this calculation, the Reynolds number is specified to be 2.5×10^4 which is two orders of magnitude lower than the test value, the flow is assumed to be fully laminar. After the unsteady Navier-Stokes equation is time-marched for about 50 shedding periods, periodic vortex shedding is achieved. Each shedding period needs about 1,250 time steps and takes about 2,280 seconds CPU time running on a single SGI R10000 processor. The predicted vortex shedding Strouhal number (based on the trailing edge thickness and downstream flow velocity) is 0.235. The instantaneous static pressure and entropy contours in Fig.6-17 and Fig.6-18 have shown that a rigorous vortex shedding street behind the blade trailing edge is captured.

Then this VKI turbine cascade flow under the test flow conditions is calculated. In the calculation, the flow is assumed to be fully turbulent from the leading edge of the blade. The turbulence mixing length limit d_{lim} in the turbulence model is given to be 2% of the trailing edge thickness. In the calculation, the non-slip wall boundary condition is applied on the blade surface. Numerical tests show that the unsteady Navier-Stokes equation must be time-marched through at least 60 vortex shedding periods to achieve a good level of periodicity of the vortex shedding from an initial 1-D flow guess. There are about 1,200 time steps in one shedding period. For each shedding period, it takes about 2,100 seconds CPU time running on a single SGI R10000 processor. It can be seen that the computation time for an unsteady calculation of vortex shedding in turbomachinery is very long, even using a moderately fine mesh and a very simple turbulence model.

Fig.6-19 shows the static pressure time traces at points corresponding to abscissa S/D of 0.65 and -0.65 on the blade trailing edge, the positions of these two reference points can be found in Fig. 6-20. At the same abscissa, the calculation suggests that the pressure fluctuation on the pressure surface is higher than that on the suction surface, which is consistent with experimental observation (Ciatelli and Sieverding, 1996). The different vortex shedding intensity on the suction and pressure surfaces in cascade flows has also been observed by other researchers (Han and Cox,1982). A vortex shedding frequency spectrum by the present calculation is shown in Fig.6-21 which suggests the predicted vortex shedding Strouhal number is 0.245, slightly lower than the experimental value of 0.27. The instantaneous contours of static pressure, Mach number and entropy in Fig.6-22 to Fig.6-24 have shown that a vigorous vortex shedding is obtained by the present unsteady calculations.

Having achieved periodic vortex shedding, the unsteady flow is then time-averaged over several shedding periods to give a time-averaged flow field. The time-averaged isentropic Mach number is compared with the experimental results in Fig.6-25. The comparison on the pressure surface is very good, but the static pressure on

the suction surface around the mid-chord region is overpredicted. The presented results are similar to those produced by an unsteady calculation using a standard Baldwin-Lomax model (Manna and Mulas, 1994). The base pressure around the blade trailing edge is reasonably predicted by the present calculation, as shown in Fig.6-26. The time-averaged pressure and Mach number contours are presented in Fig.6-27 and Fig.6-28. It can be seen that the vortex shedding is averaged out in the time-averaged flow field.

Based on the unsteady solution and the time-averaged flow field of this high Reynolds number turbulent case, the vortex shedding unsteady stresses are calculated. The contours of three major unsteady stresses ($\overline{(\rho u)'u'}$, $\overline{(\rho u)'v'}$, $\overline{(\rho v)'v'}$) are presented in Fig.6-29 to Fig.6-31. The structure of the unsteady stress $\overline{(\rho u)'u'}$ is very similar to the unsteady stress $\overline{(\rho v)'v'}$ in the circular cylinder case. The reason is that this VKI turbine blade has quite a high stagger angle, the direction of the velocity v in the wake is close to the streamwise direction. The stress $\overline{(\rho u)'u'}$ in this cascade flow case is more or less symmetric along the wake centre and a peak appears about one trailing edge thickness length downstream of the trailing edge, it then decays rapidly along the wake. Unlike its counterpart in the cylinder case, the stress $\overline{(\rho u)'v'}$ in the cascade flow is not anti-symmetric along the wake centre. The stress $\overline{(\rho v)'v'}$ is also not symmetric along the wake centre. One reason is that the direction of coordinate 'x' is not parallel to the wake direction in the turbine flow case, another reason is likely to be due to the different vortex shedding intensity from the blade suction and pressure sides. Nevertheless, the structure of unsteady stresses in the cascade flow is similar to those in the cylinder flow. The development of vortex shedding modelling in turbomachinery probably can benefit from a lot of studies on the vortex shedding behind circular cylinders.

In order to investigate the sensitivity of the vortex shedding unsteady calculation to the turbulence model, a calculation is carried out by specifying the value

of d_{lim} to be 10% of the blade trailing edge thickness. The higher value of d_{lim} means bigger viscosity in the boundary layer and wake, and the intensity of the vortex shedding is expected to be reduced. Numerical tests have shown that the vortex shedding disappears in this calculation and a 'steady-state' solution is obtained. Fig.6-32 and Fig.6-33 present the static pressure and Mach number contours, it can be seen that vortex shedding is suppressed due to the large value of d_{lim}. However, the calculated base pressure around the blade trailing edge is much higher than the experimental data as shown in Fig.6-42, due to the suppression of the vortex shedding. This calculation indicates that the unsteady vortex shedding calculation is sensitive to turbulence models.

6.5 Solutions by Solving Time-Averaged Equations

Periodic vortex shedding behind a circular cylinder and a VKI turbine blade have been achieved by solving the unsteady Navier-Stokes equations, as presented in the last section. The unsteady stresses induced by the vortex shedding are calculated from the unsteady solutions. In this section, the numerical solutions of the time-averaged equations will be presented. The unsteady stresses in the time-averaged equations are determined directly from the results produced by the unsteady calculations. In calculations for solving the time-averaged equation, the computational mesh, flow conditions, time step size, and artificial smoothing coefficients are all kept the same as their unsteady calculation counterparts (presented in Section 6.4), the only difference is that the unsteady stress terms are included.

6.5.1 Circular Cylinder

The first attempt is to solve the time-averaged equation for the circular cylinder case. The calculation residual history, as plotted in Fig.6-34, shows that a time-independent solution is achieved by solving the time-averaged equations. Here the residual is represented by the local maximum velocity residual in the first block.

The static pressure contour map is presented in Fig.6-35 and it suggests that the vortex shedding is completely suppressed by the unsteady stress terms. The comparison between the Fig.6-35 and Fig.6-8 shows excellent agreement. The calculated static pressure distribution along the cylinder surface and the centreline of the wake is in very good agreement with the time-averaged one produced by the unsteady calculation, as shown in Fig.6-10. The entropy contour map in Fig.6-36 again confirms that vortex shedding is suppressed. This numerical test has demonstrated that the vortex shedding can be suppressed by the unsteady stresses and a time-independent solution can be achieved by solving the time-averaged equation. Importantly this time-independent solution is very close to the time-averaged solution produced by the unsteady calculations.

It is well recognised that vortex shedding can be suppressed in different ways, such as excessive artificial smoothing, big time steps etc. In this work, a calculation is carried out by solving the original unsteady Navier-Stokes equation with an excessive artificial smoothing coefficient. In this calculation, the mesh and flow conditions remain the same as those in the unsteady calculation presented in Section 6.4.1, only the artificial smoothing coefficients are ten times larger. The residual history of this calculation is also shown in Fig. 6-34 and suggests that a steady-state solution is achieved. An entropy contour map in Fig.6-37 shows no sign of vortex shedding. However, the comparison between the steady static pressure distribution with the time-averaged one in Fig.6-10 shows that the large variation of the static pressure in the region just downstream of the cylinder is missing due to the suppression of the vortex shedding by using the excessive artificial smoothing.

6.5.2 VKI Turbine Cascade

The effectiveness of unsteady stresses to suppress the vortex shedding is then investigated on the VKI turbine cascade case. In this investigation, the first attempt is made on the low Reynolds number laminar flow case. Firstly, the vortex shedding

unsteady stresses are calculated from the unsteady solution in the laminar flow case as presented in Section 6.4.2. The contour maps of three unsteady stresses ($\overline{(\rho u)'u'}$, $\overline{(\rho u)'v'}$, $\overline{(\rho v)'v'}$) are presented in Fig.6-38 to Fig.6-40. The structure of these stresses shows a remarkable similarity to those in the turbulent case, only the peak values of the unsteady stresses in the laminar case are higher. This indicates that the random turbulence fluctuations and the periodic vortex shedding fluctuations are not correlated in a global-mean sense. The time-averaged equation is then solved with known unsteady stresses. The residual history in Fig.6-41 shows that a time-independent solution is achieved. The predicted static pressure distribution on the blade compares very well with the time-averaged one produced by the unsteady calculation, as shown in Fig.6-42. The static pressure and Mach number contour maps produced from this time-independent solution demonstrate that the vortex shedding is completely suppressed, as shown in Fig.6-43 and Fig.6-44.

Then a similar attempt is made for the high Reynolds number turbulent flow case. The time-averaged equation is time-marched with unsteady stresses produced from unsteady solutions in this turbulent flow case. The calculation again shows that vortex shedding is suppressed by unsteady stresses. A static pressure and Mach number contour maps are presented in Fig.6-45 and Fig.6-46, they are very similar to the time-averaged static pressure and Mach number contour maps as shown in Fig.6-27 and Fig.6-28. The comparison between the calculated static pressure by this calculation and the time-averaged static pressure produced by the unsteady calculation in Fig.6-25 is good. Importantly, the base pressure around the blade trailing edge is well predicted by solving the time-averaged equations, as shown in Fig.6-26.

In Section 6.4.2, a calculation with a d_{lim} of 10% of the trailing edge thickness has demonstrated that the vortex shedding unsteady calculation is highly sensitive to the turbulence model. It would be interesting to investigate the sensitivity

of the time-independent solution to the turbulence model. To this end, a calculation is carried out to solve the time-averaged equation with a d_{lim} being 10% of the trailing edge thickness. The unsteady stresses in this calculation are taken as those produced by the unsteady calculation with the value of d_{lim} of 2% of the trailing edge thickness. Again a time-independent solution is achieved in this calculation and the calculated static pressure around the trailing edge is plotted in Fig. 6-26. It can be seen that the base pressure by this calculation is closer to the experimental data than that produced by the unsteady calculation with the value of d_{lim} of 10% of the trailing edge thickness. It implies that solution of the time-averaged equations appears to be less sensitive to the turbulence model than the solutions by solving unsteady equations. This could be important and maybe of interest to turbomachine designers, because they would like to see that their design methods are less sensitive to turbulence models.

6.6 Summary

Some modelling issues on trailing edge vortex shedding have been addressed in this chapter. The emphasis of this work is to investigate the feasibility of producing a trailing edge vortex shedding time-independent solution by solving the time-averaged equations. To solve the time-averaged equations, it is essential to work out the unsteady stress terms. In this investigation, the unsteady stresses are calculated from vortex shedding unsteady calculations.

The work presented in this chapter starts with the unsteady calculation of vortex shedding behind a circular cylinder and a VKI turbine blade by using a multi-block Navier-Stoke solver. The numerical results have shown the structure and the frequency of vortex shedding street can be reasonably well predicted by the present unsteady solver. The calculations have demonstrated that the unsteady calculation of trailing edge vortex shedding in turbomachinery is very CPU time consuming. The

numerical tests have also demonstrated that vortex shedding unsteady calculation is highly sensitive to the artificial smoothing and turbulence model.

Based on the unsteady solutions, the time-averaged flow fields about trailing edge shedding are calculated. The vortex shedding unsteady stresses are worked out. The numerical results have shown that the structures of three major vortex shedding unsteady stresses ($\overline{(\rho u)'u'}$, $\overline{(\rho u)'v'}$, $\overline{(\rho v)'v'}$) are not very complex. All of them reach their peak values roughly at the end of the vortex shedding formation region, and then decay rapidly along the wake direction. The structures of the unsteady stresses in the turbine cascade flow are similar to those produced in the circular cylinder case, it suggests that the development of the vortex shedding modelling in turbomachinery probably can benefit from much easier studies of vortex shedding behind circular cylinders. The remarkable similarity of unsteady stress topologies between the laminar flow and the turbulent flow implies that the random turbulence fluctuations and the periodic vortex shedding fluctuations are uncorrelated in the global-mean sense.

With the vortex shedding unsteady stresses obtained from unsteady calculations, the time-averaged equations are solved. Numerical results have shown that vortex shedding can be suppressed by the unsteady stress terms and a time-independent solution can be achieved. Importantly, the vortex shedding time-averaged effects are included in time-independent solutions. A numerical test has also indicated that solution of the time-averaged equations appears to be less sensitive to the turbulence model than unsteady solutions.

Chapter 7 Conclusions and Suggestions

Some numerical investigations have been carried out towards understanding and predicting unsteady flows in turbomachinery. The principal part of the present work is the development of efficient frequency domain methods for unsteady flows around oscillating blades. To start with, a quasi 3-D time-linearized Euler/Navier-Stokes solver has been developed. Based on the time-linearized method, a novel quasi 3-D nonlinear harmonic Euler/Navier-Stokes method has been developed. Finally, some numerical efforts have been made to address modelling issues on trailing edge vortex shedding. The present work is concluded in the following three sections, and the chapter ends with a discussion of suggestions for the future development.

7.1 Time-Linearized Euler/Navier-Stokes Method

The time-linearized Euler method was originally presented by Ni (1974), currently this method and its Navier-Stokes version have been widely used in industry to compute unsteady flows in turbomachinery. The main purpose of the development of a quasi 3-D time-linearized method in the present work is that this method is the baseline method for the development of a nonlinear harmonic Euler/Navier-Stokes method.

In Chapter 2, the development of the quasi 3-D time-linearized Euler/Navier-Stokes method has been presented. In this method, the unsteady flow is decomposed into a **steady flow** plus a harmonically varying unsteady perturbation. Through the linearization, the original unsteady Euler/Navier-Stokes equation is divided into two equations, a steady flow equation and a time-linearized perturbation equation. In the time-linearized Navier-Stokes perturbation equation, the viscosity is frozen to its steady value, effectively the perturbation of the viscosity is neglected. A pseudo time-marching technique is introduced to make both the steady flow equation and the time-

linearized perturbation equation time-independent, so the time-marching method can be used. In the present work, a cell-vertex scheme is implemented to discritize the steady and perturbation equations in space and the 4-stage Runge-Kutta scheme is used to integrate them in the pseudo-time domain. In order to avoid the spurious reflection in the far-field boundaries when solving the perturbation equations, 1-D/2-D nonreflecting boundary conditions are applied. A slip-wall boundary condition is developed for solving the time-linearized Navier-Stokes perturbation equations.

The present quasi 3-D time-linearized Euler/Navier-Stokes method has been extensively validated, as presented in Chapter 3. An excellent agreement is achieved between the present calculation and a well-developed analytic method LINSUB for an oscillating flat plate cascade. A satisfactory comparison between the present calculation and LINSUB is obtained for a high frequency forced response case induced by incoming wakes for a flat plate cascade. Calculated results for an oscillating turbine cascade agree reasonably well with the experiment data. A calculation for a compressor cascade confirms that the time-linearized Euler method works well for transonic unsteady flows provided that the shock wave is sufficiently smeared and the shock oscillating amplitude is small. Calculated results for a laminar and a turbulent unsteady boundary layers are in good agreement with analytical solutions and other well-known numerical results. Finally, a calculation of an oscillating compressor cascade with a high incidence shows good comparison between calculated results and experimental data.

7.2 Nonlinear Harmonic Euler/Navier-Stokes Method

Based on a novel nonlinear approach proposed by He (1996a), a quasi 3-D nonlinear harmonic Euler/Navier-Stokes method has been developed, as described in Chapter 4. In this method, the unsteady flow is decomposed to be a **time-averaged flow** plus an unsteady perturbation. The time-averaged flow equations are given by time-averaging unsteady Euler/Navier-Stokes equations. Due to the nonlinearity of

unsteady equations, time-averaging produces extra 'unsteady stress' terms in the time-averaged equations. These unsteady stress terms are evaluated from unsteady perturbations. The unsteady perturbations are obtained by solving quasi-linear harmonic perturbation equations, while the coefficients of perturbation equations come from the solution of the time-averaged equations. Therefore, the time-averaged equations and harmonic perturbation equations interact each other. In order to ensure a good convergence and accuracy of a solution, a strong coupling method is applied to solve the time-averaged equations and harmonic perturbation equations simultaneously in a pseudo-time domain. The nonlinear effects are included in a coupling solution between the time-averaged flow and unsteady perturbations. The solution methods in the present nonlinear harmonic Euler/Navier-Stokes method are very similar to those used in the time-linearized Euler/Navier-Stokes method. The cell-vertex scheme is implemented for the spatial discretization and the 4-stage Runge-Kutta scheme is applied for the temporal discretization. In order to effectively handle the strong nonlinearity in the flow field produced by a large amplitude of shock wave oscillation, an approximate approach to linearize the pressure sensor in the artificial smoothing terms is implemented.

The effectiveness of the nonlinear harmonic Euler/Navier-Stokes method has been checked by calculations of transonic unsteady flows in a divergence duct, a biconvex cascade, a transonic diffuser and a compressor cascade. The calculated results are compared with a well-documented nonlinear time-marching method, the time-linearized Euler/Navier-Stokes method and experimental data. The comparisons have shown that the validity of the time-linearized method for unsteady flows is highly subject to the strength of nonlinearity in flow fields. A nonlinear harmonic analysis can considerably improve the numerical results over a linear analysis when the nonlinear effects cannot be ignored. However, the limitation of the nonlinear harmonic method has also been observed from calculations. The limitation is likely due to the quasi-linear characteristics of the present nonlinear harmonic method. Numerical tests have shown that a nonlinear harmonic analysis typically needs 60% of

the CPU time more than that required for a time-linearized analysis, it is still much more efficient than a nonlinear time-marching calculation.

7.3 Numerical Investigations on Trailing Edge Vortex Shedding

The major issue addressed in this part of work is: can we produce a time-independent solution by solving time-averaged equations when trailing edge vortex can be resolved in a calculation? This issue originally arises from the consideration of a time-linearized analysis and a nonlinear harmonic analysis in which a time-independent solution must be required. Actually it is a general concern in turbomachinery. To investigate this issue, the work starts with unsteady calculations of trailing edge vortex shedding from a circular cylinder and a VKI turbine blade using a multi-block unsteady Navier-Stokes solver. Based on the unsteady calculation results, the unsteady stresses due to trailing vortex shedding are worked out. Finally the time-averaged equations with known vortex shedding unsteady stresses are solved. Based on the present numerical study, several conclusions can be drawn as follows:

- Numerical results have shown that the structure and the frequency of vortex street can be well predicted by the present unsteady calculations. However, the unsteady calculation of vortex shedding is highly sensitive to the turbulence model and artificial smoothing. The numerical tests have also confirmed that the computational cost for an unsteady calculation of trailing edge vortex shedding in turbomachinery is very high.

- The structures of the three primary unsteady stresses $(\overline{(\rho u)'u'}, \overline{(\rho u)'v'}, \overline{(\rho v)'v'})$ produced by the trailing edge vortex shedding are not very complex. All of them reach their peak values roughly at the end of vortex shedding formation region, then decay rapidly along the wake. The structures of unsteady stresses generated by vortex shedding from the VKI turbine blade are similar to those generated by

vortex shedding from a circular cylinder. The topologies of vortex shedding unsteady stresses in a turbulent flow case are very similar to those in a laminar flow case, but the peak values of unsteady stresses in the laminar flow case are higher.

- A time-independent solution for vortex shedding can be achieved by solving time-averaged equations and the unsteady stresses are effective in suppressing vortex shedding. Importantly, the time-independent solution agrees with the time-averaged solution produced by unsteady calculations. Although numerical tests have shown that vortex shedding can be suppressed by other approaches, such as the excessive artificial smoothing or different turbulence models, the solutions are very different compared with time-averaged solutions. A numerical test has indicated that the solution by solving time-averaged equations appears to be less sensitive to the turbulence model than an unsteady solution.

7.4 Suggestions for the Future Work

As far as the time-linearized and nonlinear harmonic method is concerned, several outstanding issues need to be addressed in the near future. The first is that the validity of freezing the viscosity in the perturbation equations to its steady/time-averaged value should be further checked, especially for very low frequency unsteady flows. The second issue is on the linearization of the artificial smoothing. Although an approximate approach is implemented in the present nonlinear harmonic method to linearize pressure sensors, a more accurate approach is desired to be pursued. This might be particularly important for the flow with very strong nonlinearity. The another issue is on the acceleration of Navier-Stokes time-linearized and nonlinear harmonic analyses. In the present work, a 2-grid technique is applied to accelerate the convergence of the linear and nonlinear harmonic Navier-Stokes method. However, because the time accuracy is not a concern in a frequency domain method, a more efficient multigrid technique is highly preferable to be implemented. Meanwhile,

further investigations on mesh-dependence of this nonlinear harmonic method should be carried out.

Many latest numerical and experimental results have demonstrated that the 3-D effects could be potentially important in the prediction of unsteady flows in turbomachinery. The extension of the present quasi 3-D method to a fully 3-D method should be pursued. From the methodology point of view, the extension work is not difficult, it can be done by either extending the present solver to a fully 3-D one or developing one from a well-developed fully 3-D steady or unsteady solver. However, the validation of 3-D methods would be difficult because very few 3-D unsteady experimental data are available so far.

Another area of interest for blade flutter analysis is to include the interaction effects from other sources of unsteadiness, such as bladerow interactions, inlet distortions etc. In the time-linearized methods, the interaction between different unsteady disturbances is completely missed because the unsteady perturbations are based on a steady flow field. This interaction could be realised in a solution by the nonlinear harmonic method through time-averaged flows. In the nonlinear harmonic method, the time-averaged flow can be changed by the unsteady perturbations and vice versa in a coupling procedure. The unsteady stresses produced by different unsteady disturbances can be summed up to construct a total unsteady stress to put into the time-averaged equations. The communication between different disturbances can indirectly build up through time-averaged flows. The investigation in this direction is worthwhile to be carried out in the future. For turbomachine designers, it is highly desirable to develop a design method which is efficient while it can take account of unsteady effects from different disturbances. The nonlinear harmonic method is promising to be developed into this kind of design method.

Trailing edge vortex shedding is one of the most difficult problems in turbomachinery because it has a very small length and time scale. The modelling of

the trailing edge vortex shedding is a completely new way to look at this problem. The present work on the modelling issues is important because it has conceptually proved that vortex shedding can be suppressed by the unsteady stresses and a time-independent solution can be produced by solving time-averaged equations. However, how to model these unsteady stresses still remains an open question and much more effort needs to be made. Luckily the turbomachinery researches can benefit from the study on vortex shedding behind cylinders which is much less affected by geometrical constraints. Therefore the effort needs to be made to construct a function in which the unsteady stresses are correlated to Reynolds numbers and cylinder geometry in circular cylinder flows. This function then can be extrapolated from cylinder flows to turbomachine flows. At the early stage, all the investigations can be carried out on laminar flows in order to avoid any uncertainties of turbulence models. For turbulent flows, improved turbulence models such as Reynolds stress models or even the Large-Eddy Simulation (LES) technique must be implemented to investigate unsteady stresses more accurately. The relationship between the unsteady stresses and boundary layer characteristics needs to be constructed.

BIBLIOGRAPHY

Ackerberg, R. C. and Philips, J. H., (1972), " The Unsteady Laminar Boundary Layer on a Semi-infinite Flat Plate due to Small Fluctuations in the Magnitude of the Free-Stream Velocity", *Journal of Fluid Mechanics,* Vol. 51, Part 1

Adamczyk, J. J., (1985), " Model Equations for Simulating Flows in Multistage Turbomachinery", ASME Paper 85-GT-226

Adamczyk, J. J., Celestina, M. L., Beach, T. A., and Barnett, M., (1989), " Simulation of Three-Dimensional Viscous Flow Within a Multistage Turbine", ASME Paper 89-GT-152

Allmaras, S. R., (1989), " A Coupled Euler/Navier-Stokes Algorithm for 2-D Unsteady Transonic Shock/Boundary Layer Interaction", GTL Report # 196, Massachusetts Institute of Technology

Arnone, A., (1996), " IGV-Rotor Interaction Analysis in a Transonic Compressor Using the Navier-Stokes Equations", ASME paper 96-GT-141

Arnone, A. and Pacciani R., (1997), " Numerical Prediction of Trailing Edge Wake Shedding", ASME Paper 97-GT-89

Ayer, T. C. and Verdon, J. M., (1996), " Validation of Nonlinear Unsteady Aerodynamic Simulator for Vibrating Blade Rows", ASME Paper 96-GT-340

Baldwin, B. S. and Lomax, H., (1978), " Thin Layer Approximation and Algebraic Model for Separated Turbulent Flows", AIAA Paper 78-257

Bendiksen, O. O., (1991), " A New Approach to Computational Aeroelasticity" AIAA Paper 91-0939

Bogar, T. J., Sajben, M., and Kroutil, J. C., (1983), " Characteristic Frequencies of Transonic Diffuser Flow Oscillations", *AIAA Journal*, Vol. 21, No.9

B ö lcs, A. and Fransson, T. H., (1986), " Aeroelasticity in Turbomachines Comparison of Theoretical and Experimental Cascade Results", Communication du Laboratoire de Thermique Appliquee et de Turbomachines, No. 13, Lausanne, EPEL.

Buffum, D. H., (1995), "Blade Row Interaction Effects on Flutter and Forced Response", *Journal of Propulsion and Power,* Vol.11, No.2

Cantwell, B. and Coles, D., (1983), "An Experimental Study of Entrainment and Transport in the Turbulent Near Wake of a Circular Cylinder", *Journal of Fluid Mechanics,* Vol. 136, pp.321-374

Caspar, J. R. and Verdon, J. M., (1981), " Numerical Treatment of Unsteady Subsonic Flow Past an Oscillating Cascade", *AIAA Journal,* Vol.19

Cebeci, T., (1977), " Calculation of Unsteady Two-Dimensional Laminar and Turbulent Boundary Layers with Fluctuations in External Velocity", Proceeding of Royal Society (London), Vol. 355

Celestina, M. L., Mulac, R. A., and Adamczyk, J. J., (1986), "A Numerical Simulation of the Inviscid Flow Through Counterroting Propeller", ASME Paper 86-GT-138

Chen, J. P, Celestina, M. L. and Adamczyk, J. J., (1994), " A New Procedure for Simulating Unsteady Flows Through Turbomachinery Blade Passages", ASME Paper 94-GT-151

Chew, J. W. and Marshall, J. G., (1997), " Part-Speed Flutter Analysis of a Wide-Chord Fan Blade", Proceeding of the 8th International Symposium on Unsteady Aerodynamics and Aeroelasticity of Turbomachines, Stockholm

Cicatelli, G. and Sieverding, C. H. (1995), " A Review of the Research on Unsteady Turbine Blade Wake Characteristics", AGARD PEP Symposium on Loss Mechanisms and Unsteady Flows in Turbomachines, Derby, U.K.

Cicatelli, G. and Sieverding, C. H., (1996), "The Effect of Vortex Shedding on the Unsteady Pressure Distribution Around the Trailing Edge of a Turbine Blade", ASME Paper 96-GT-39

Copenhaver, W. W., Puterbauch, S.L., and Hah, C., (1993), " Three-Dimensional Flow Analysis Inside Turbomachinery Stages with Steady and Unsteady Navier-Stokes Method", ISABE 93-7095

Currie, T. C. and Carscallen, W. E., (1996), "Simulation of Trailing Edge Vortex Shedding in a Transonic Turbine Cascade", ASME Paper 96-GT-483

Dawes, W. N., (1988), " Development of a 3D Navier-Stokes Solver for Application to all Types of Turbomachinery", ASME Paper 88-GT-70

Dean, R.C.Jr., (1959), "On the Necessity of Unsteady Flow in Fluid Machines", *Trans ASME Journal of Basic Engineering,* Vol. 81, No.24

Denton, J. D., (1982), " An Improved Time Marching Method for Turbomachinery Flows", ASME Paper 82-GT-239

Denton, J. D., (1990), " The Calculation of Three Dimensional Viscous Flow Through Multistage Turbomachines", ASME Paper 90-GT-19

Denton, J. D., (1993), "Loss Mechanisms in Turbomachines", 1993 ASME IGTI Scholar Award Paper

Erdos, J.I., Alzner, E., and Mcnally, W., (1977), "Numerical Solution of Periodic Transonic Flow Through a Fan Stage", *AIAA Journal*, Vol.15, No.11

Fransson, T. H., (1984), " Numerical Investigation of Unsteady Subsonic Compressible Flows Through an Oscillating Cascade", ASME Paper 86-GT-304

Fransson, T. H. and Pandolfi, M., (1986), " Numerical Investigation of Unsteady Subsonic Compressible Flows Through an Oscillating Cascade", ASME Paper 86-GT-304

Fransson, T. H. and Verdon, J. M., (1993), " Panel Discussion on Standard Configurations for Unsteady Flow Through Vibrating Axial-Flow Turbomachine Cascades", in *Unsteady Aerodynamics, Aeroacoustics, and Aeroelasticity of Turbomachines and Propellers,* H. M. Atassi, ed., Springer-Verlag, New York, pp. 859-889

Gerolymos, G. A., (1988), " Numerical Integration of the 3D Unsteady Euler Equations for Flutter Analysis of Axial Flow Compressors", ASME Paper 88-GT-255

Giles, M. B., (1988), " Calculation of Unsteady Wake Rotor Interaction", *AIAA Journal of Propulsion and Power,* Vol.4, No.4

Giles, M. B., (1990a), "Stator/Rotor Interaction in a Transonic Turbine", *AIAA Journal of Propulsion and Power,* Vol.6, No.5

Giles, M. B., (1990b), "Nonreflecting Boundary Conditions for Euler Equation Calculations", *AIAA Journal, Vol. 28, No.12*

Giles, M. B. and R., Haimes, (1991a), " Validation of a Numerical Method for Unsteady Flow Calculations", ASME paper 91-GT-271

Giles, M. B., (1991b), "Flutter and Forced Response Analysis Using the Three-Dimensional Linearized Euler Equations", a private communication, MIT

Giles, M. B., (1992), " An Approach for Multi-Stage Calculations Incorporating Unsteadiness", ASME Paper 92-GT-282

Gostelow, J. P. and Solomon, W. J., (1996), " Some Unsteady Effects on Flows over Blading", IMechE conference paper, S461/010/96

Gundy-Burlet, K. L., and Dorney, D. J., (1997), " Physics of Airfoil Clocking in a Axial Compressors", ASME Paper 97-GT-444

Hall, E. J., (1997), " Aerodynamic Modeling of Multistage Compressor Flowfields - Part 2: Modeling Deterministic Stresses", ASME Paper 97-GT-345

Hall, K. C. and Crawley, E. F., (1989), "Calculation of Unsteady Flows in Turbomachinery Using the Linearized Euler Equations", *AIAA Journal,* Vol.27, No.6

Hall, K. C. and Lorence, C. B., (1992), " Calculation of Three-Dimensional Unsteady Flows in Turbomachinery Using the Linearized Harmonic Euler Equations", ASME Paper 92-GT-136

Hall, K. C., Clark, W. S. and Lorence, C. B., (1994), "A Linearized Euler Analysis of Unsteady Transonic Flows in Turbomachinery", *Journal of Turbomachinery,* Vol. 116

Han, L. S. and Cox W. R., (1982), " A Visual Study of Turbine Blade Pressure Side Boundary Layer", ASME Paper 82-GT-47

He, L., (1990a), " Unsteady Flows Around Oscillating Turbomachinery Blades", Ph.D Thesis, Department of Engineering, University of Cambridge, September 1990

He, L., (1990b), "An Euler Solution for Unsteady Flows Around Oscillating Blades", *ASME Journal of Turbomachinery*, Vol.112, pp.714-722

He, L., (1992), "A Method of Simulating Unsteady Turbomachinery Flows With Multiple Perturbations", *AIAA Journal,* Vol. 30, No.12

He, L., (1993a), " A New Two-Grid Acceleration Method for Unsteady Navier-Stokes Calculations", *AIAA Journal of Propulsion and Power,* Vol.9, No. 2

He. L. and Denton, J. D., (1993b), " Inviscid-Viscous Coupled Solution for Unsteady Flows through Vibrating Blades, Part 1. Methodology", *Journal of Turbomachinery*, Vol. 115, No.4

He, L. and Denton, J. D., (1994a), " Three-Dimensional Time-Marching Inviscid and Viscous Solutions for Unsteady Flows Around Vibrating Blades", ASME *Journal of Turbomachinery,* Vol. 116, pp.469-476

He, L., (1994b), "Integration of 2-D Fluid/Structure Coupled System for Calculations of Turbomachinery Aerodynamic/Aeroelastic Instabilities", *Journal of Computational Fluid Dynamics,* Vol.3, pp.217-231

He, L., (1996a), " I. Modelling Issues for Computation of Unsteady Turbomachinery Flows" in "Unsteady Flows in Turbomachinery" , VKI Lecture Series 1996-05

He, L., (1996b), unpublished work, University of Durham

He, L., (1997a), " Computational Study of Rotating Stall Inception in Axial-Flow Compressors", *Journal of Power and Propulsion*, Vol.13, No.1

He, L., (1997b), "Computation of Unsteady Flow Through Steam Turbine Blade Rows at Partial Admission", *IMechE Journal of Power & Energy,* Vol.211, Part A

He, L., (1997c), a private communication, University of Durham

Hesieh, T., Wardlaw, A. B. Jr., Collins, P., and Coakley, T. J., (1984), " Numerical Investigation of Unsteady Inlet Flow Fields", AIAA Paper 84-0031

Holmes, D. G. and Chung, H. A., (1993), "2D Linearized Harmonic Euler Flow Analysis for Flutter and Forced Response", in *Unsteady Aerodynamics, Aeroacoustics, and Aeroelasticity of Turbomachines and Propellers,* ed. Atassi, H.M., Springer-Verlag, New York

Holmes, D. G. and Lorence, C. B., (1997), "Three Dimensional Linearized Navier-Stokes Calculations for Flutter and Forced Response", Proceeding of the 8th International Symposium on Unsteady Aerodynamics and Aeroelasticity of Turbomachines, Stockholm, Sweden

Huff, D. L., (1991), a private communication, NASA Lewis Research Center

Jameson, A., Schmidt, W. and Turkel, E., (1981), "Numerical Solutions of the Euler Equation by Finite Volume Method Using Runge-Kutta Time-Stepping Scheme", AIAA Paper 81-1259

Jameson, A., (1991), " Time Dependent Calculations Using Multigrid with Application to Unsteady Flows Past Airfoils and Wings", AIAA Paper 91-1597

Joubert, H., (1984), " Supersonic Flutter in Axial Flow Compressor", Proceeding of the 3rd Symposium on Unsteady Aerodynamics and Aeroelasticity of Turbomachines and Propellers, Cambridge, U.K.

Jung, A. R., Mayer, J. F. and Stetter, H., (1997), " Prediction of 3D-Unsteady Flow in an Air Turbine and a Transonic Compressor Including Blade Gap Flow and Blade Row Interaction", ASME Paper 97-GT-94

Karlsson, S. K. F., (1959), " An Unsteady Turbulent Boundary Layer", *Journal of Fluid Mechanics,* Vol.5, pp. 622- 636

Koya, M. and Kotake, S., (1985), " Numerical Analysis of Fully Three-Dimensional Periodic Flows Through a Turbine Stage", *Journal of Engineering for Gas Turbines and Power,* Vol. 107

Krouthen, B. and Giles, M.B., (1988), " Numerical Investigation of Hot Streaks in Turbines", AIAA Paper 88-3015

Lane, F., (1956), " System Mode Shapes in Flutter of Compressor Blade Rows", *Journal of Aeronautical Sciences*, Vol. 23, No. 1

Lightwill, M. J., (1954), " The Response of Laminar Skin Friction and Heat Transfer to Fluctuations in the Stream Velocity", Proceedings of the Royal Society (London), Vol. A224

Linquist, D. and Giles, M. B., (1991), " On the Validity of Linearized Unsteady Euler Equations with Shock Capturing", AIAA Paper 91-1958

Linquist, D., (1991), " Computation of Unsteady Transonic Flowfields Using Shock Capturing and the Linear Perturbation Euler Equations", Ph.D thesis, Gas Turbine Laboratory, Massachusetts Institute of Technology

MacCormack, R. W., (1969), " The Effect of Viscosity in Hypervelocity Impact Cratering", AIAA Paper 69-354

Manna M. and Mulas, M., (1994), " Navier-Stokes Analysis of Trailing Edge Induced Unsteady Flow in a Turbine Blade", VKI Lecture Series 1994-06

Marshall, J.G. and Imregun, M., (1995), " A 3D Time-Domain Flutter Prediction Method for Turbomachinery Blades", Proceeding of International Symposium of Aeroelasticity and Structural Dynamics, Manchester, Royal Aeronautical Society, 42.1-42.14

Marshall, J. G. and Giles, M. B., (1997), "Some Applications of a Time-Linearized Euler Method to Flutter & Forced Response in Turbomachinery", Proceeding of the 8th International Symposium on Unsteady Aerodynamics and Aeroelasticity of Turbomachines, Stockholm, Sweden

Massey, B. S., (1983), " Mechanics of Fluids", 6th edition, Van Nostrand Reinhold (UK)

McCormick, D. C., Paterson, R. W. and Weingold, H. D., (1988), "Experimental Investigation of Loading Effects on Simulated Compressor Airfoil Trailing-Edge Flowfields", AIAA Paper 88-0365

Menter, F. R., (1993), "Zonal Two-Equation $K-\omega$ Turbulence Models for Aerodynamic Flows", AIAA Paper 93-2906

Morreti, G., and Abbett, M., (1966), " A Time-Dependent Computational Method for Blunt Body Flows", *AIAA Journal,* Vol. 4, No. 12, pp. 2136-2141

Ni, R. H., (1974), "Nonstationary Aerodynamics of Arbitrary Cascades in Compressible Flow", Ph.D thesis, Stevens Institute of Technology, June 1974

Ni, R. H., (1989), " Prediction of 3D Multi Stage Flow Field Using a Multiple Grid Euler Solver", AIAA Paper 89-0203

Pandofi, M., (1980), " Numerical Experiments on Unsteady Flows through Vibrating Cascades", Proceeding of the 2nd Symposium on Unsteady Aerodynamics and Aeroelasticity of Turbomachines and Propellers, Lausanne, Switzerland

Rai, M. M., (1985), " Navier-Stokes Simulations of Rotor-Stator Interaction Using Patched and Overlaid Grids", AIAA Paper 85-1519

Rai, M. M., (1987), "Unsteady Three-Dimensional Navier-Stokes Simulations of Turbine Rotor-Stator Interaction", AIAA Paper 87-2058

Reynolds, W. C. and Hussain, A. K. M. F., (1972), " The Mechanics of an Organised Wave in Turbulent Shear Flow", Part 3. Theoretical Models and Comparisons with Experiments, *Journal of Fluid Mechanics*, Vol.54, pp. 263-288

Rhie, C. M., Gleixner, A. J., Spear, D. A., Fischberg, C. J., and Zacharias, R. M., (1995), " Development and Application of a Multistage Navier-Stokes Solver - Part I: Multistage Modelling Using Bodyforces and Deterministic Stresses", ASME Paper 95-GT-342

Roberts, Q. D. H and Denton, J. D., (1996), "Loss Production in the Wake of a Simulated Subsonic Turbine Blade", ASME Paper 96-GT-421

Roberts, Q. D. H, (1997), "The Trailing Edge Loss of Subsonic Turbine Blades", Ph.D dissertation, University of Cambridge, October 1997

Roe, P. L., (1981), " Approximate Riemann Solver, Parameter Vectors, and Difference Schemes", *Journal of Computational Physics*, Vol.43, No.2

Sajben, M., Bogar, T. J. and Kroutil, J. C., (1984), " Forced Oscillation Experiments in Supercritical Diffuser Flows", *AIAA Journal*, Vol.22, No.4

Salmon, J. T., Bogar, T. J. and Sajben, M., (1983), " Laser Doppler Velocimeter Measurements in Unsteady, Separated, Transonic Diffuser Flows", *AIAA Journal*, Vol.21 , No12

Silkowski, P. D. and Hall, K. C., (1997), " A Coupled Mode Analysis of Unsteady Multistage Flows in Turbomachinery", ASME Paper 97-GT-186

Verdon, J. M. and Caspar, J. R., (1984), " A Linearized Unsteady Aerodynamics Analysis for Transonic Cascades", *Journal of Fluids Mechanics,* Vol. 149

Verdon, J. M., (1993), " Unsteady Aerodynamic Methods for Turbomachinery Aeroelastic and Aeroacoustic Applications", *AIAA Journal*, Vol. 31, No.2, pp. 235-250

Whitehead, D. S., (1970), " Vibration and Sound Generation in a Cascade of Flat Plates in Subsonic Flow", A.R.C. R&M, No. 3865

Whitehead, D. S., (1982), " The Calculation of Steady and Unsteady Transonic Flow in Cascades", University of Cambridge, Department of Engineering Report CUED/A-Turbo/TR 118

Whitehead, D. S., (1987), " Classical Two-Dimensional Methods", AGRAD Manual on Aeroelasticity in Axial-Flow Turbomachines, *Unsteady Turbomachinery Aerodynamics,* Vol.1, AGRAD-AG-298

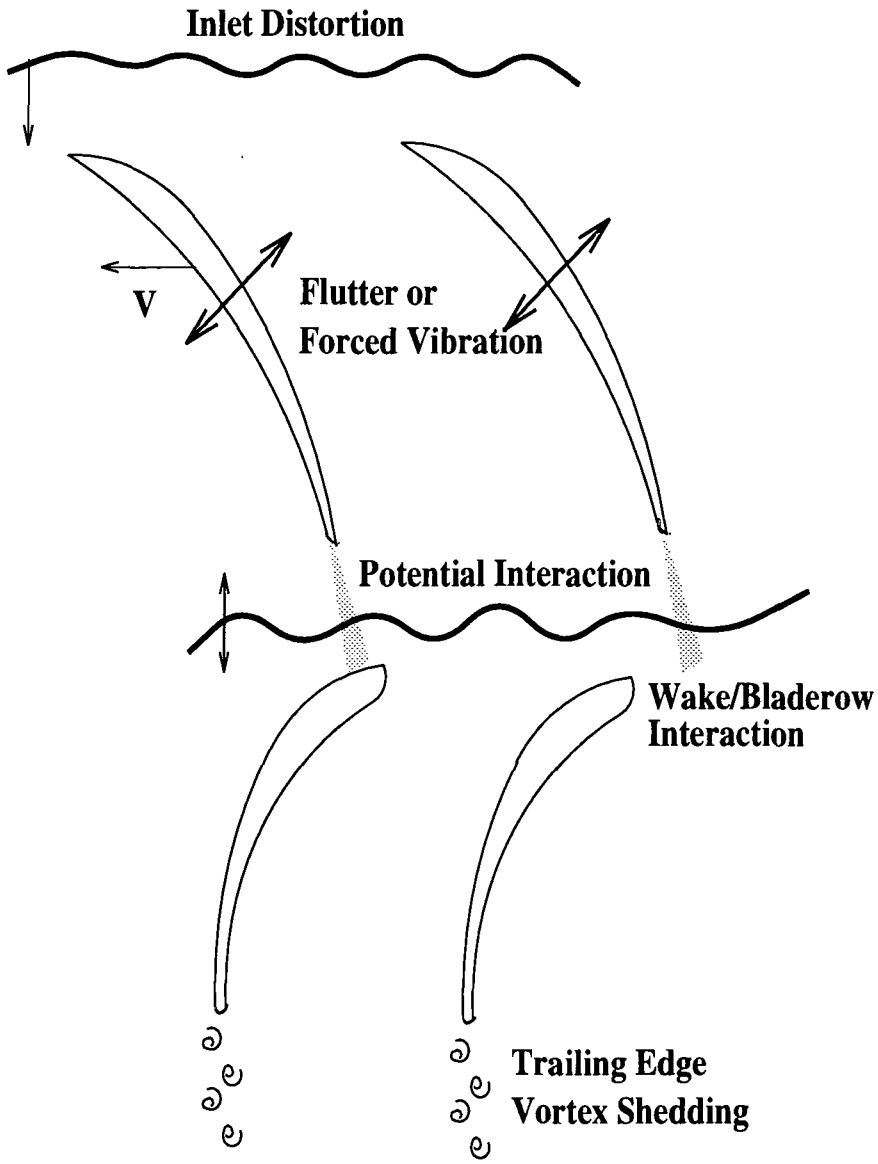

Fig. 1-1 Sources of Unsteadiness in Turbomachinery

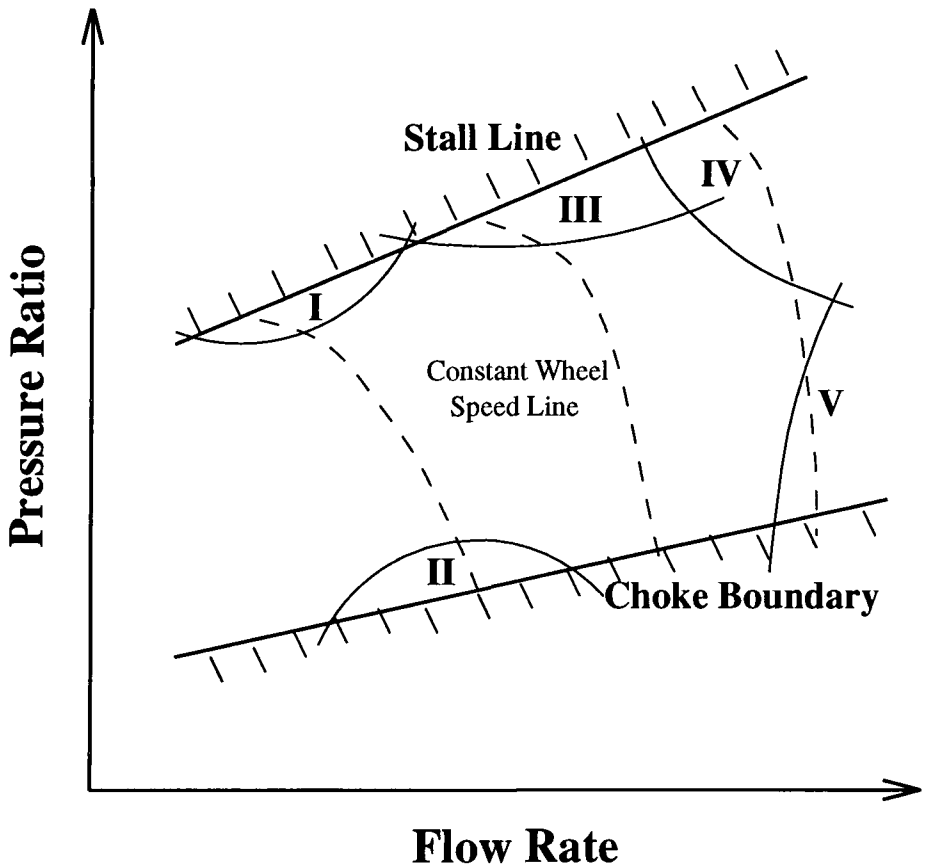

I. Subsonic/Transonic Stall Flutter

II. Choke Flutter

III. Supersonic Stall Flutter

IV. High Backpressure Supersonic Flutter

V. Low Backpressure Supersonic Flutter

Fig. 1-2 Blade Flutter Boundaries on Compressor Performance Map

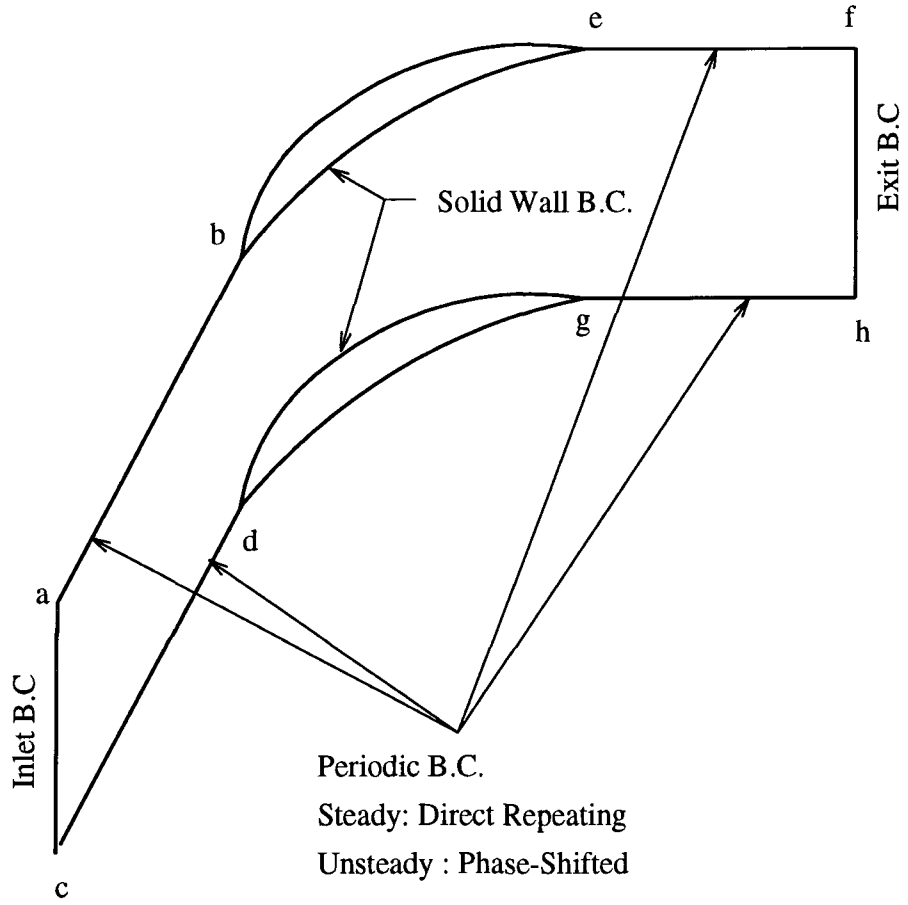

Fig. 1-3 A Single Blade-Blade Passage Computational Domain

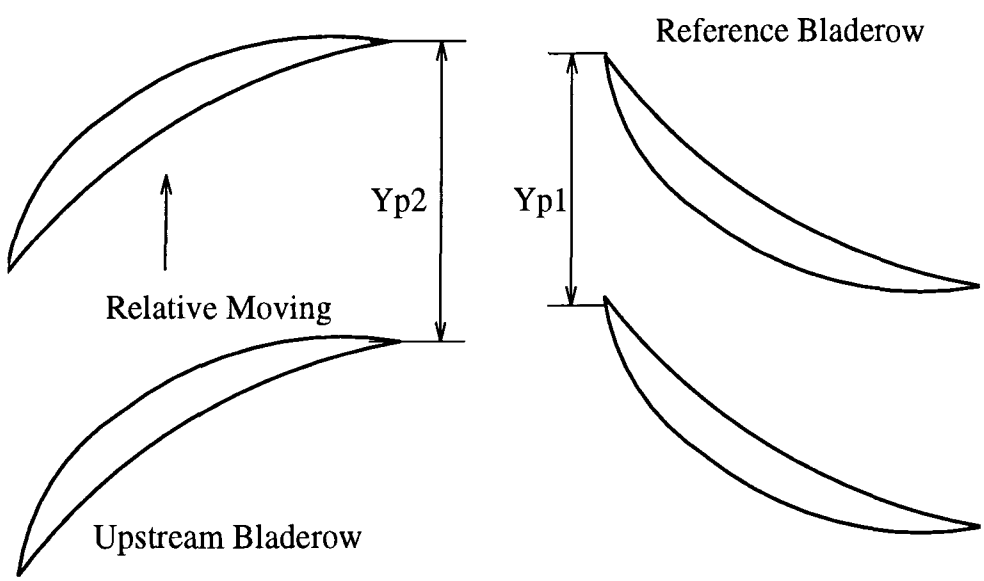

Fig. 1-4 A Single Blade-Blade Passage Computational Domain for a Stage

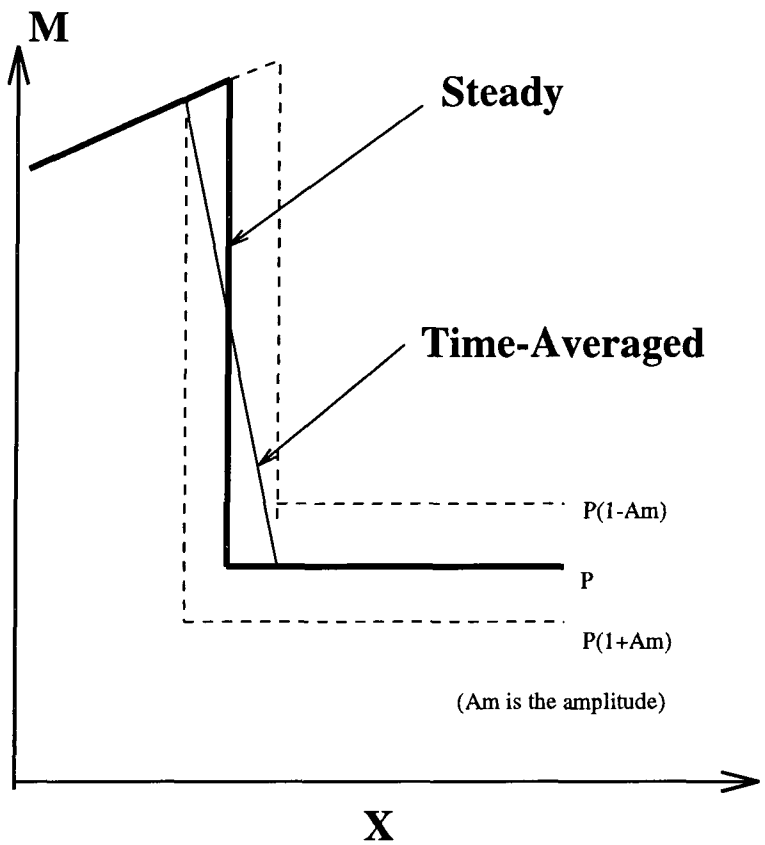

Fig. 1-5 Shock Oscillation due to Back Pressure Variation

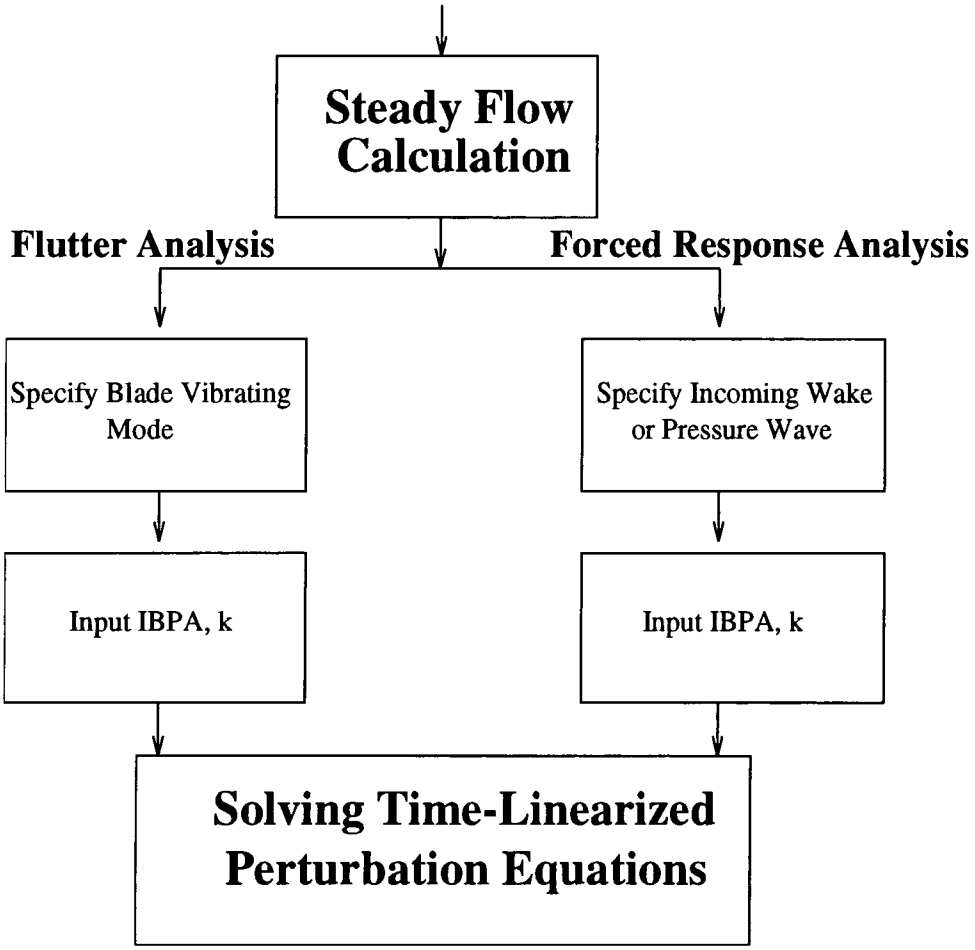

Fig. 2-1 Solution Procedure of a Time-Linearized Ananlysis

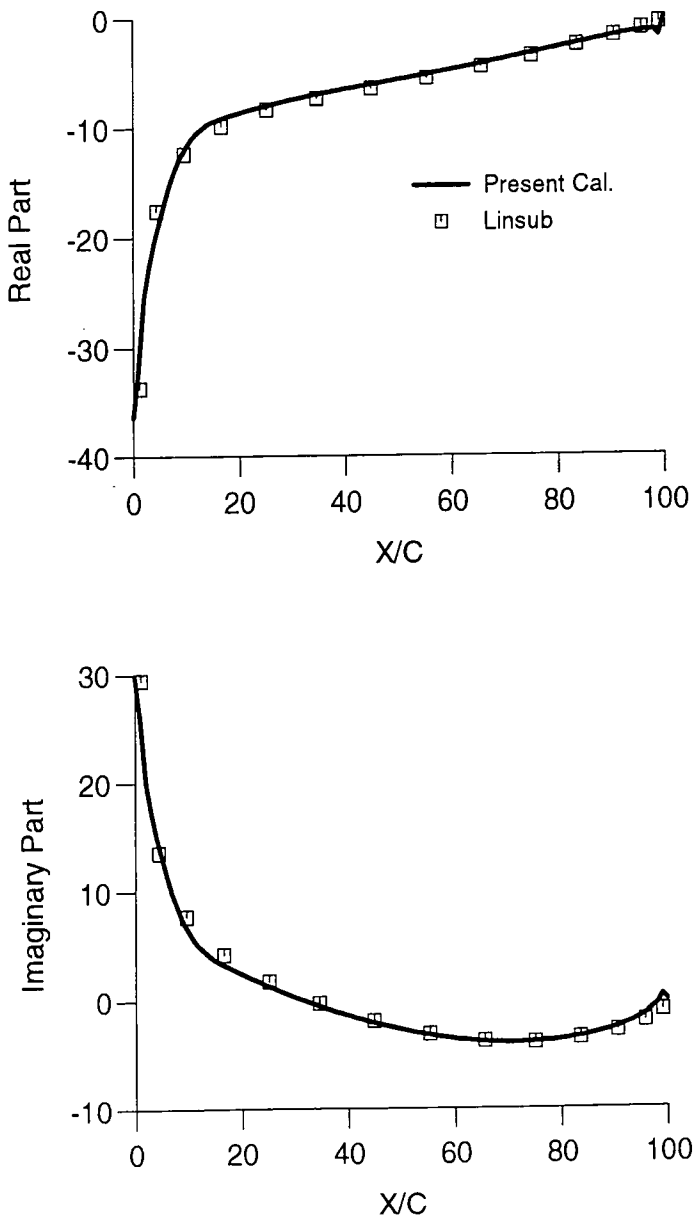

Fig. 3-1 Imaginary and Real Parts of Unsteady Pressure Coefficient Jump for an Oscillating Flat Plate Cascade (k = 0.57)

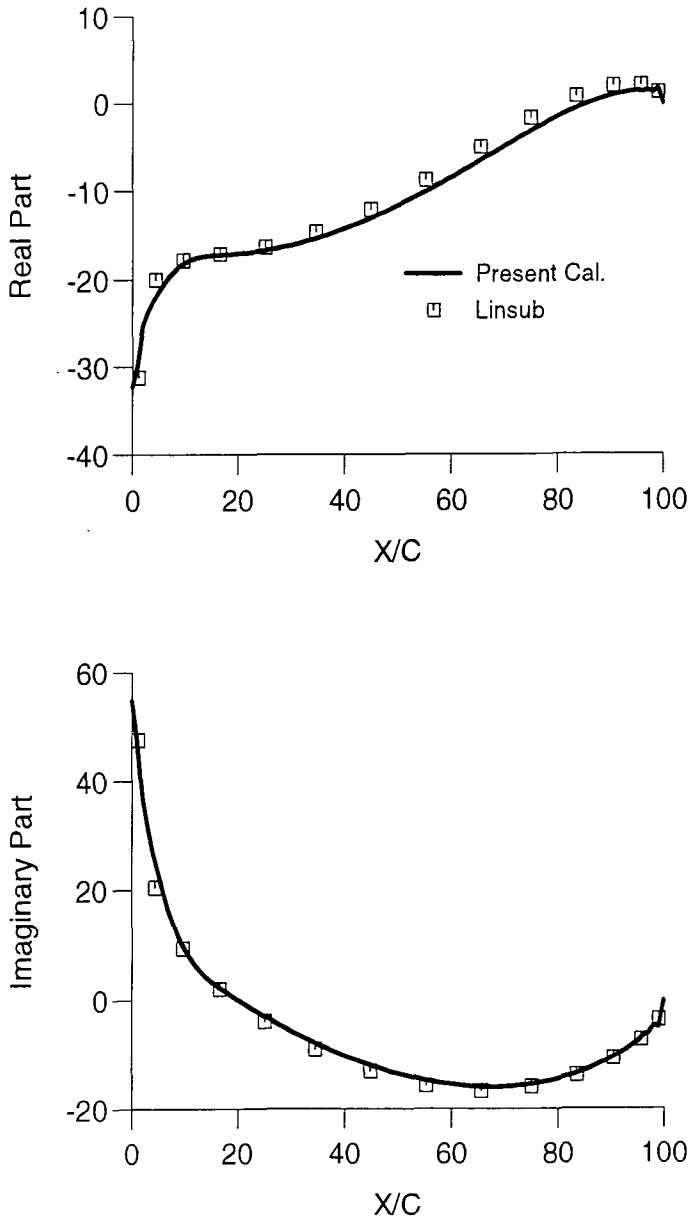

Fig. 3-2 Real and Imaginary Parts of Unsteady Pressure Coefficient Jump for an Oscillating Flat Plate Cascade (k = 1.714)

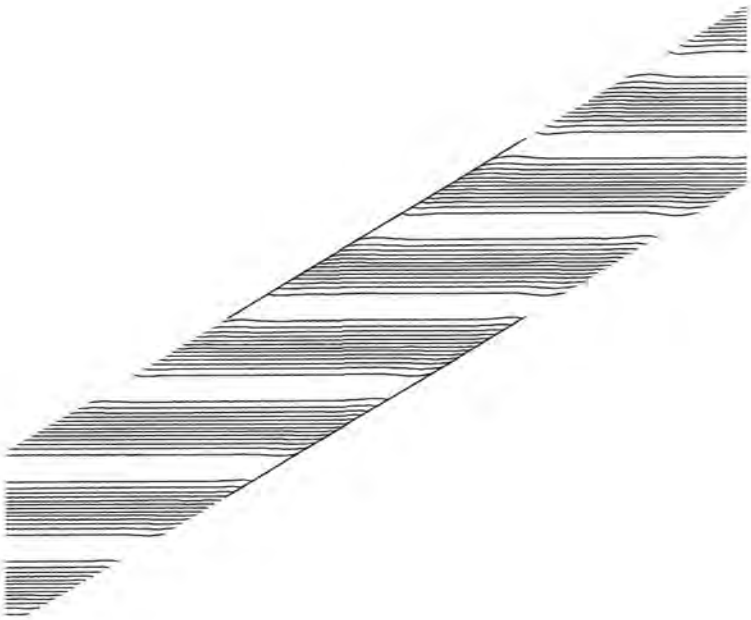

Fig. 3-3 Instantaneous First Harmonic Entropy Contour Map
(Incoming Wake Angle: 0 degree)

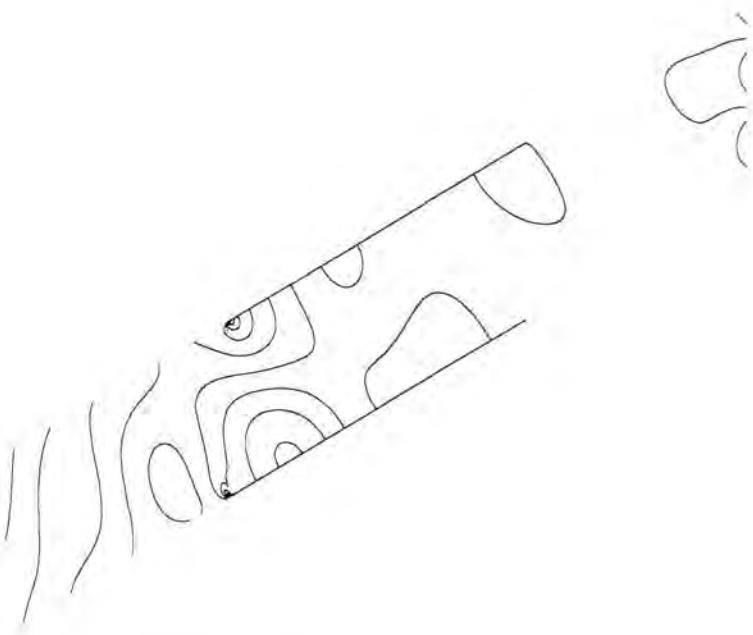

Fig. 3-4 Instantaneous First Harmonic Pressure Contour Map
(Incoming Wake Angle: 0 degree)

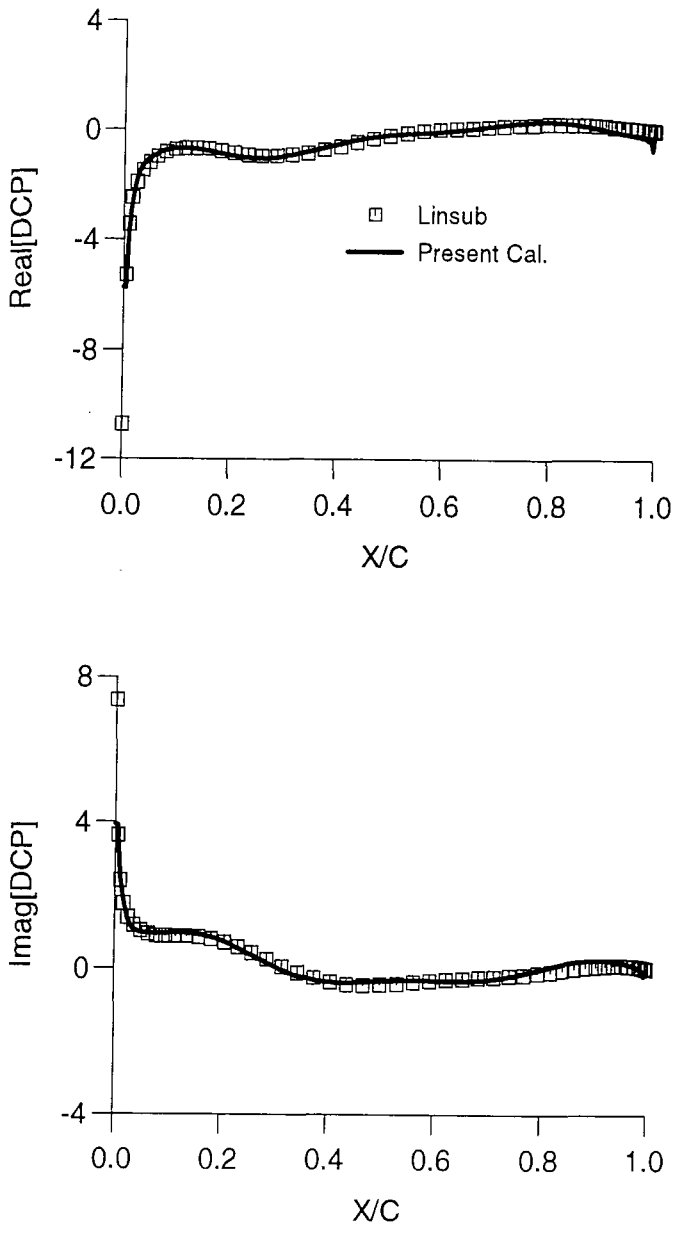

Fig. 3-5 Unsteady Pressure Coefficient Jump for a Flat Plate Cascade
(Incoming Wake Angle: 0 degree)

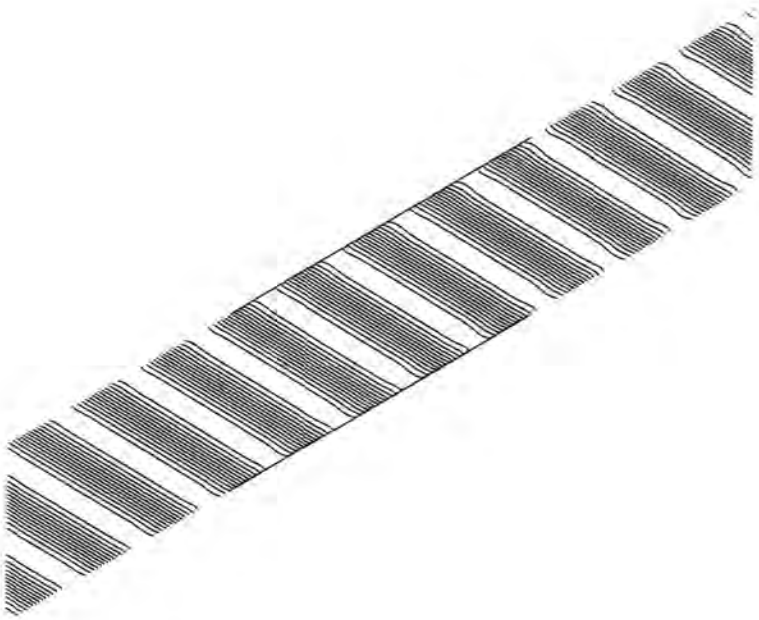

Fig. 3-6 Instantaneous First Harmonic Entropy Contour Map
(Incoming Wake Angle: -30 degree)

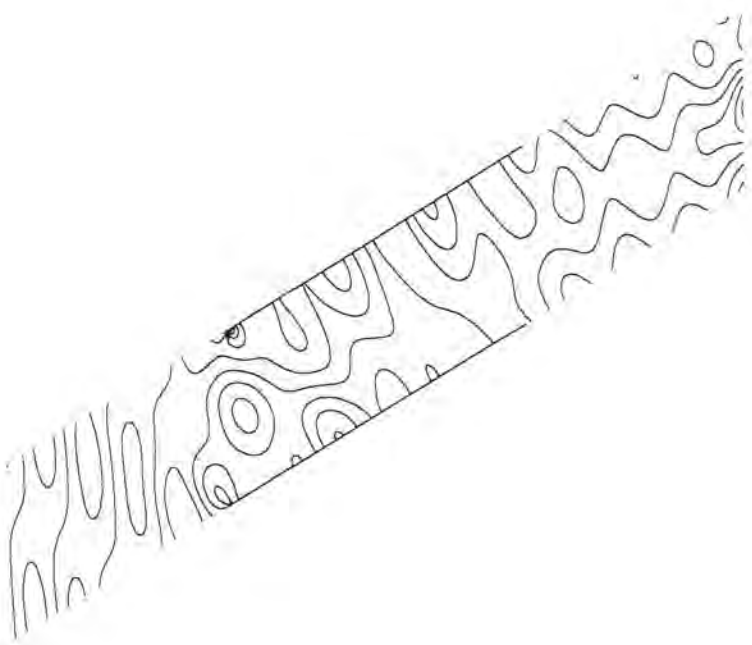

Fig. 3-7 Instantaneous First Harmonic Pressure Contour Map
(Incoming Wake Angle: -30 degree)

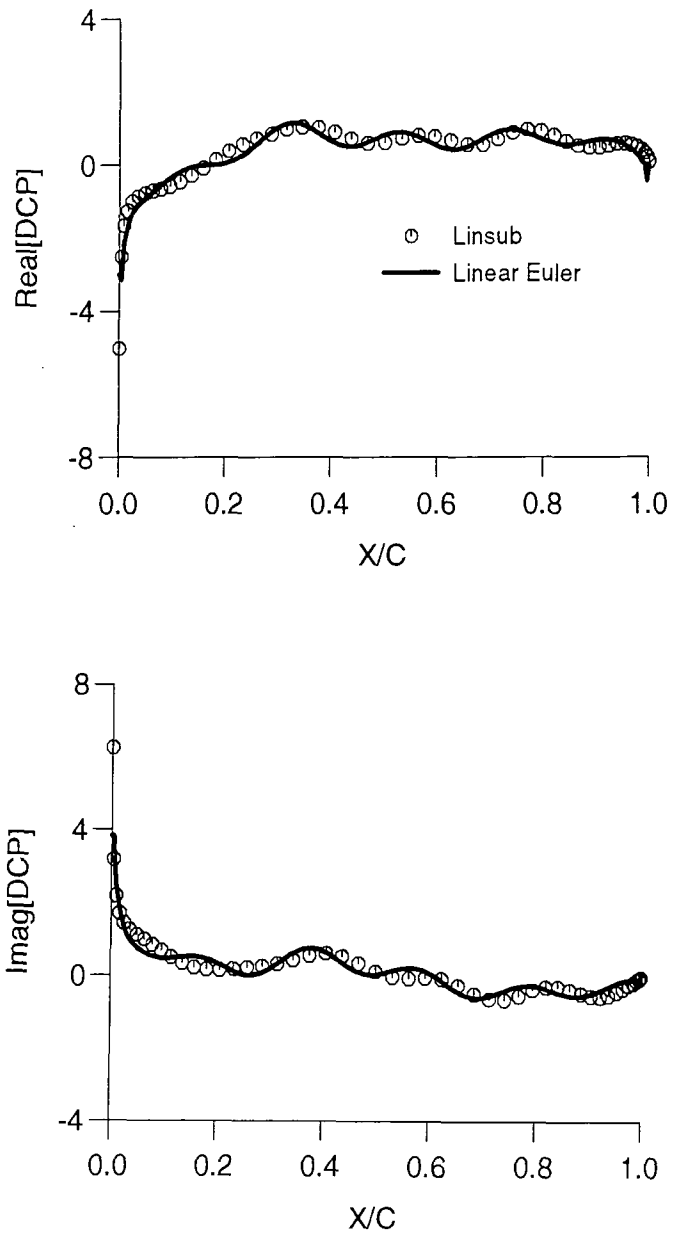

Fig. 3-8 Unsteady Pressure Coefficient Jump for a Flat Plate Cascade
(Incoming Wake Angle: -30 degree)

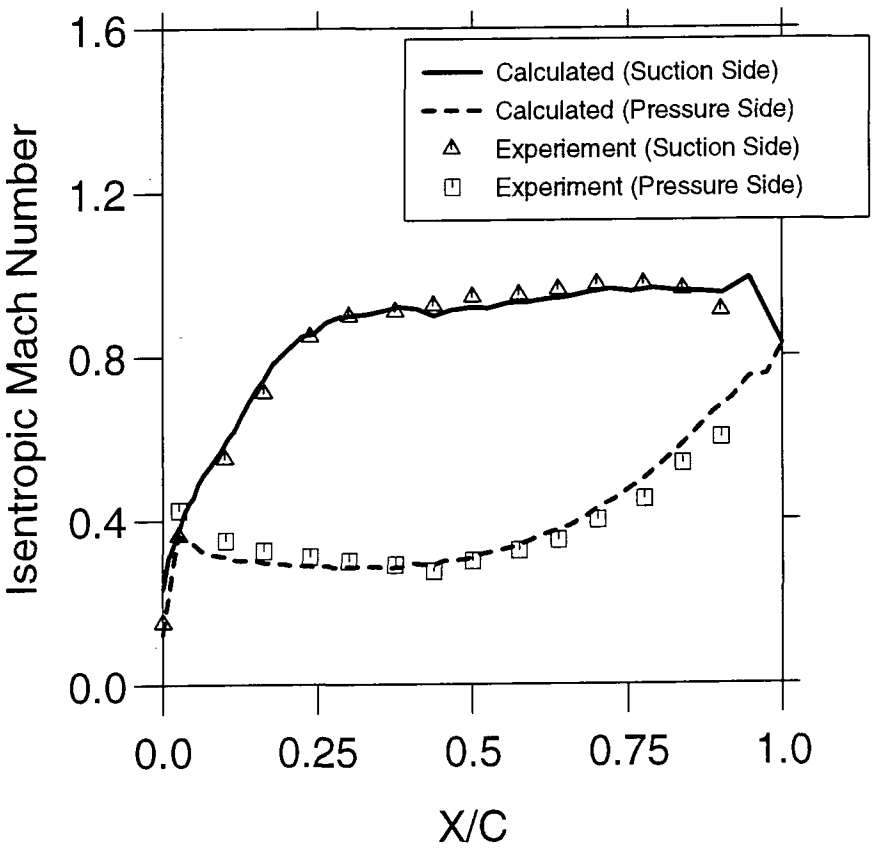

Fig. 3-9 Isentropic Mach Number Distribution for a Turbine Cascade

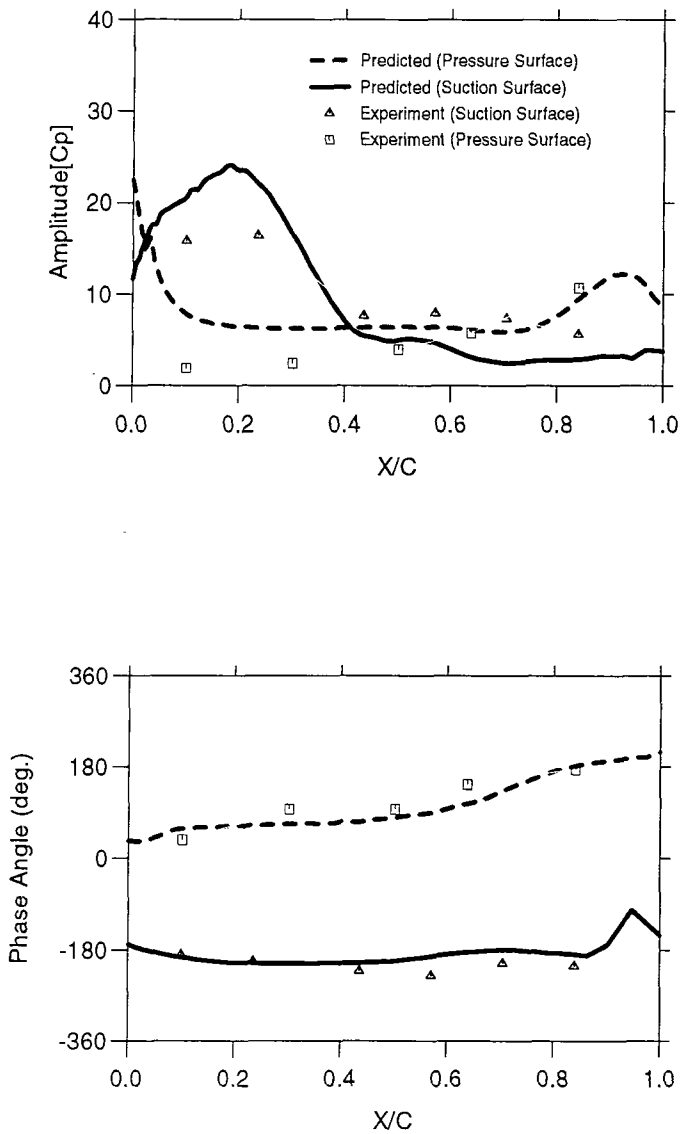

Fig. 3-10 Amplitude and Phase of Unsteady Pressure Coefficient Distribution for a Turbine Blade (IBPA = -90 deg.)

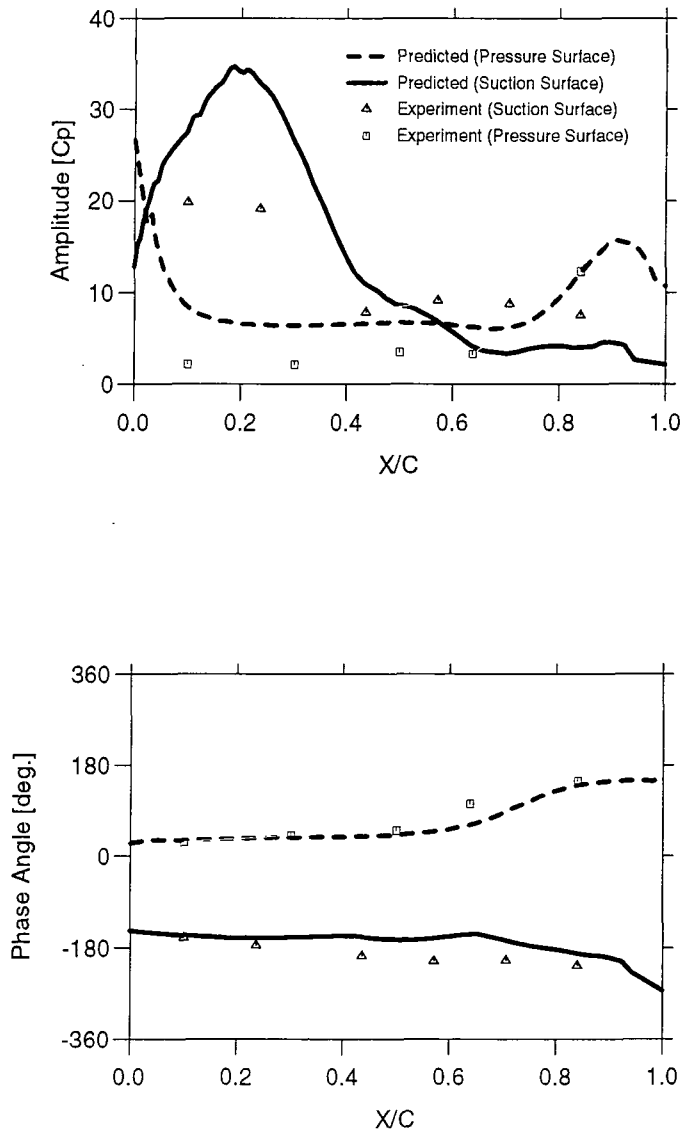

Fig. 3-11 Amplitude and Phase of Unsteady Pressure Coefficient Distribution for a Turbine Blade (IBPA = 180 deg.)

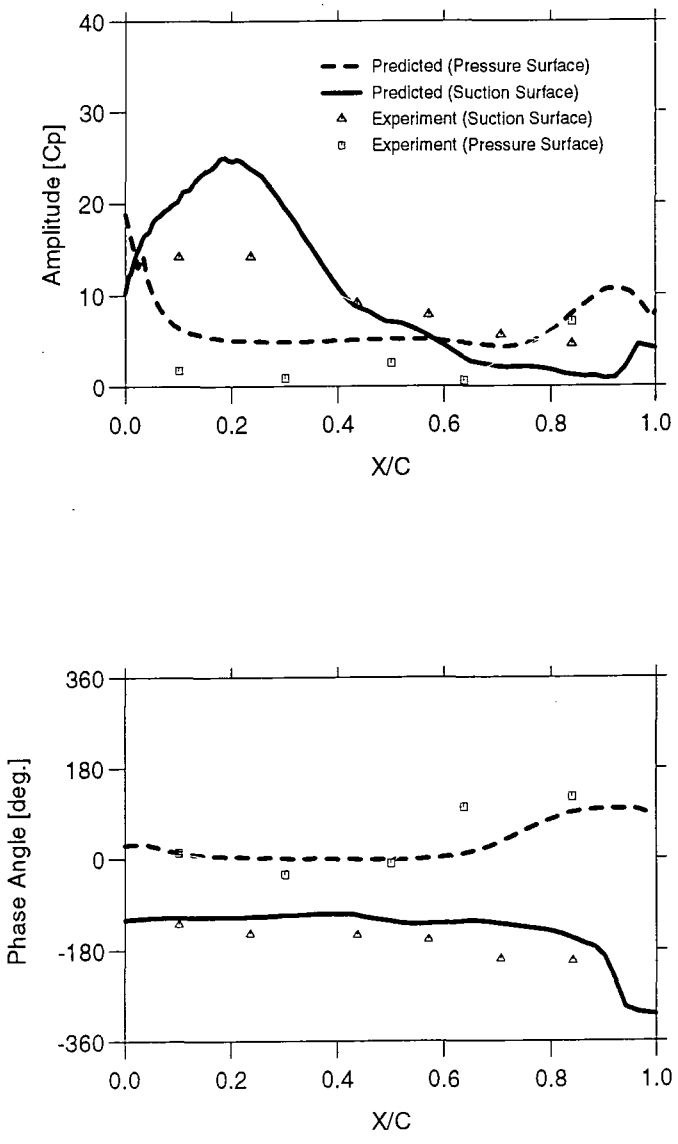

Fig. 3-12 Amplitude and Phase of Unsteady Pressure Coefficient Distribution for a Turbine Blade (IBPA = 90 deg.)

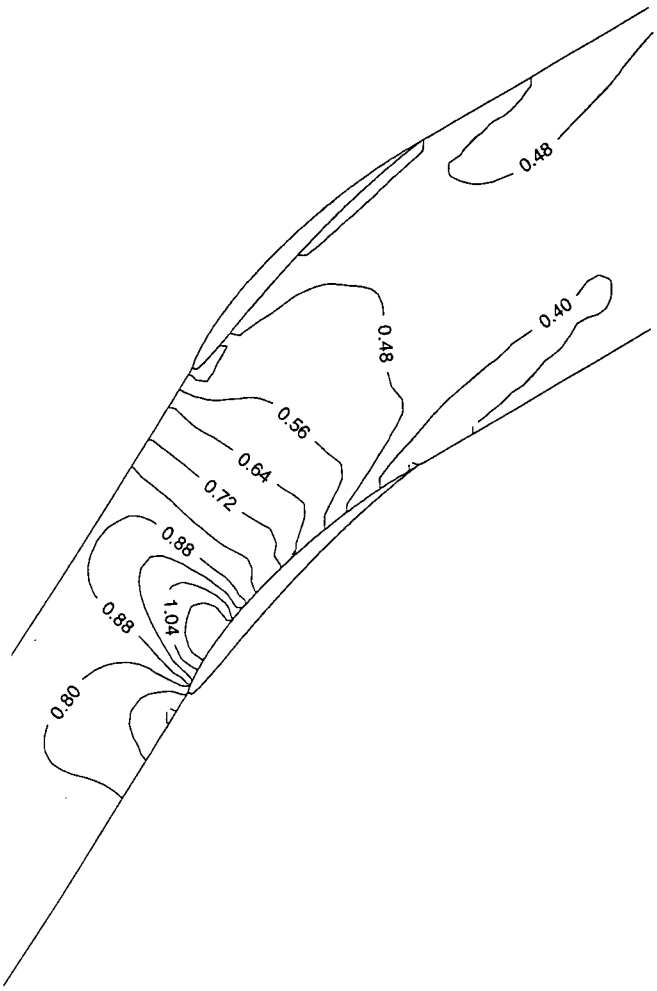

Fig. 3-13 Steady Mach Number Contour Map for a Compressor Cascade

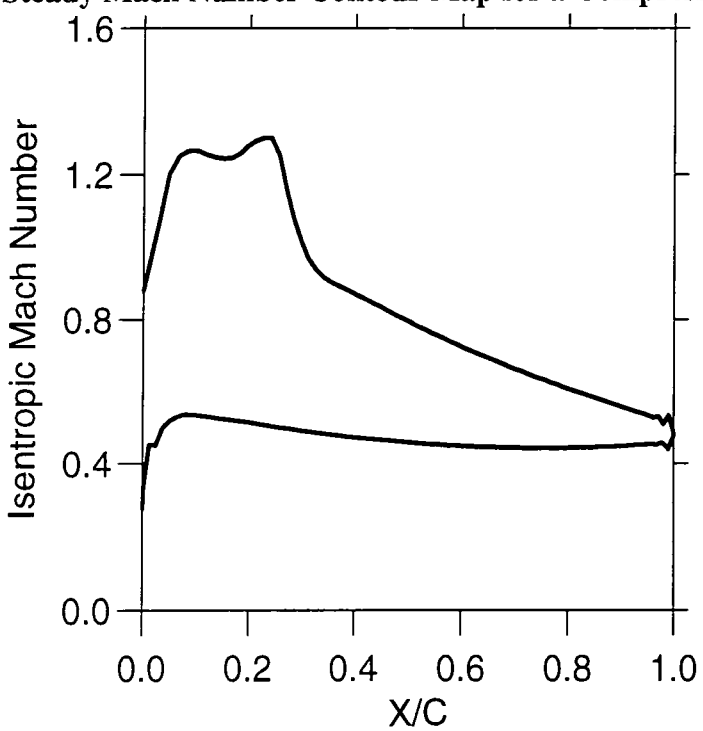

Fig. 3-14 Isentropic Mach Number Distribution on a Compressor Blade

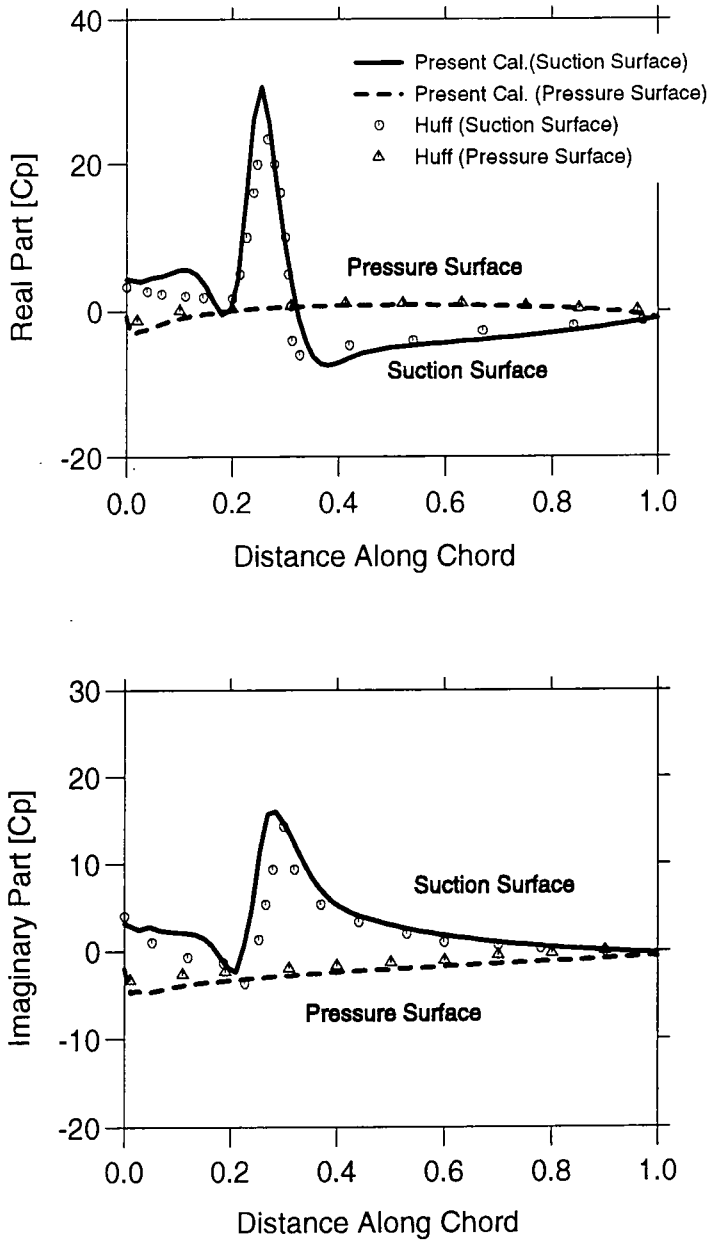

Fig. 3-15 Real and Imaginary Parts of Unsteady Pressure Coefficient Distribution on a Compressor Blade

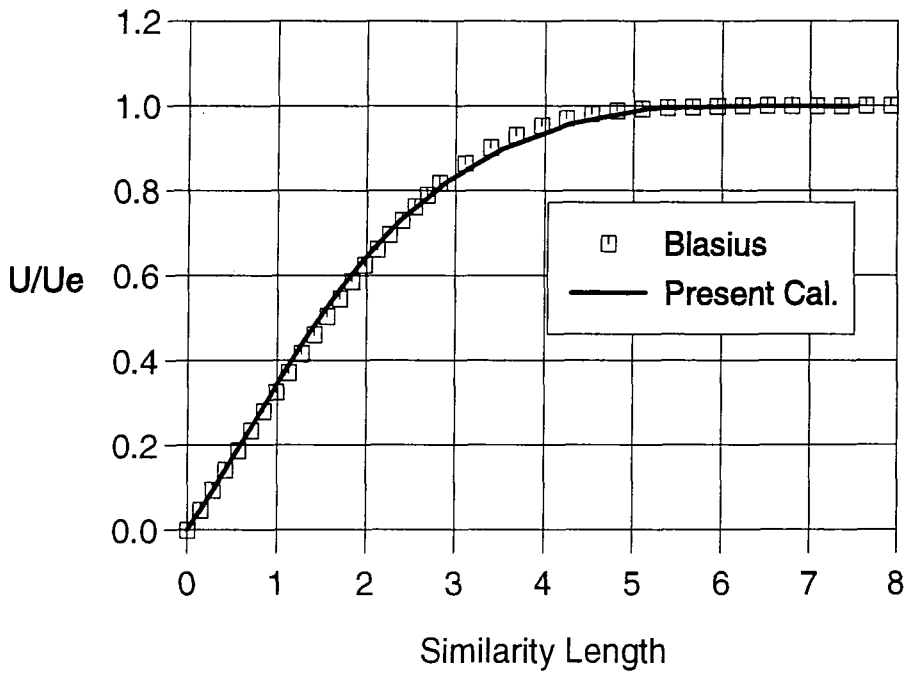

Fig. 3-16 Steady Velocity Profile in a Laminar Boundary Layer on Flat Plate

(a) $\omega x / U_0 = 0.5$

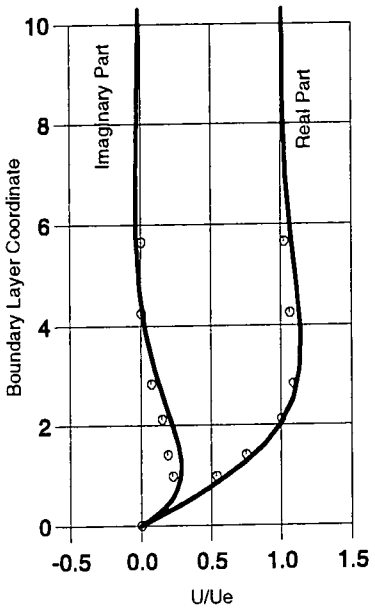

Ackerberg & Philips

Present Cal.

(b) $\omega x / U_0 = 1.5$

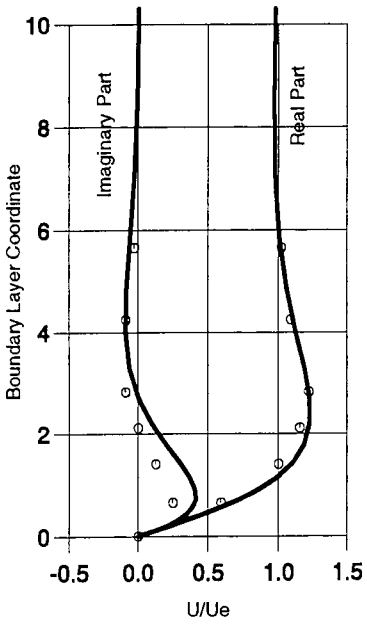

(c) $\omega x / U_0 = 2.5$

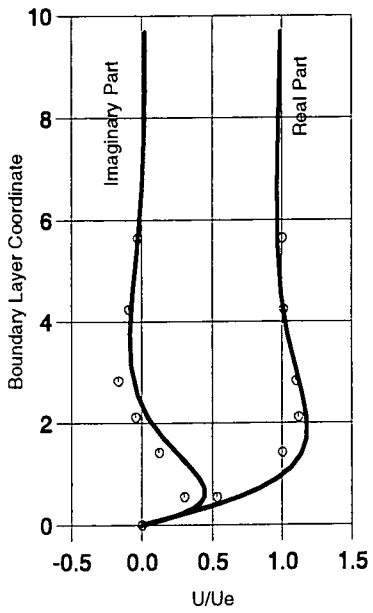

Fig. 3-17 Unsteady Velocity Profiles in a Laminar Boundary Layer on Flat Plate

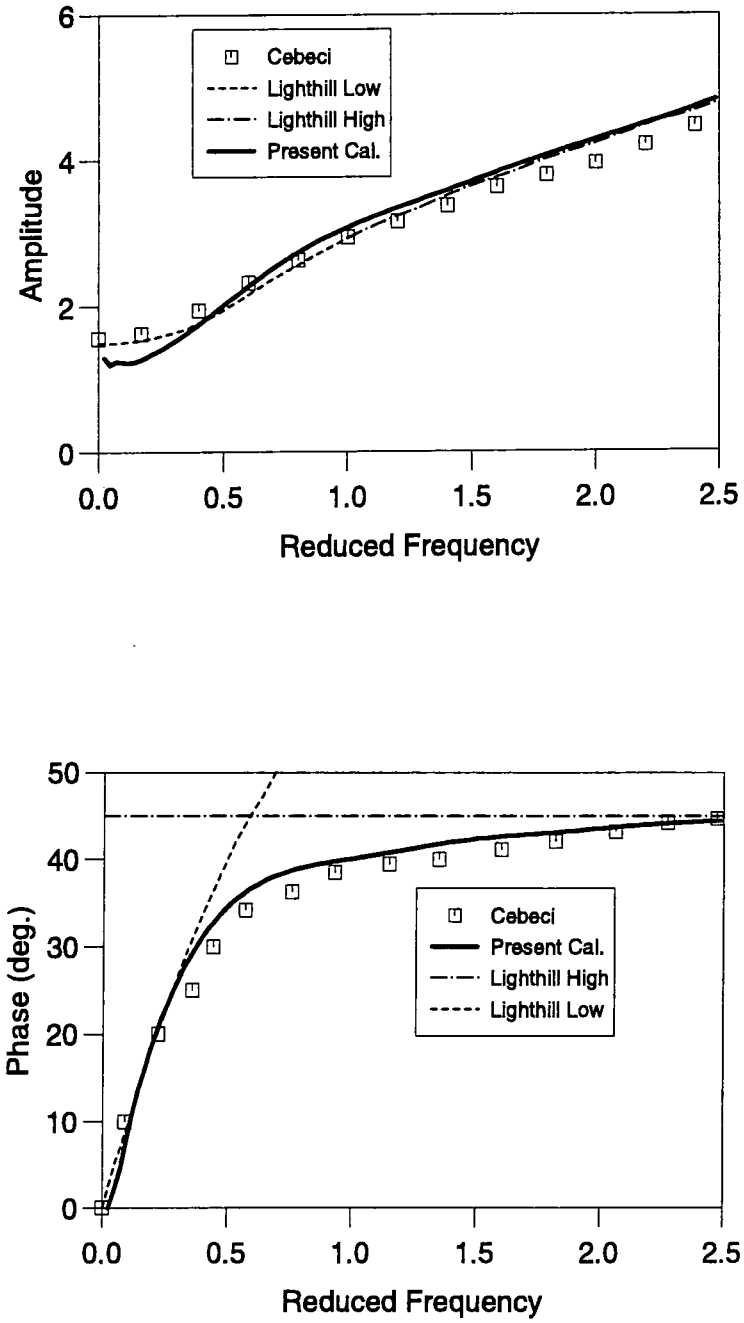

Fig. 3-18 Amplitude and Phase of Unsteady Shear Stress on Flat Plate

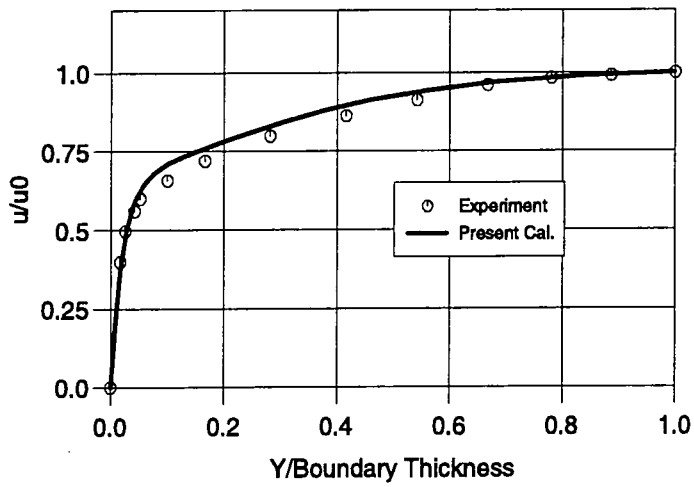

Fig. 3-19 Steady Velocity Profile in a Turbulent Boundary Layer on Flat Plate

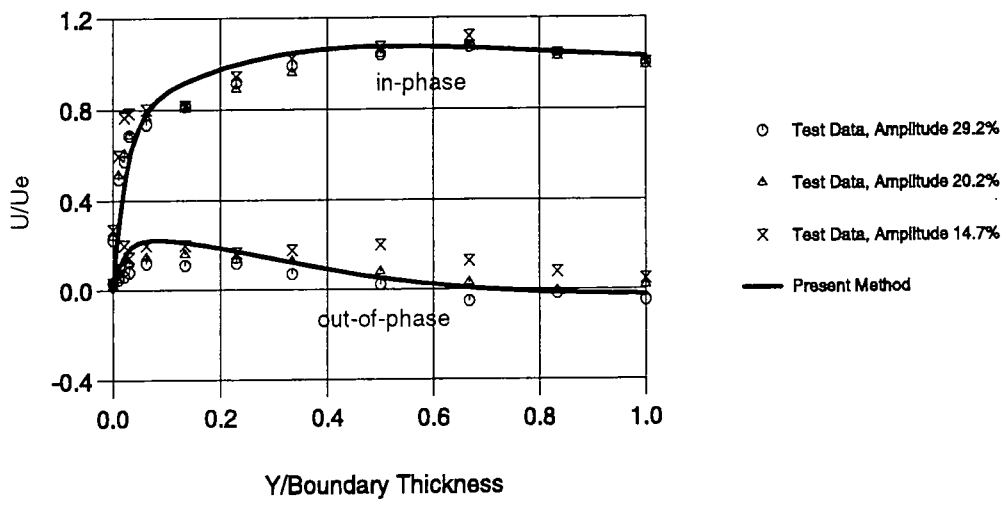

Fig. 3-20 Unsteady Velocity Profile in a Turbulent Boundary Layer on Flat Plate (f = 0.33 Hz)

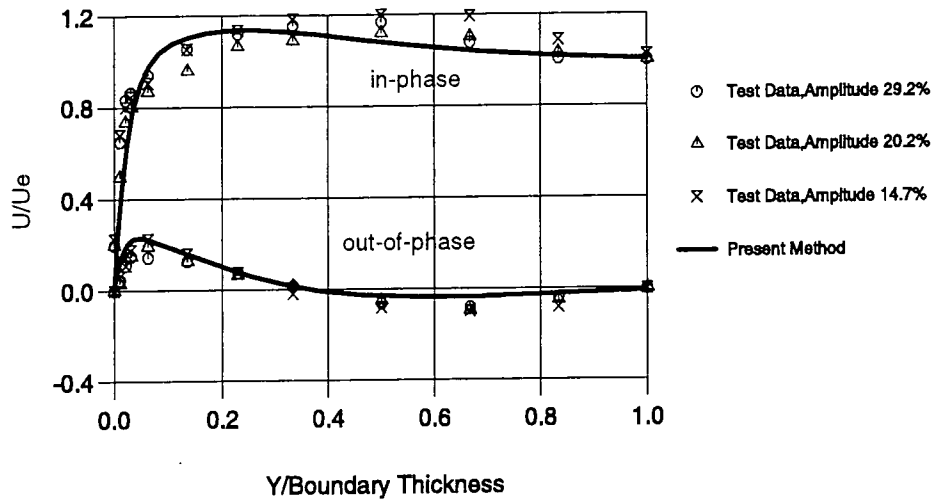

Fig. 3-21 Unsteady Velocity Profile in a Turbulent Boundary Layer on Flat Plate (f = 1.0 Hz)

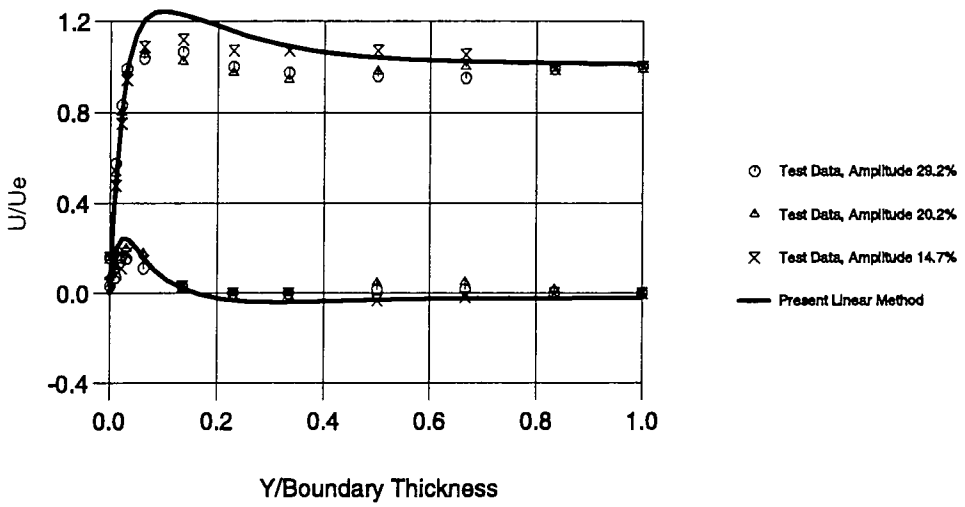

Fig. 3-22 Unsteady Velocity Profile in a Turbulent Boundary Layer on Flat Plate (f = 4.0 Hz)

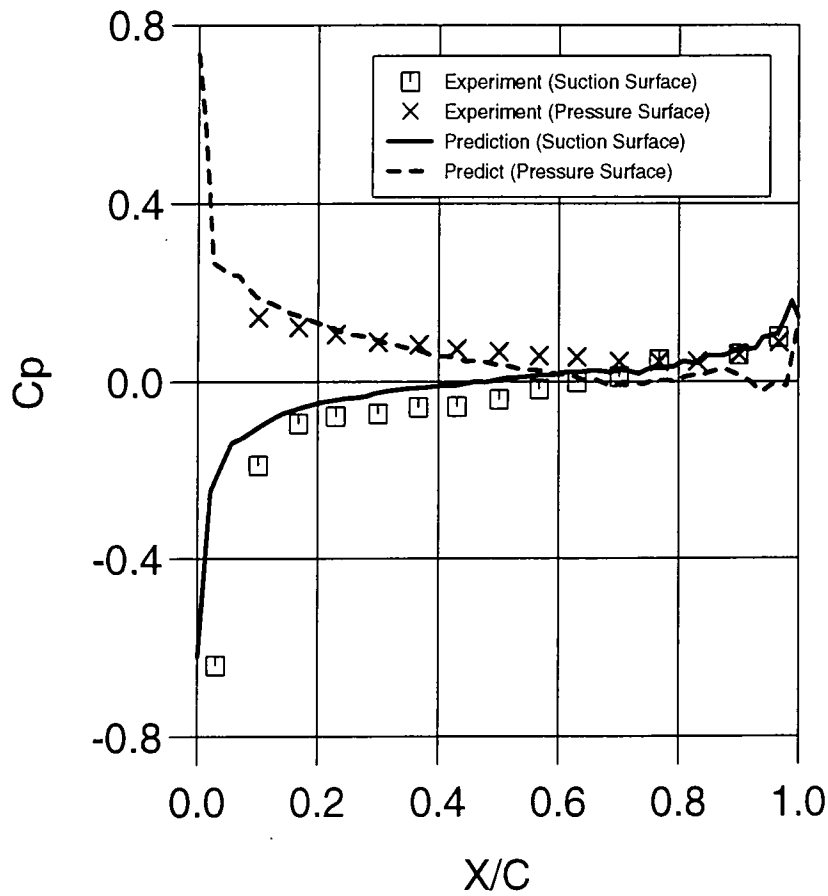

Fig. 3-23 Steady Pressure coefficient Distribution on a Compressor Blade

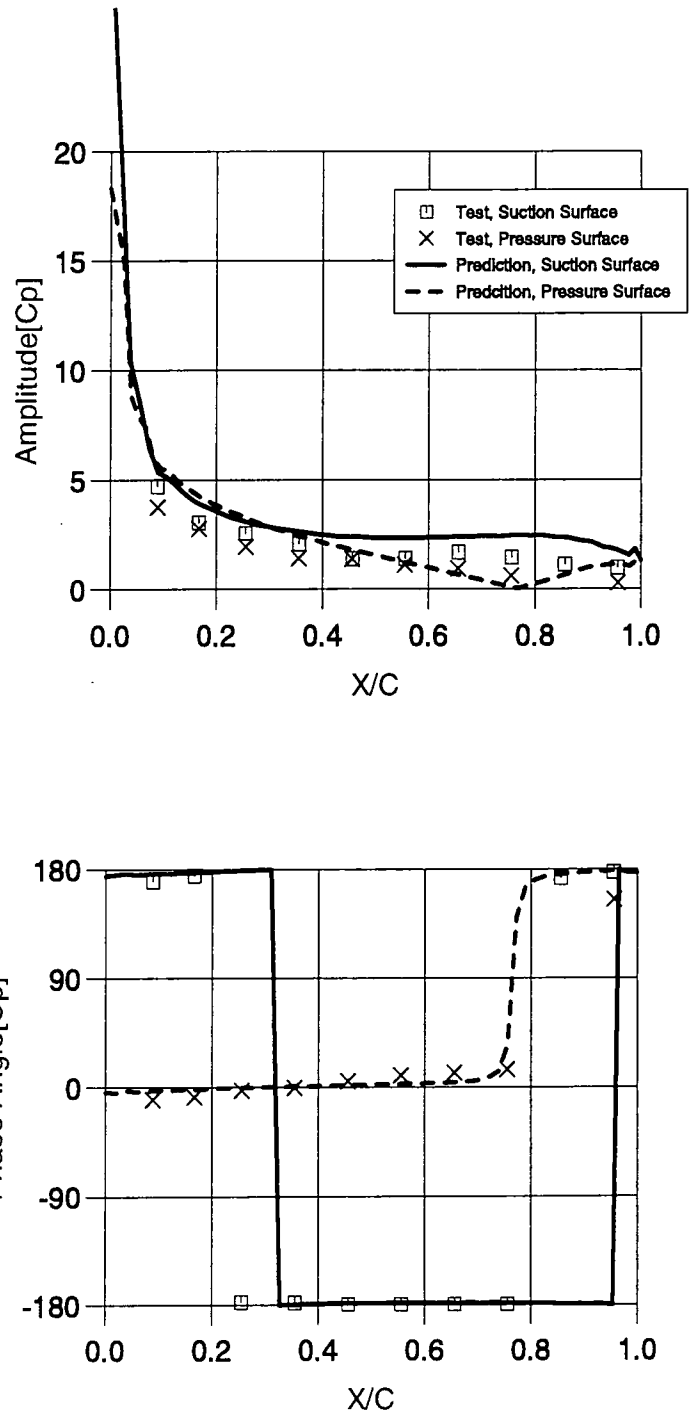

Fig. 3-24 Amplitude and Phase of Unsteady Pressure Coefficient Distribution on a Compressor Blade (k = 0.14)

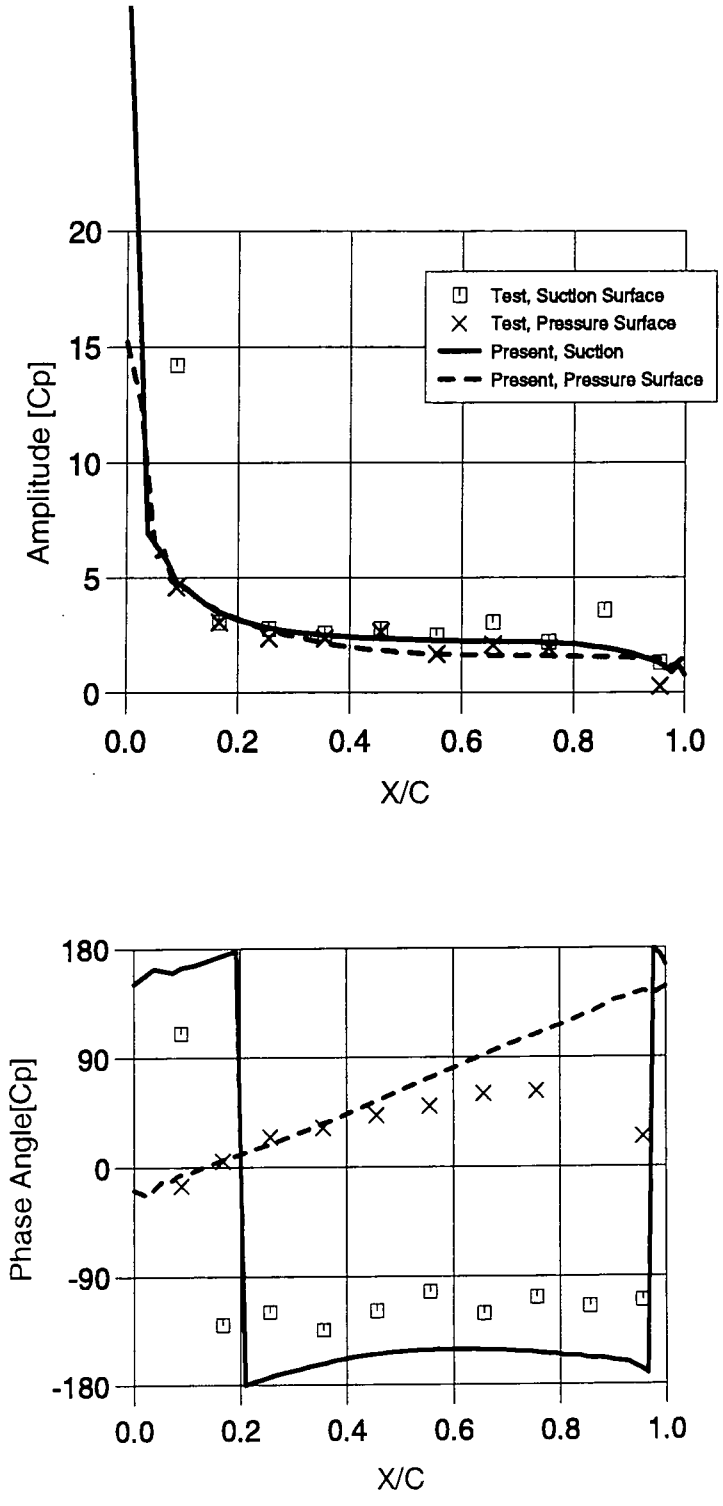

Fig. 3-25 Amplitude and Phase of Unsteady Pressure Coefficient Distribution on a Compressor Blade (k = 1.02)

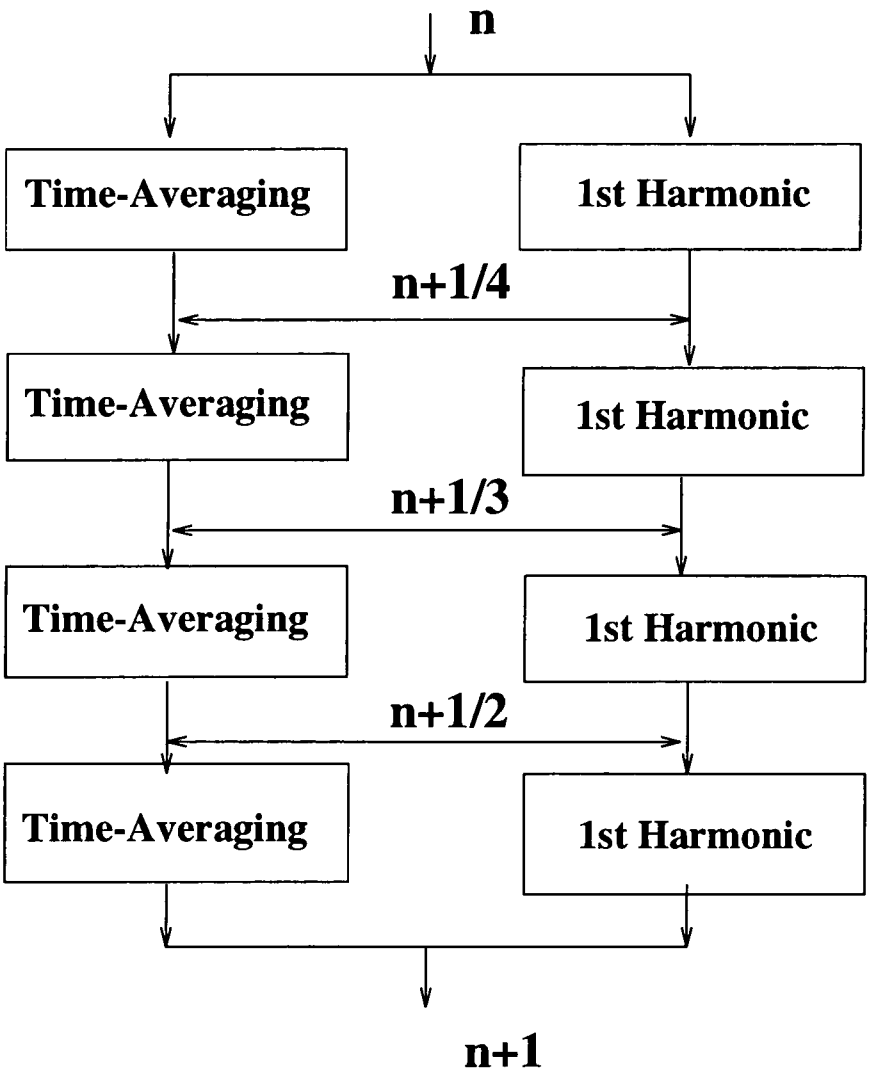

Fig. 4-1 A Strong Coupling Procedure for Nonlinear Harmonic Method in the 4-Stage Runge Kutta Scheme

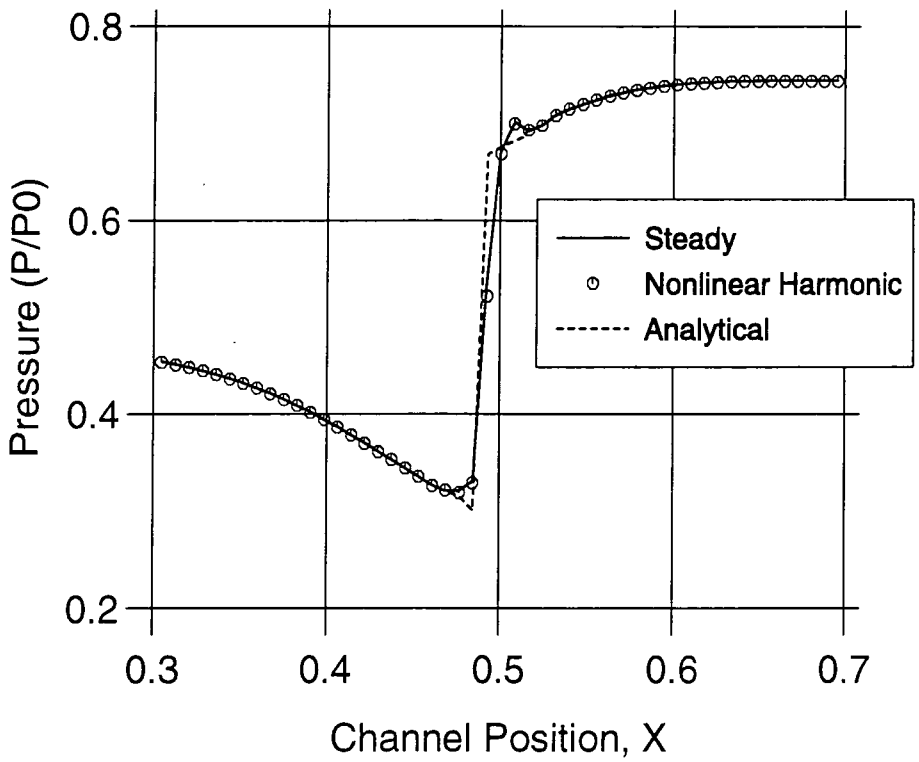

Fig. 5-1 Steady and Time-averaged Static Pressure Distribution in Diverging Channel (Back Pressure Variation Amplitude : 1%)

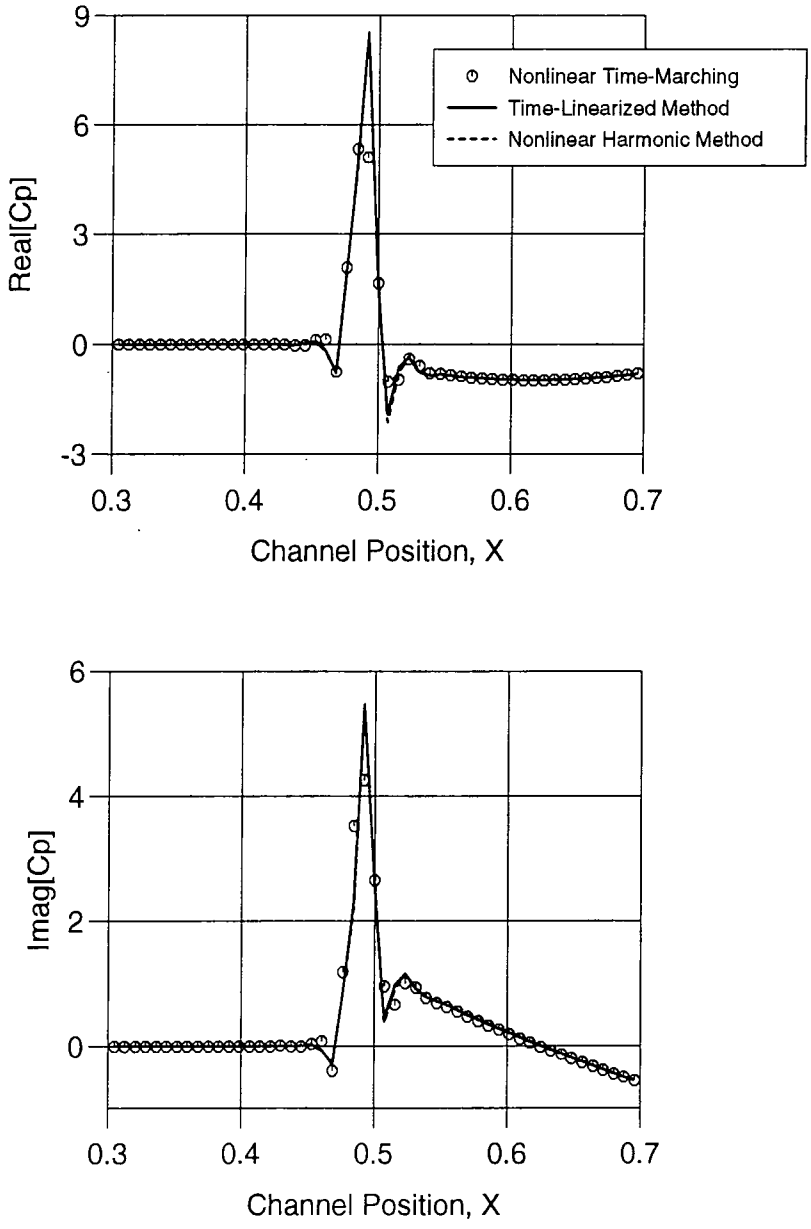

Fig. 5-2 Real and Imaginary Parts of Unsteady Pressure Coefficients in Diverging Channel (Back Pressure Variation Amplitude : 1%)

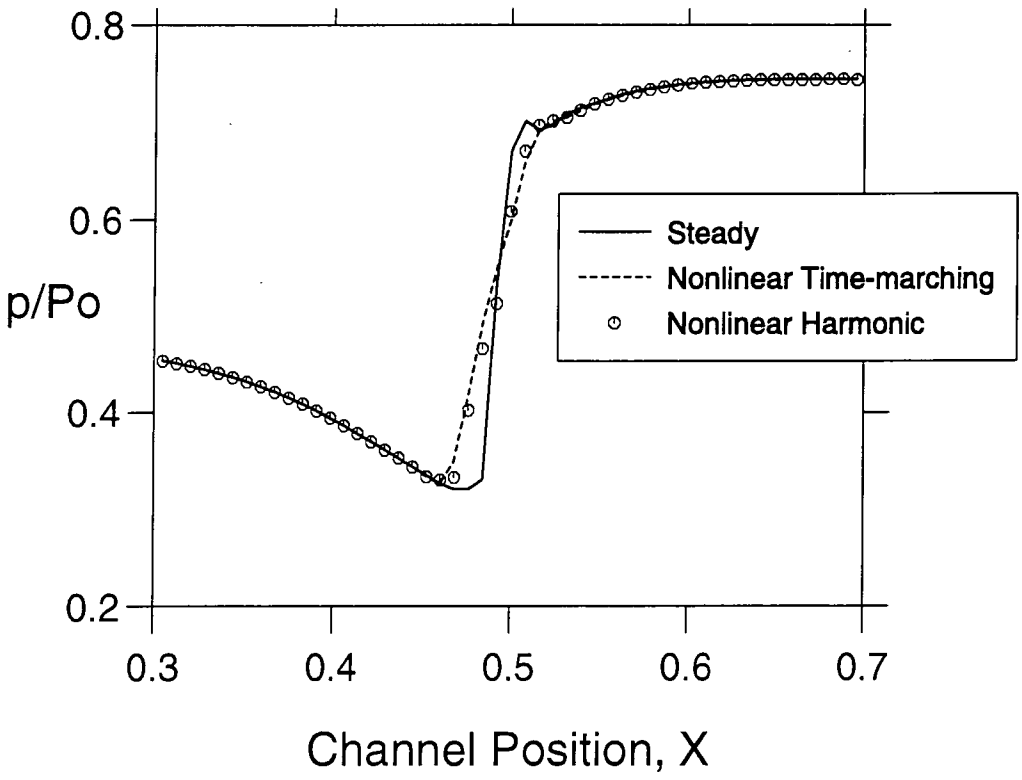

Fig. 5-3 Steady and Time-averaged Static Pressure Distribution in Diverging Channel (Back Pressure Variation Amplitude : 7%)

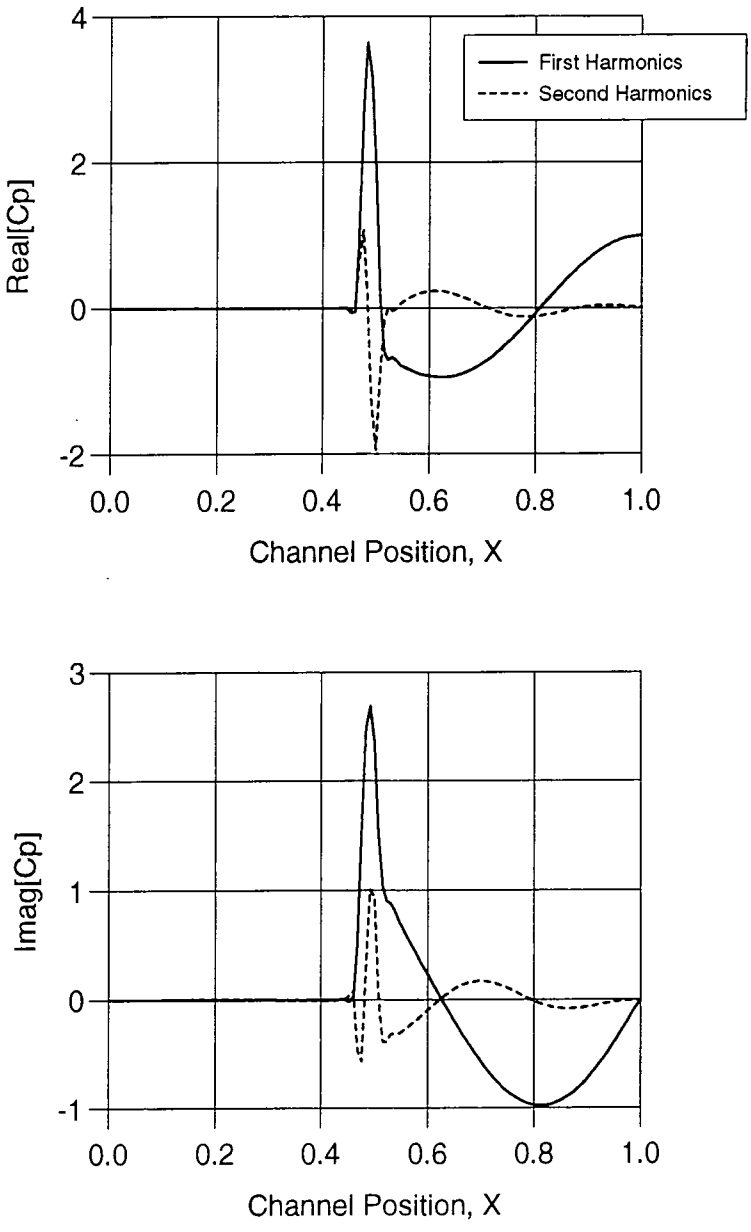

Fig. 5-4 First and Second Harmonics of Unsteady Pressure Coefficients in a Diverging Channel (Back Pressure Variation Amplitude: 7%)

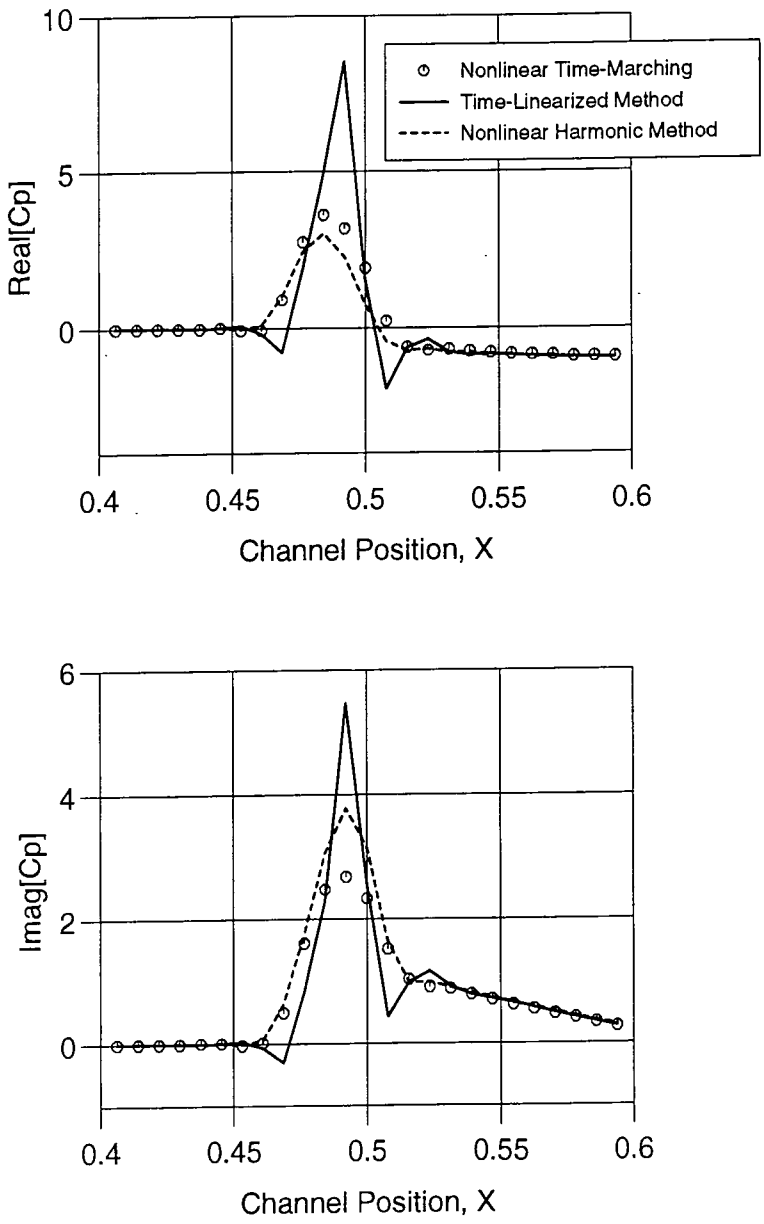

Fig. 5-5 Real and Imaginary Parts of Unsteady Pressure Coefficients in Diverging Channel (Back Pressure Variation Amplitude : 7%)

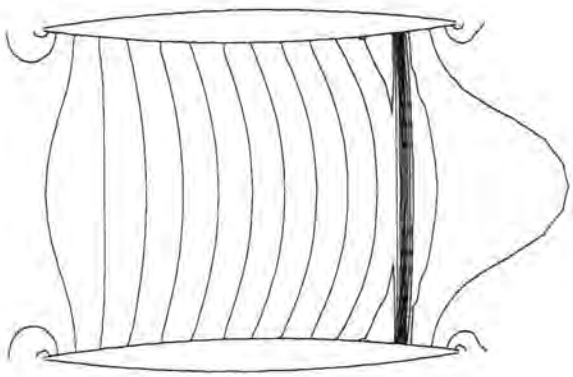

Fig. 5-6 Steady Mach Number Contour Map in Biconvex Cascade (Pressure Ratio: 0.7)

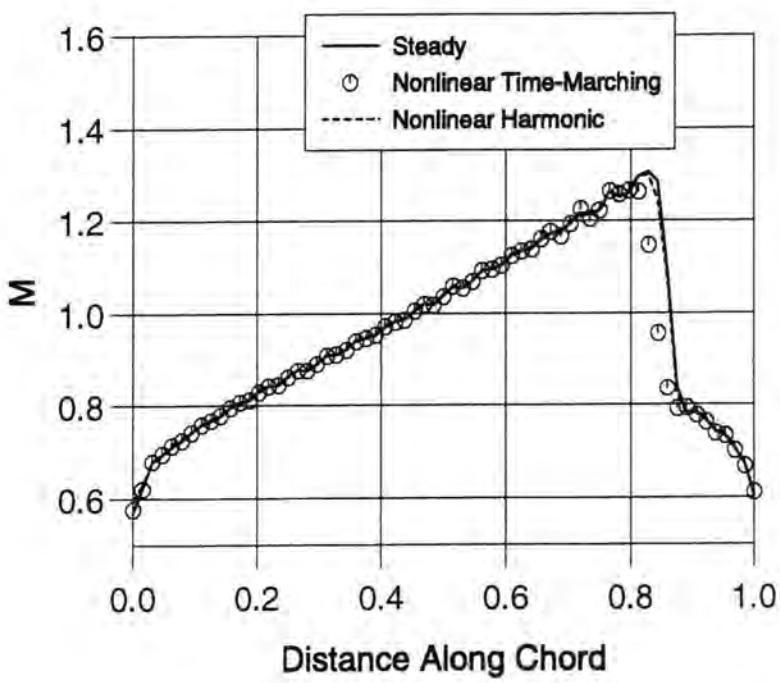

Fig. 5-7 Steady and Time-averaged Mach Number Distribution on Biconvex Blade (Pressure Ratio: 0.7)

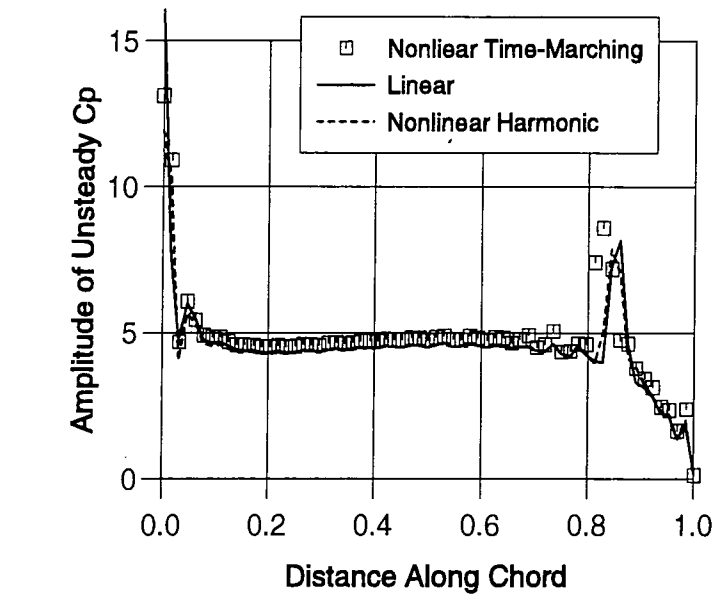

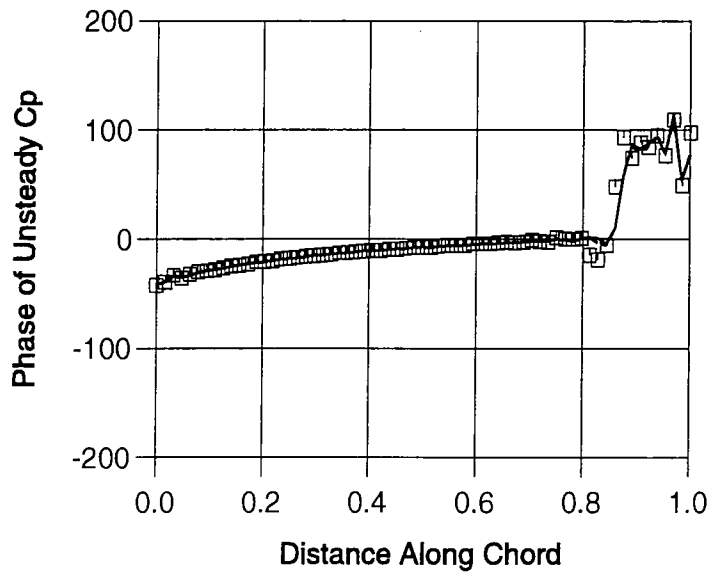

Fig. 5-8 Amplitude and Phase of Unsteady Pressure Coefficients on Biconvex Blade (Pressure Ratio: 0.7)

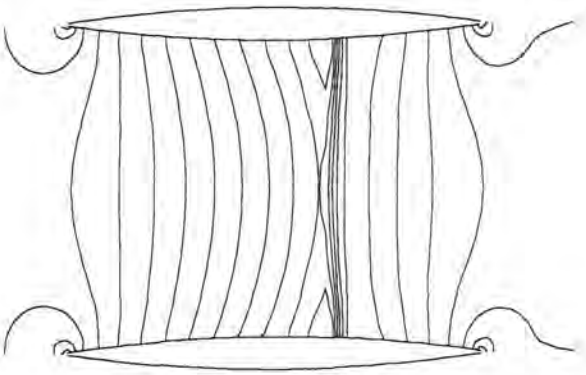

Fig. 5-9 Steady Mach Number Contour Map in Biconvex Cascade (Pressure Ratio: 0.725, Torsion Amplitude: 0.75 deg.)

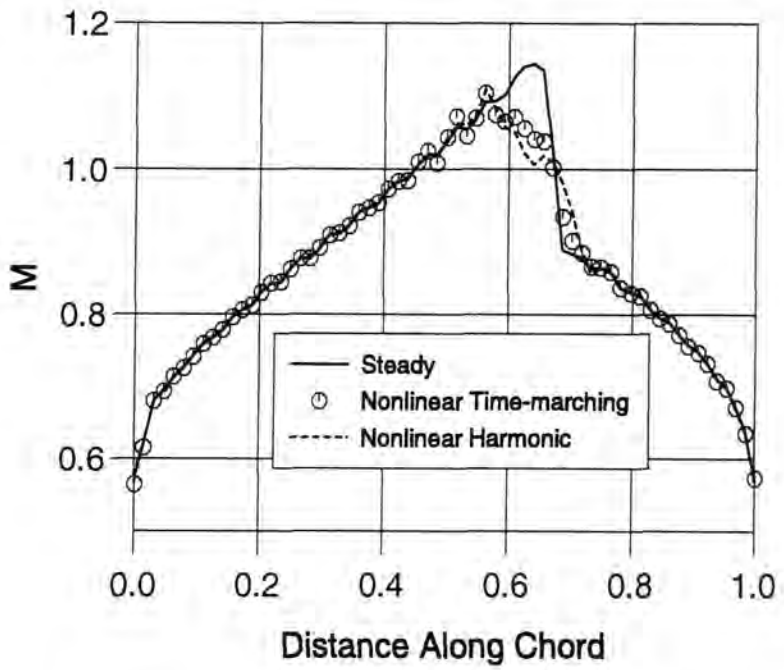

Fig. 5-10 Steady and Time-averaged Mach Number Distribution on Biconvex Blade (Pressure Ratio: 0.725, Torsion Amplitude: 0.75 deg.)

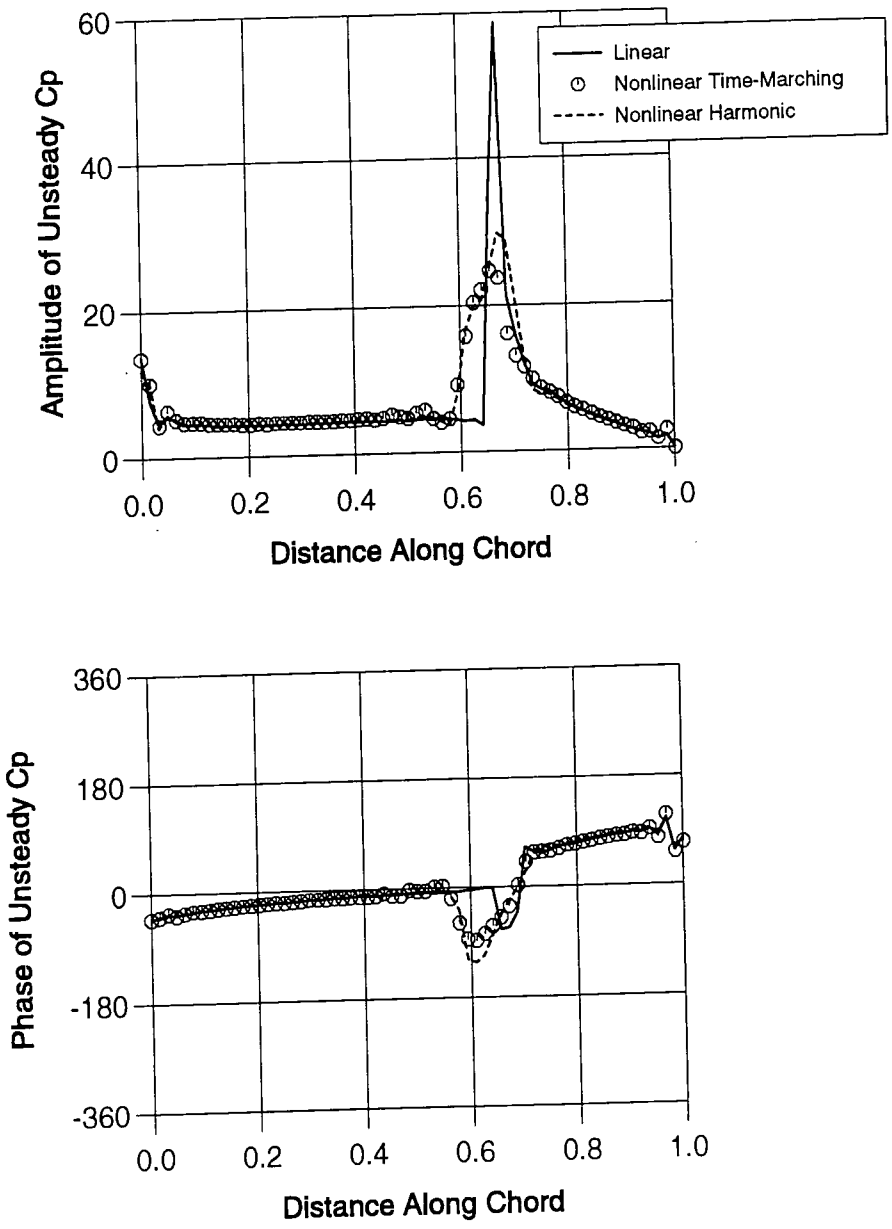

Fig. 5-11 Amplitude and Phase of Unsteady Pressure Coefficients on Biconvex Blade (Pressure Ratio: 0.725, Torsion Amplitude: 0.75 deg.)

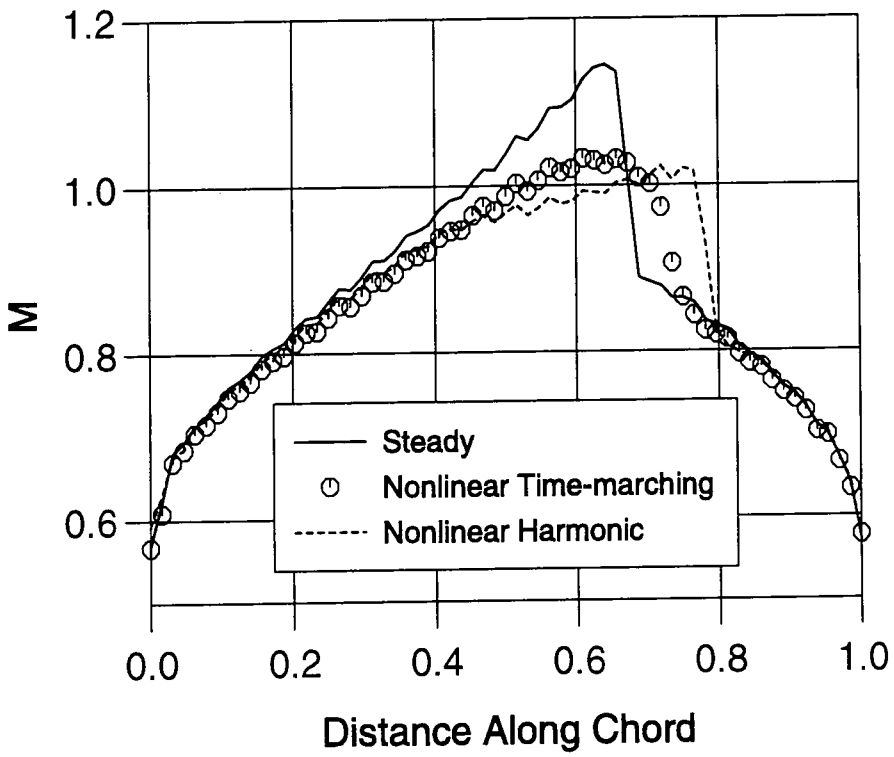

Fig. 5-12 Steady and Time-averaged Mach Number Distribution on Biconvex Blade (Pressure Ratio: 0.725, Torsion Amplitude: 2 deg.)

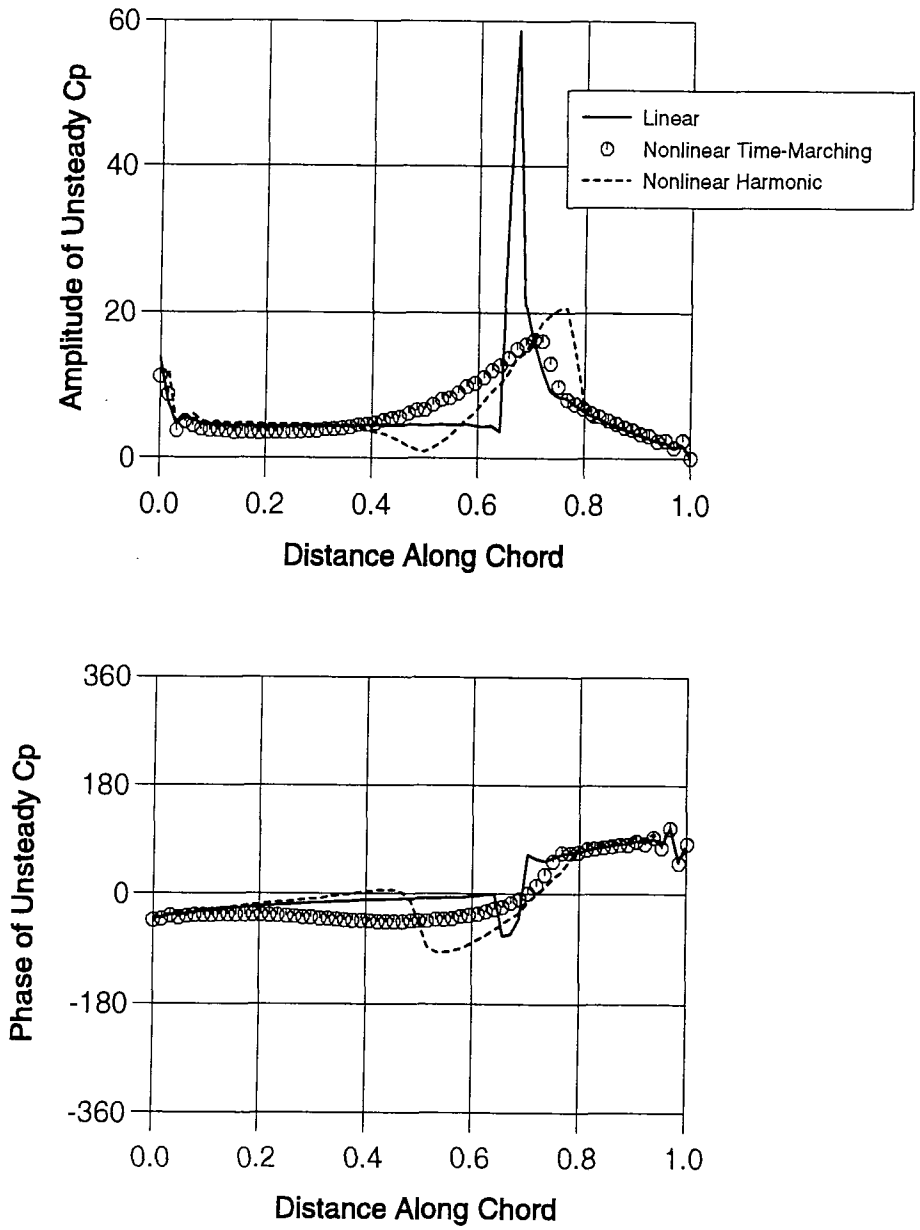

Fig. 5-13 Amplitude and Phase of Unsteady Pressure Coefficients on Biconvex Blade (Pressure Ratio: 0.725, Torsion Amplitude: 2 deg.)

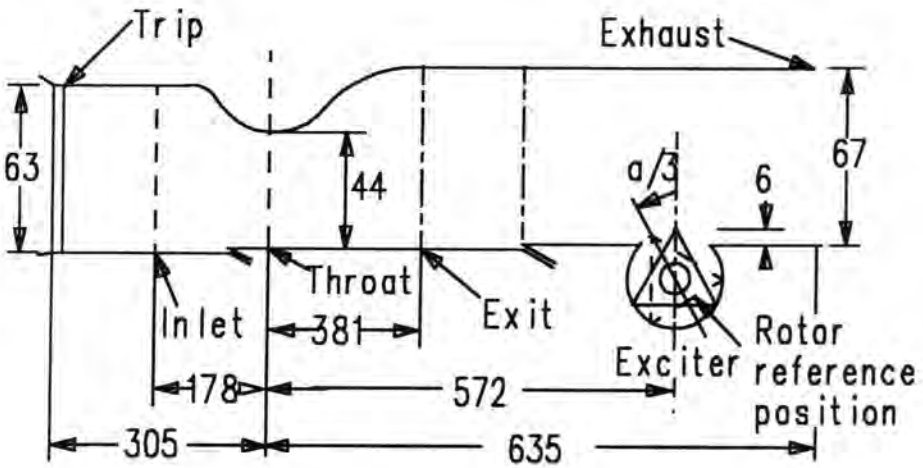

Fig. 5-14 Schematic of diffuser model

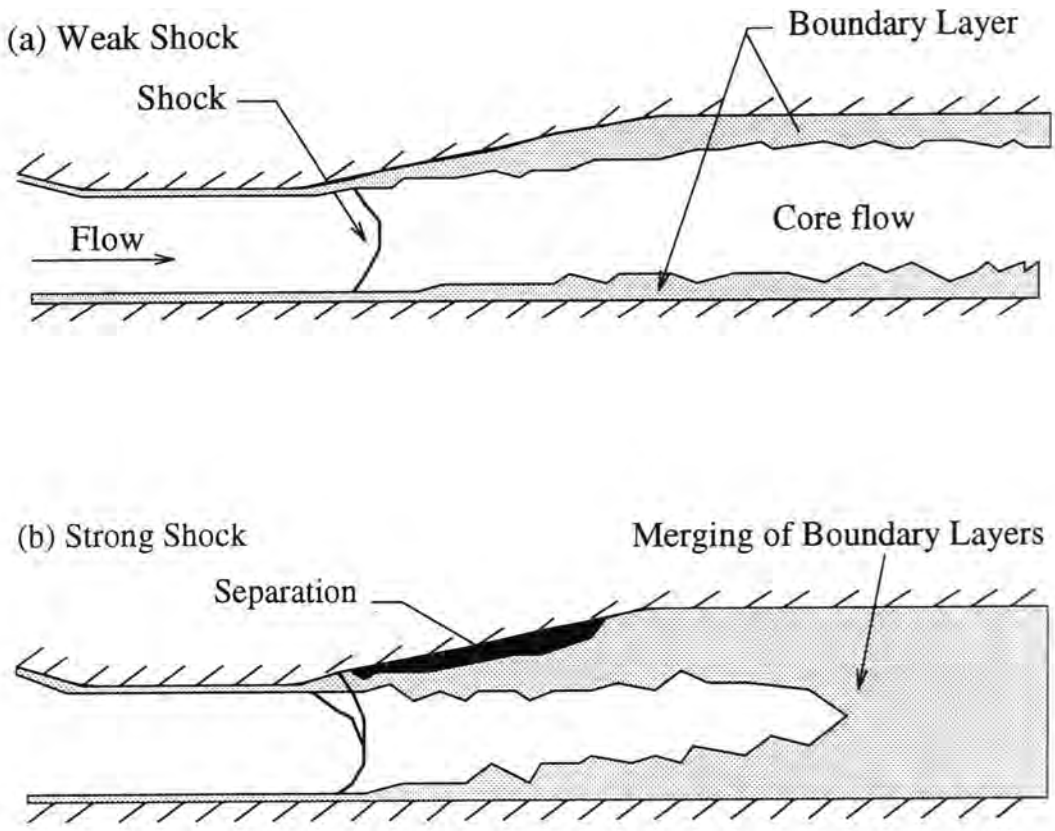

Fig. 5-15 Flow patters observed in diffuser flows

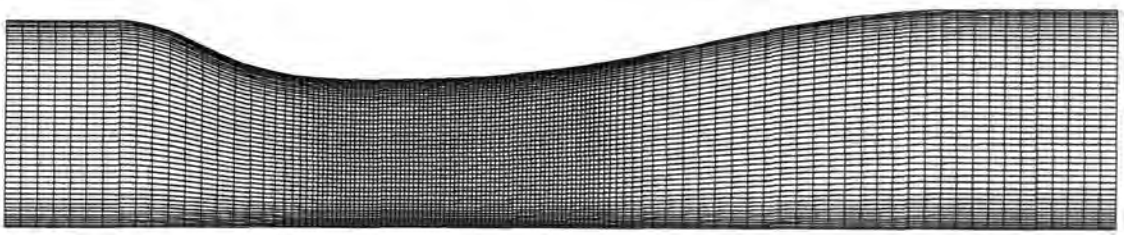

Fig. 5-16 Computational Mesh for Transonic Diffuser
(vertical scale enlarged by a factor of 2)

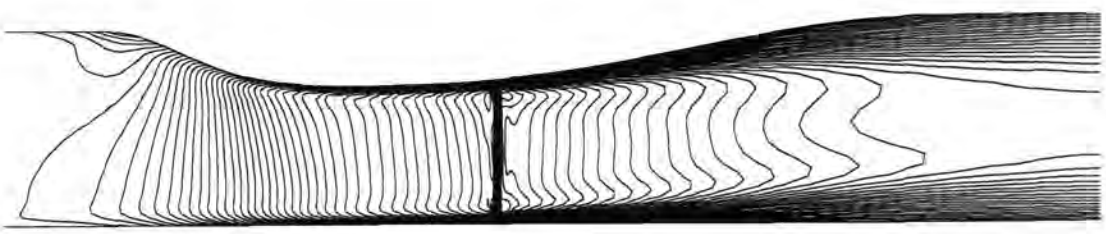

Fig. 5-17 Steady Mach Number Contours in Transonic Diffuser
(vertical scale enlarged by a factor of 2)

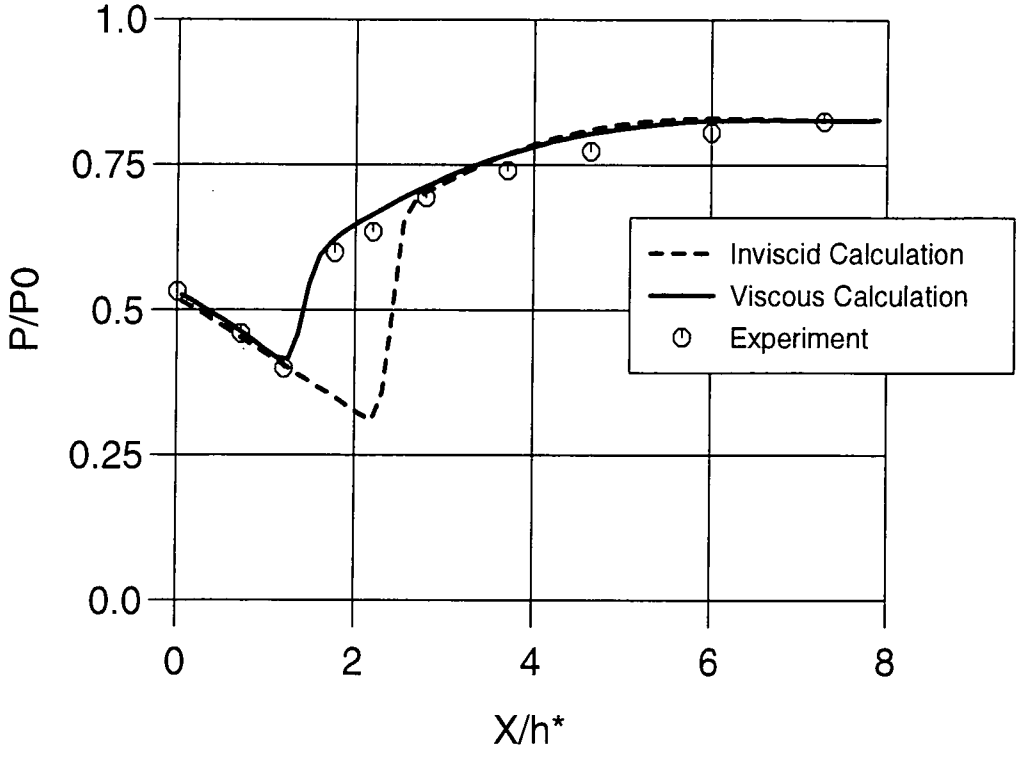

Fig. 5-18 Steady Static Pressure Distribution on Top Wall of Transonic Diffuser

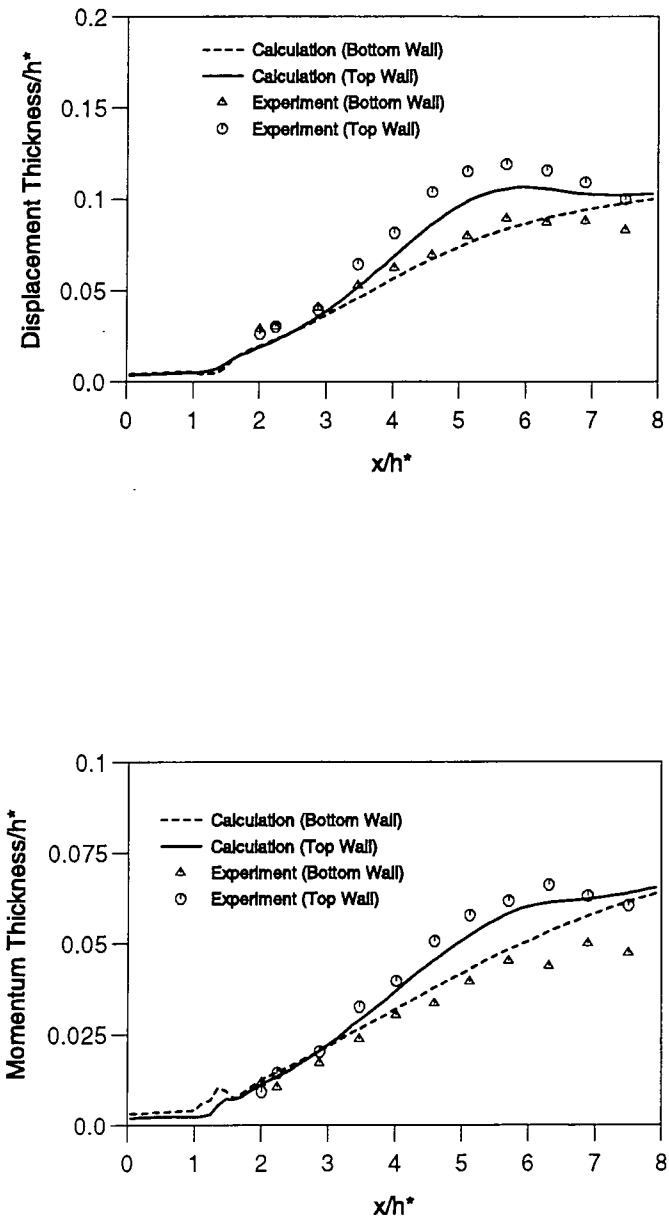

Fig. 5-19 Steady Boundary Layer Displacement Thickness and Momentum Thickness Distributions on Top Wall of Transonic Diffuser

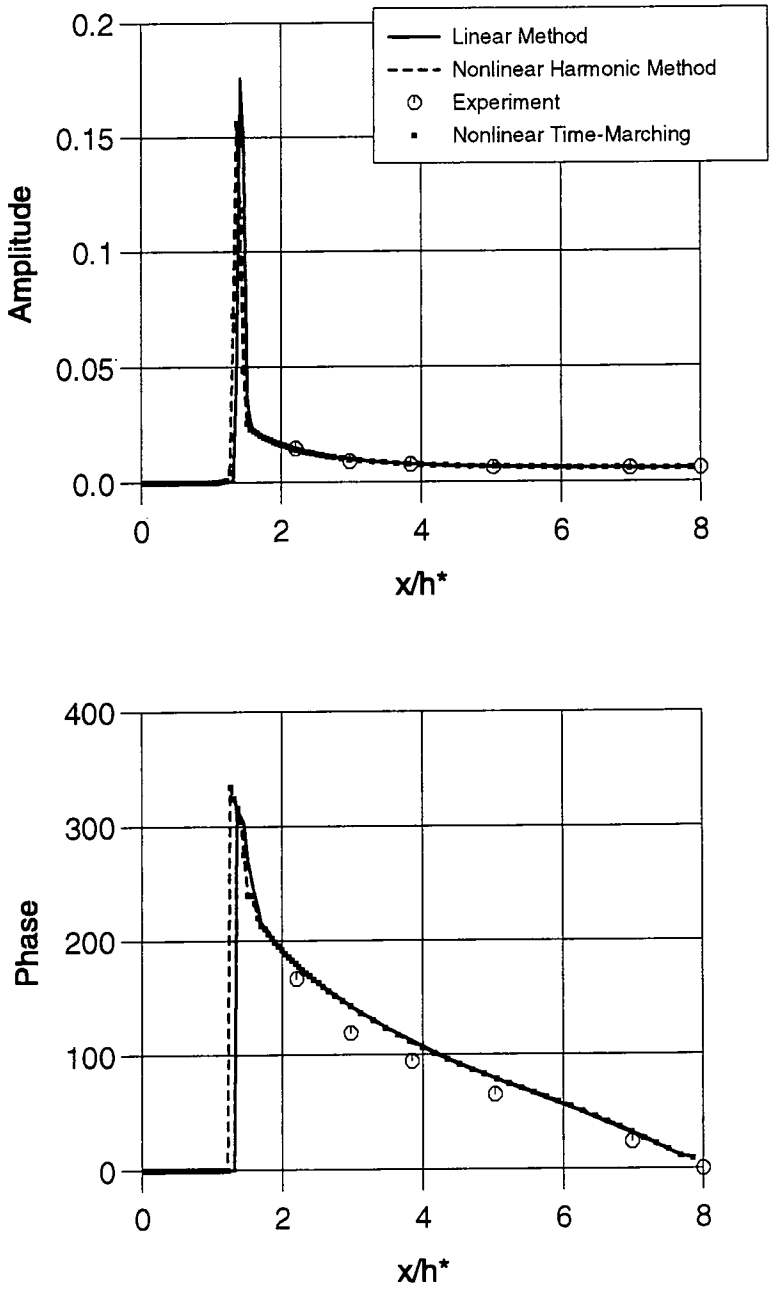

Fig. 5-20 Amplitude and Phase of Unsteady Pressure Coefficients on Top Wall of Transonic Diffuser (f = 300 Hz, Amplitude: 0.0085)

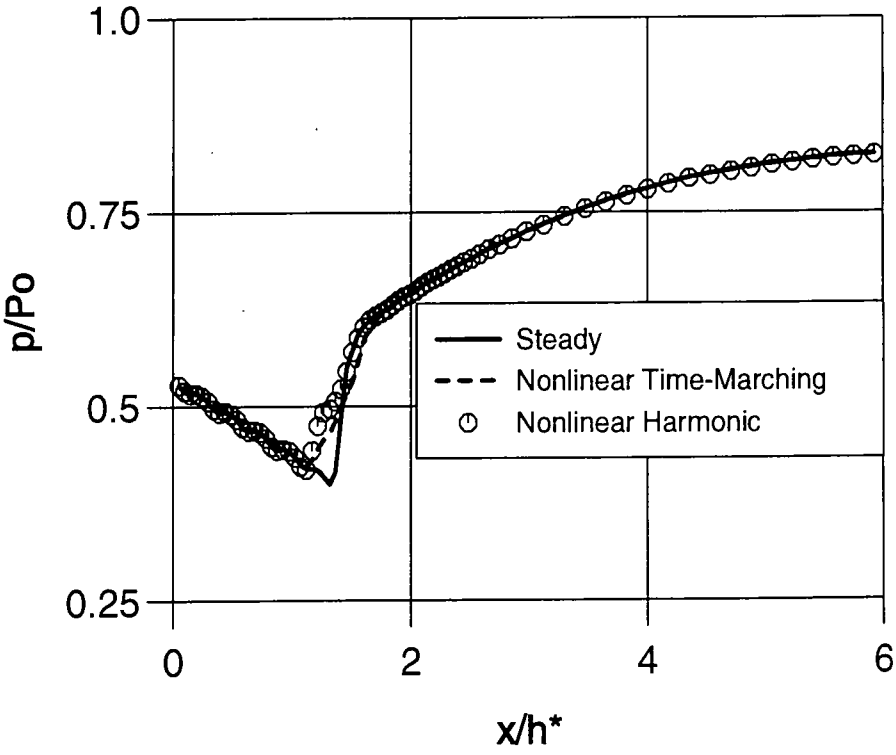

Fig. 5-21 Steady and Time-averaged Pressure Distribution on Top Wall of Transonic Diffuser (f = 150 Hz, Amplitude: 0.011)

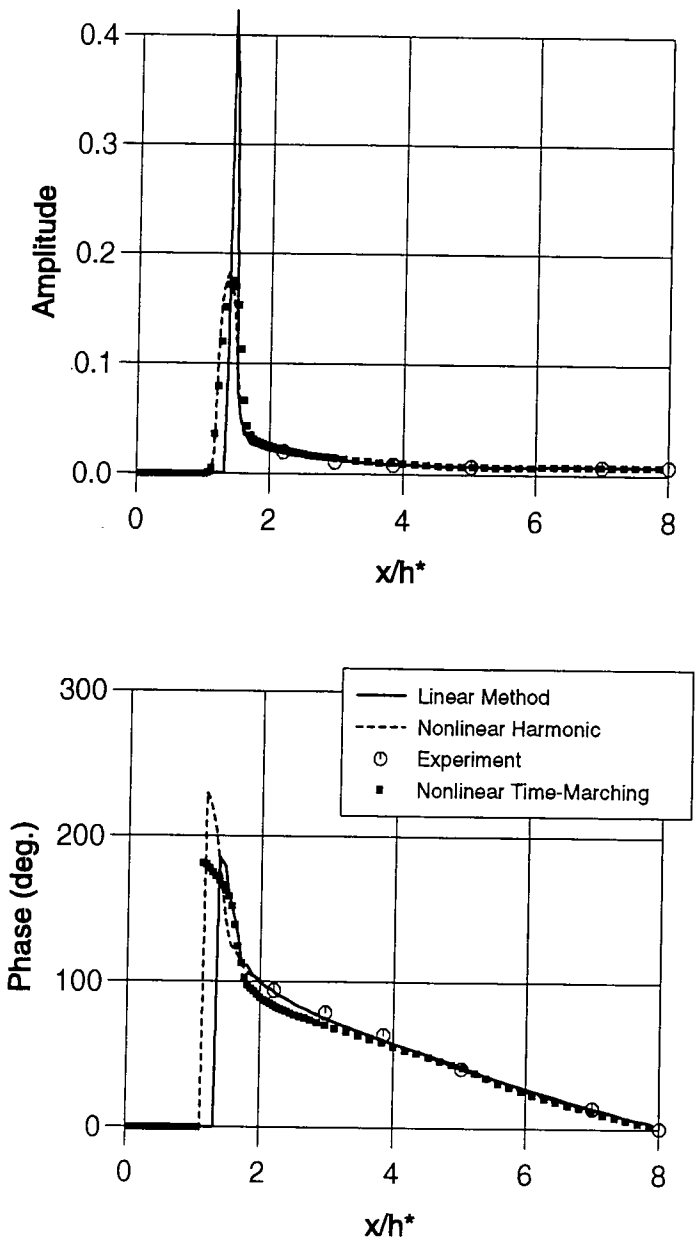

Fig. 5-22 Amplitude and Phase of Unsteady Pressure Coefficients on Top Wall of Transonic Diffuser (f = 150 Hz, Amplitude: 0.011)

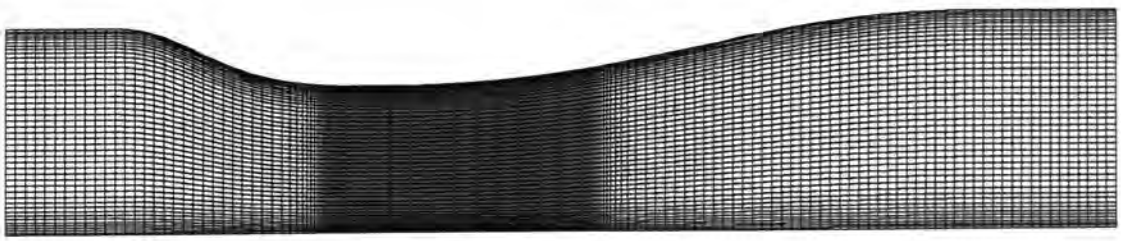

Fig. 5-23 Finer Computational Mesh for Transonic Diffuser (vertical scale enlarged by a factor of 2)

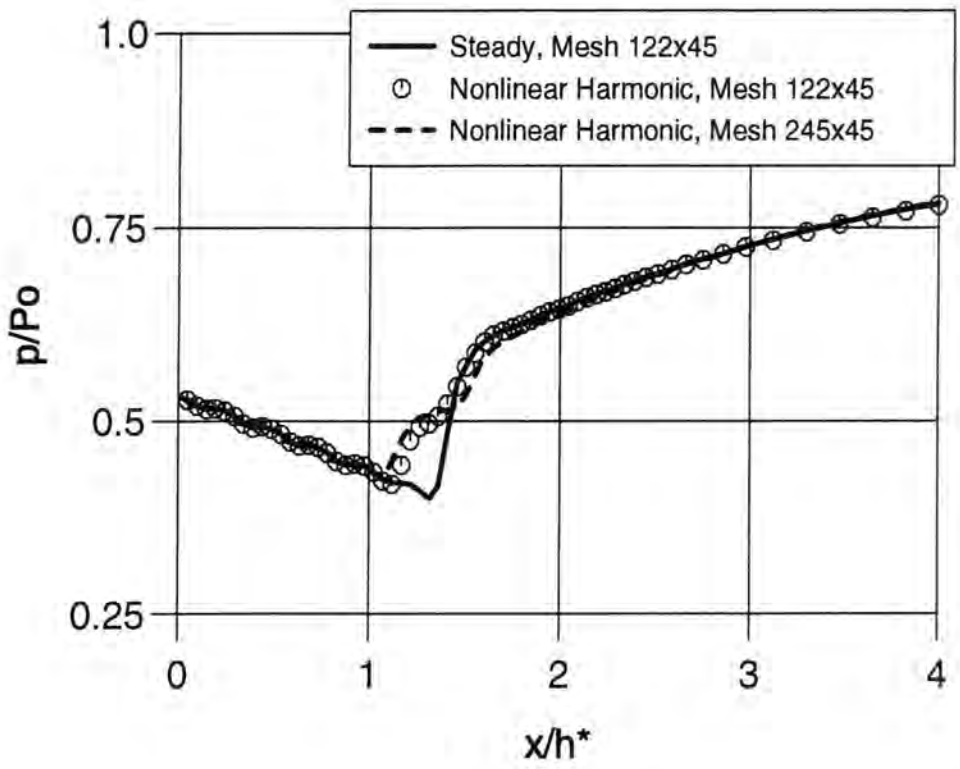

Fig. 5-24 Steady and Time-averaged Pressure Distribution on Top Wall of Diffuser with Different Meshes (f = 150Hz, Amplitude: 0.011)

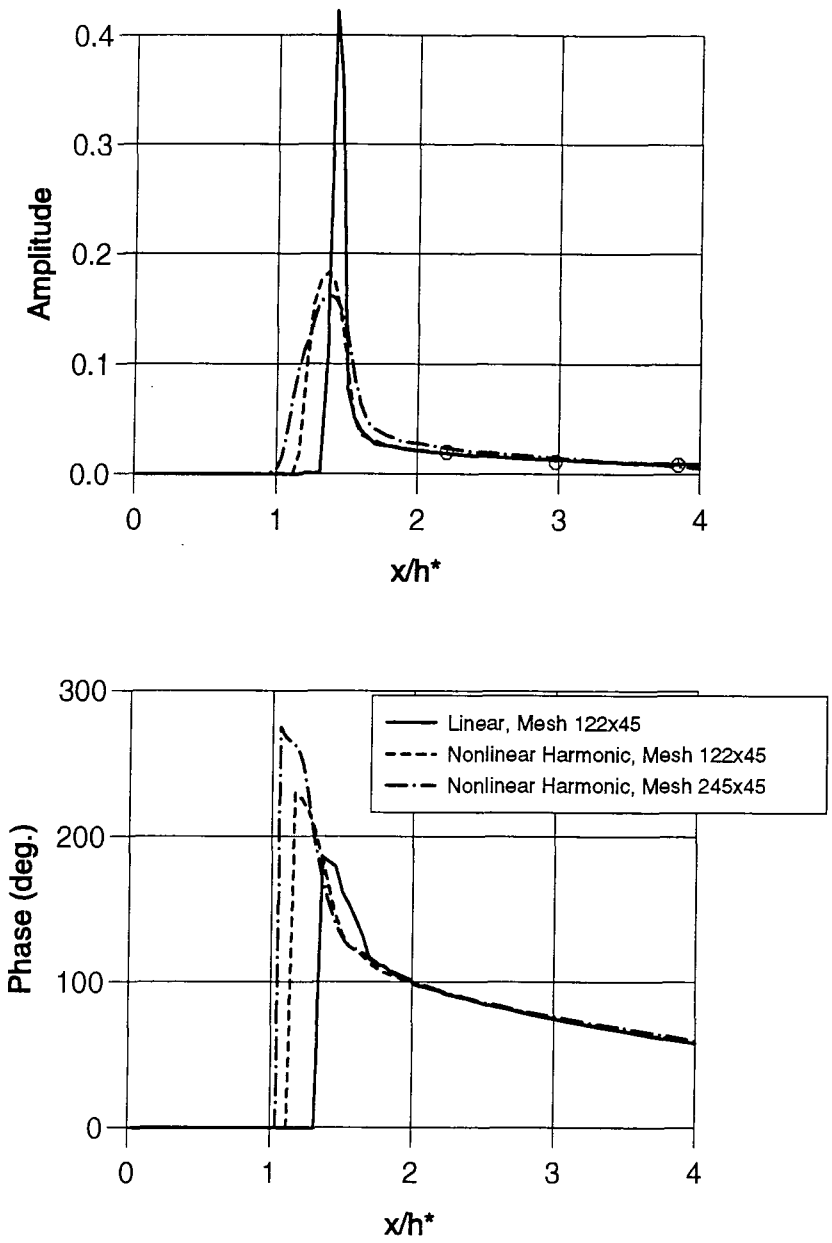

Fig. 5-25 Amplitude and Phase of Unsteady Pressure Coefficients on Top Wall of Transonic Diffuser with Different Meshes (f = 150 Hz, Amplitude: 0.011)

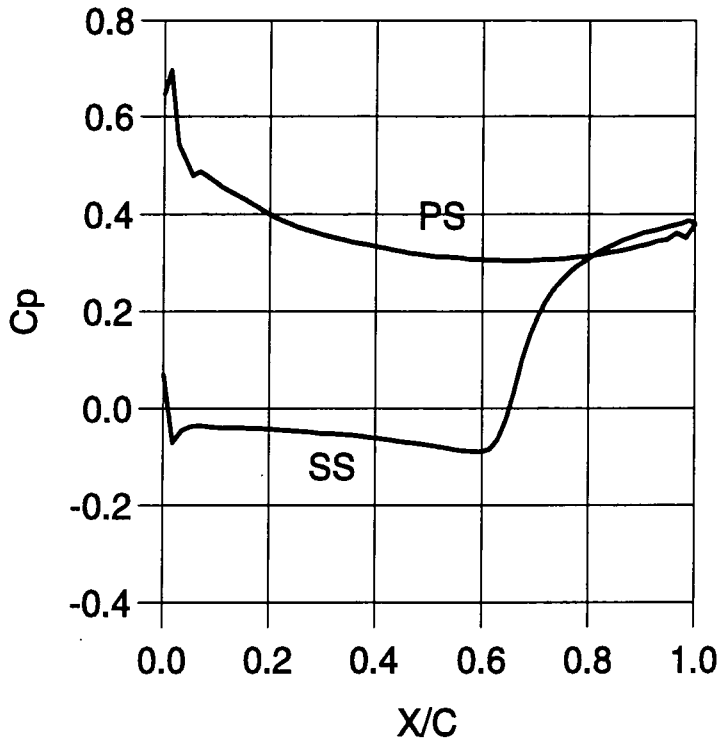

Fig. 5-26 Steady Pressure Coefficient Distribution on a Compressor Blade

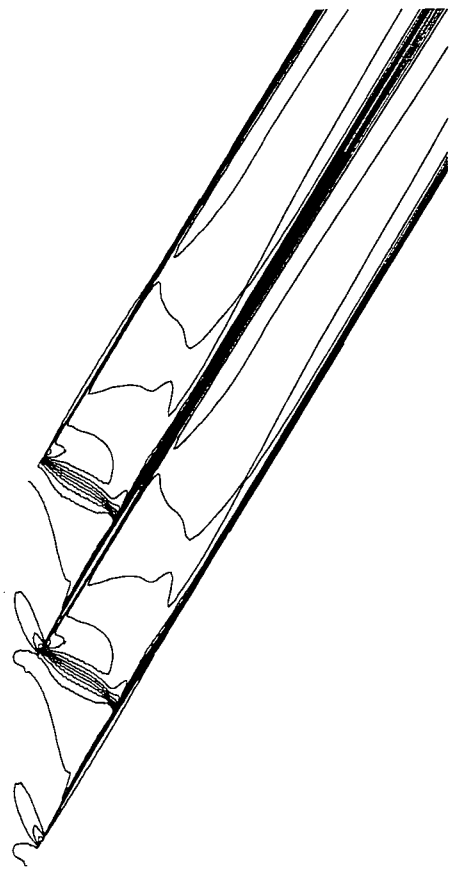

Fig. 5-27 Steady Mach Number Contours in a Compressor Cascade

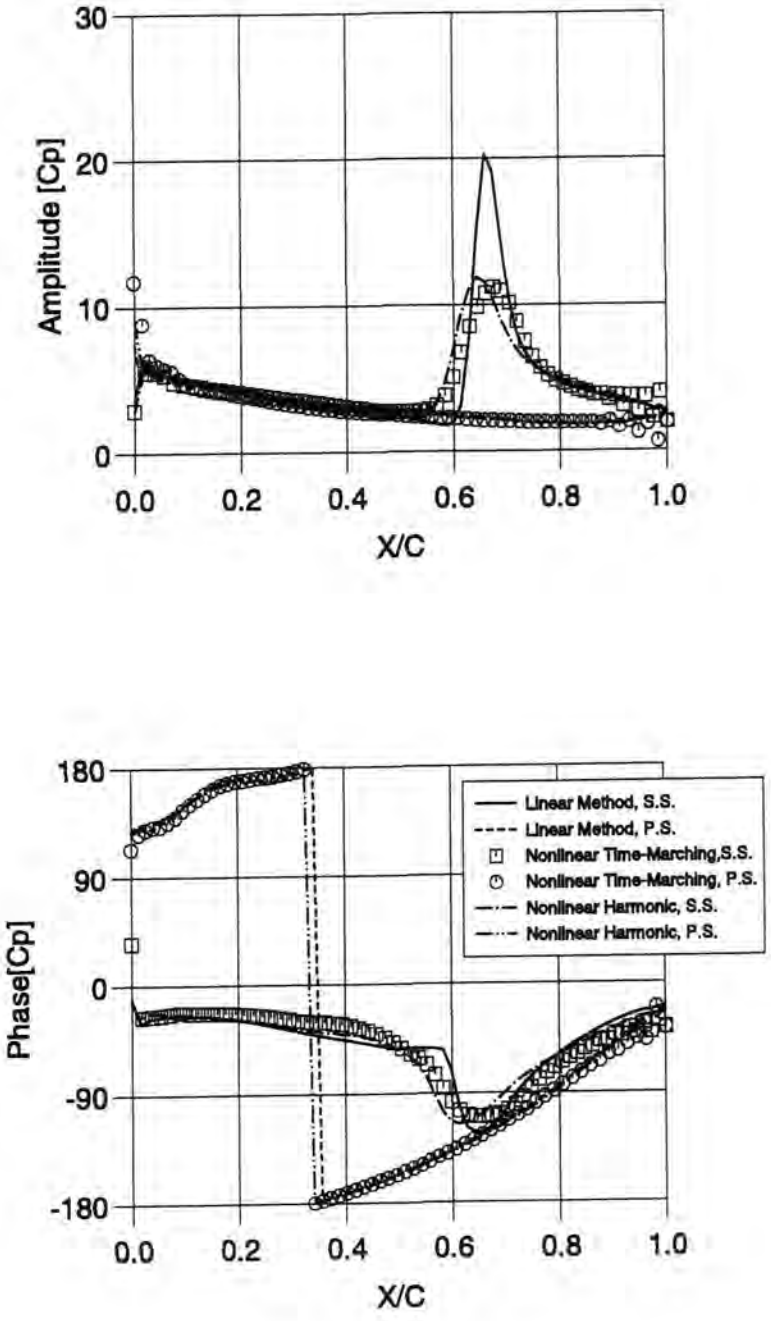

Fig. 5-28 Amplitude and Phase Distributions of Unsteady Pressure Coefficients on a Compressor Blade

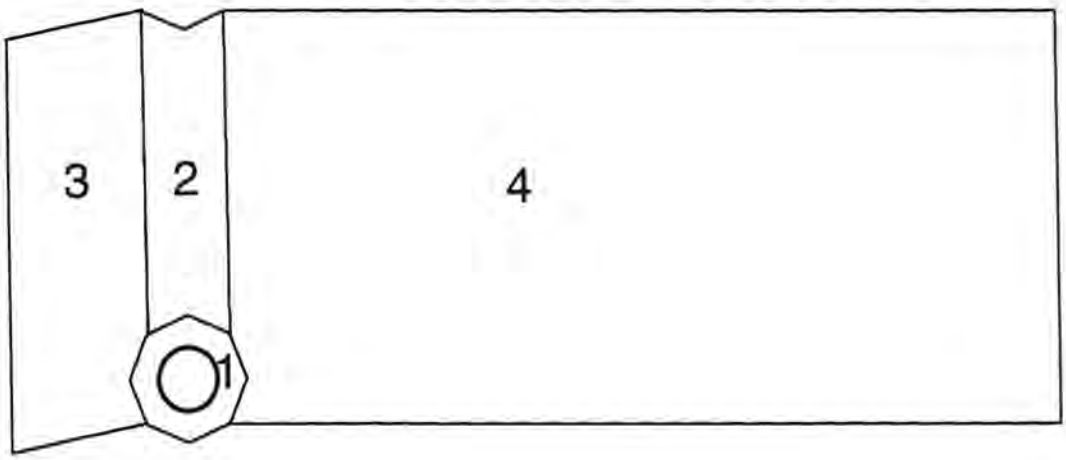

Fig. 6-1 Layout of 4-Block Mesh around a Circular Cylinder

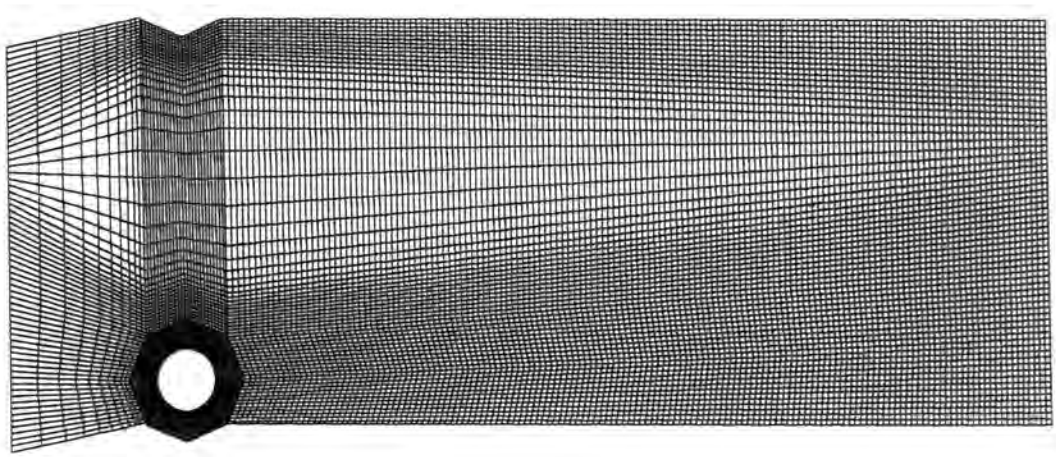

Fig. 6-2 Computational Mesh for a Circular Cylinder

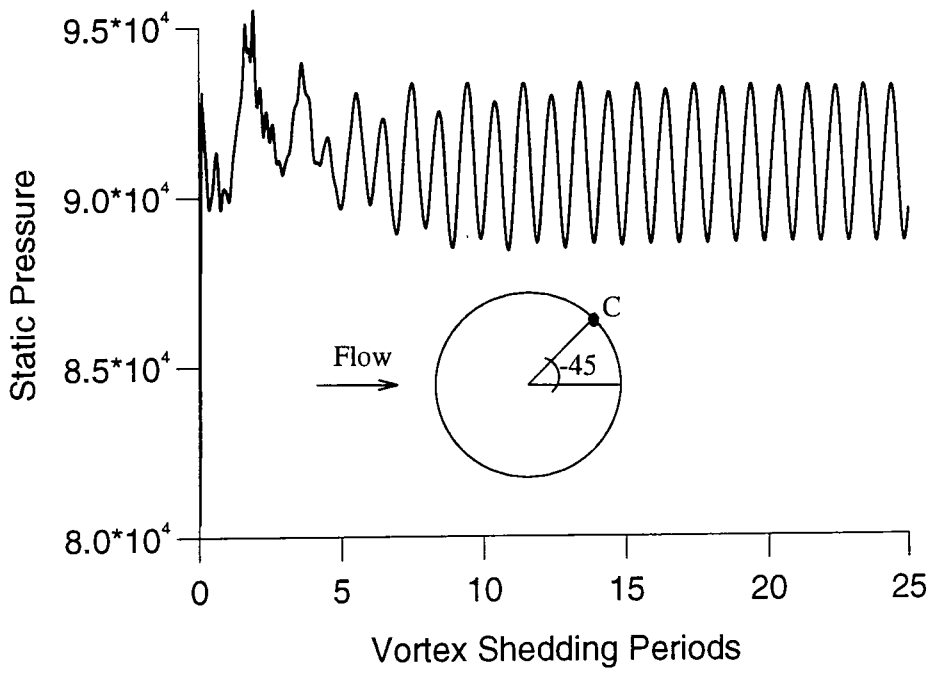

Fig. 6-3 Instantaneous Static Pressure History at Point C

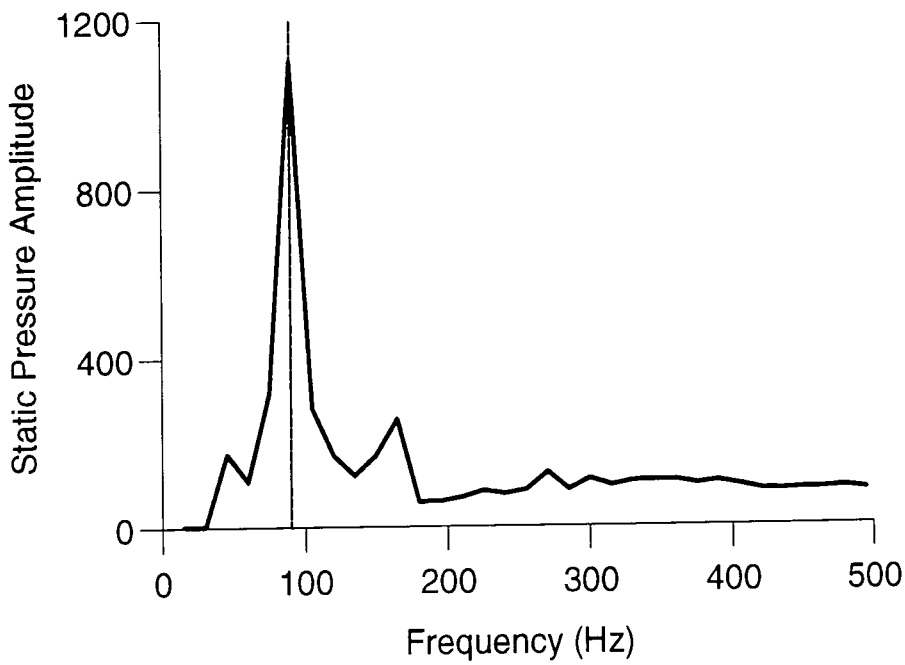

Fig. 6-4 Unsteady Pressure Frequency Spectrum at Point C

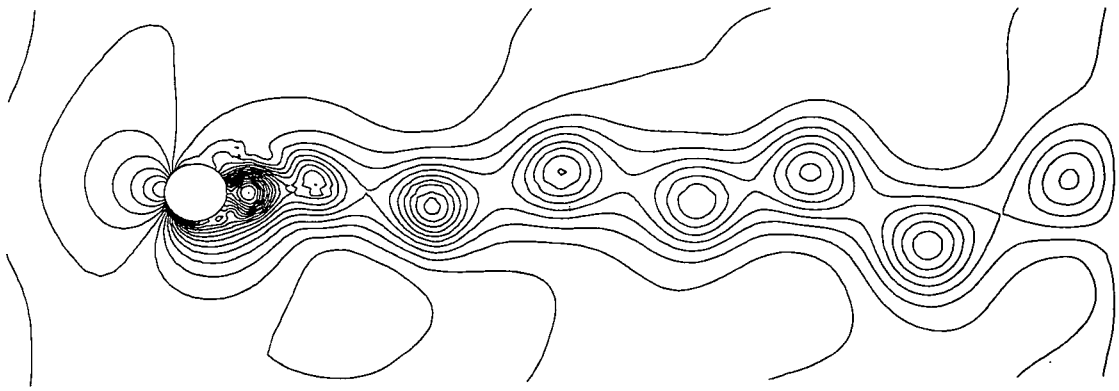

Fig. 6-5 Contours of Instantaneous Static Pressure around Cylinder

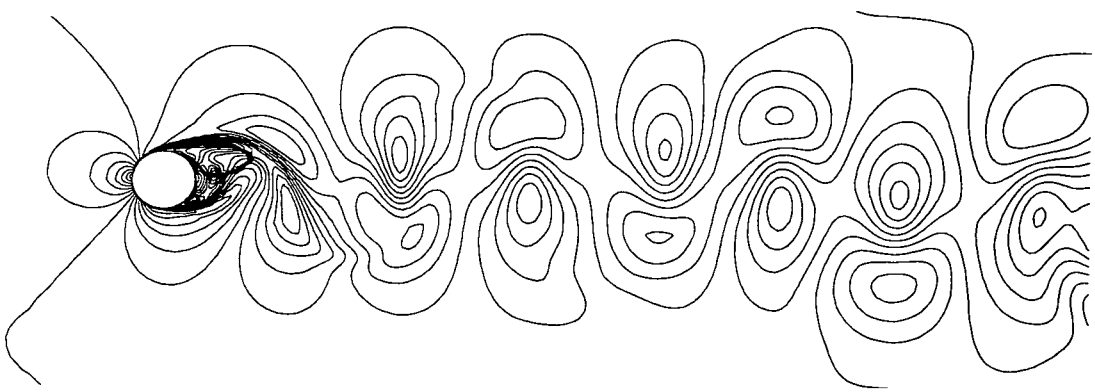

Fig. 6-6 Contours of Instantaneous Mach Number around Cylinder

Fig. 6-7 Contours of Instantaneous Entropy around Cylinder

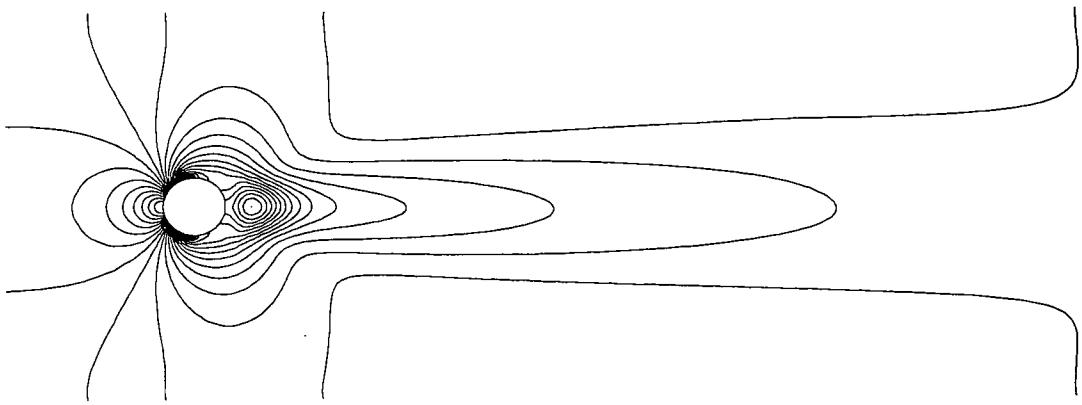

Fig. 6-8 Contours of Time-averaged Static Pressure around Cylinder

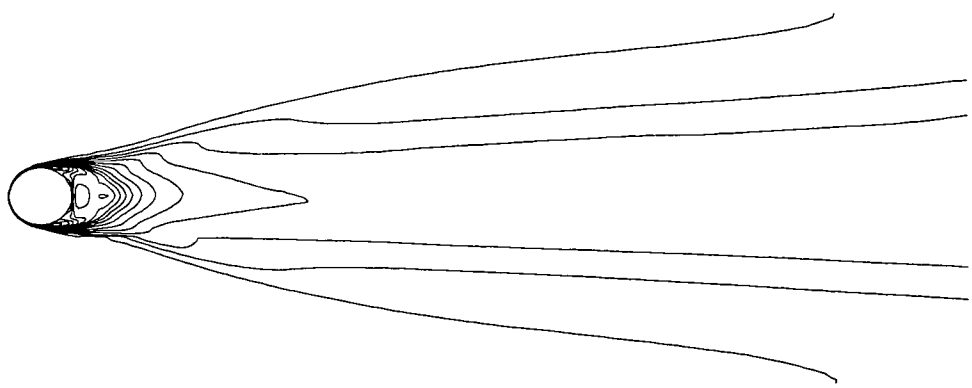

Fig. 6-9 Contours of Time-averaged Entropy around Cylinder

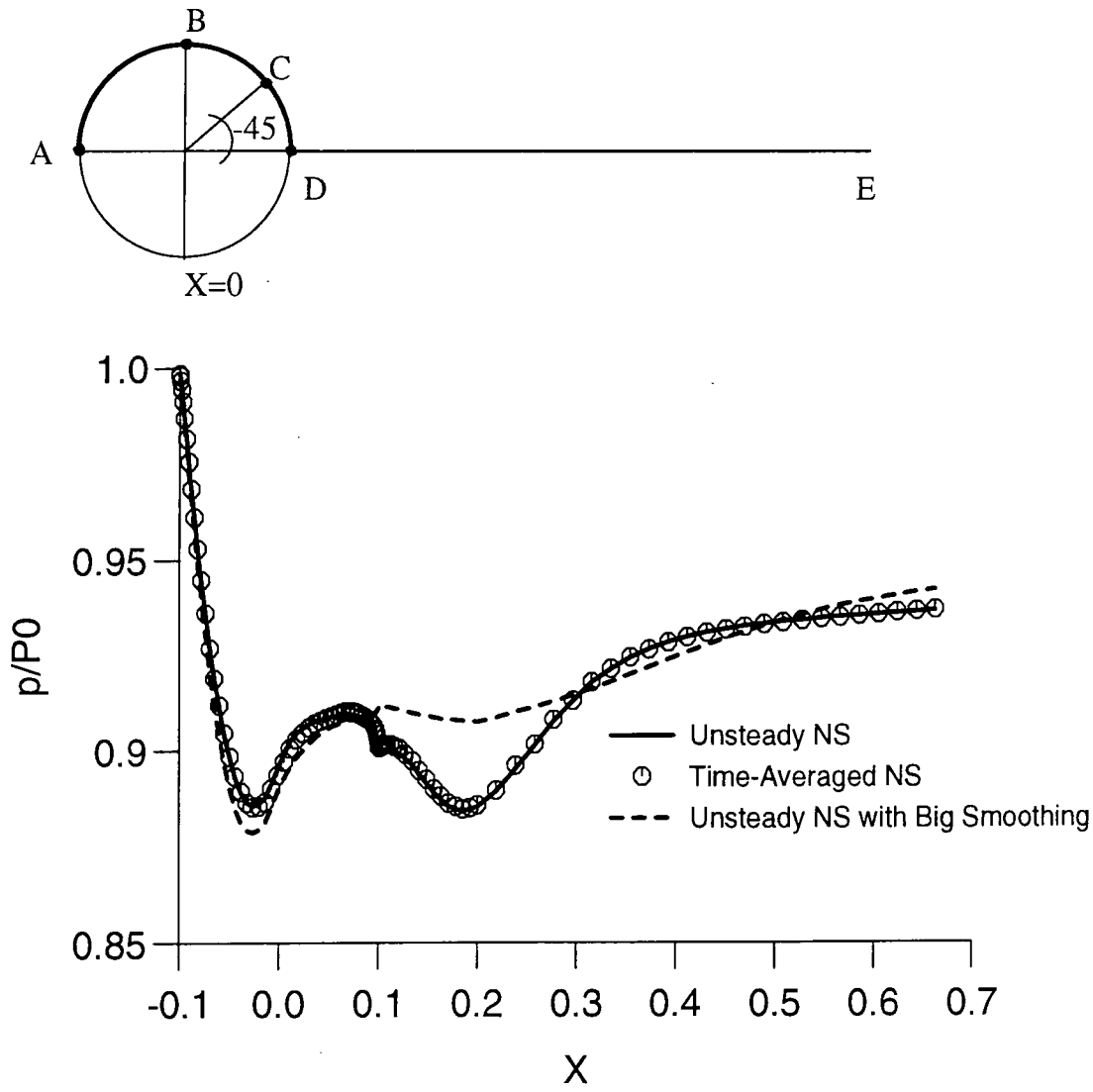

Fig. 6-10 Static Pressure Distribution along Line A-B-C-D-E

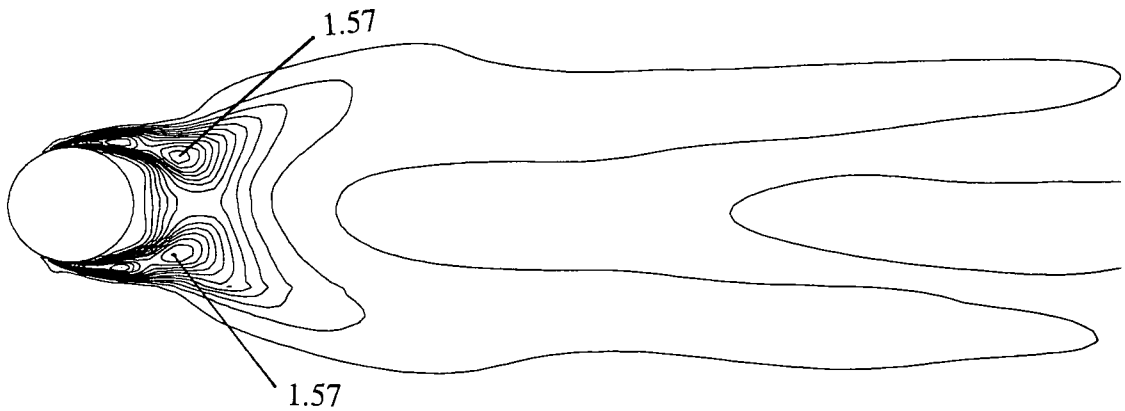

Fig. 6-11 Contours of Unsteady Stress $\overline{(\rho u)'u'}$ around Cylinder

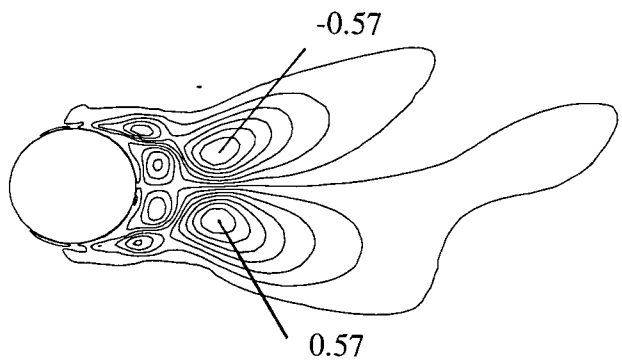

Fig. 6-12 Contours of Unsteady Stress $\overline{(\rho u)'v'}$ around Cylinder

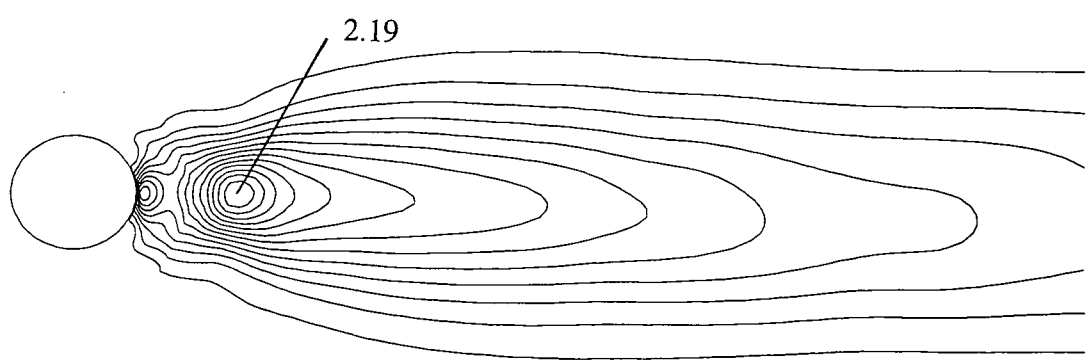

Fig. 6-13 Contours of Unsteady Stress $\overline{(\rho v)'v'}$ around Cylinder

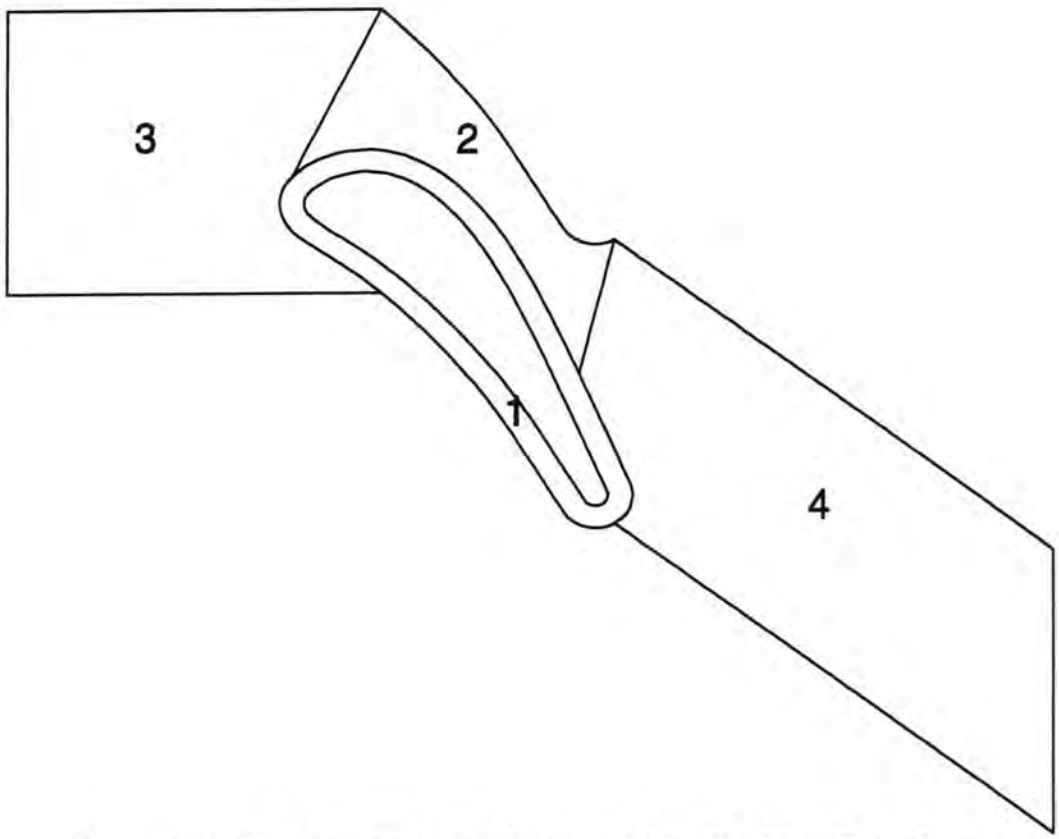

Fig. 6-14 Layout of 4-Block Mesh around VKI Turbine Cascade

Fig. 6-15 Computational Mesh around VKI Turbine Cascade

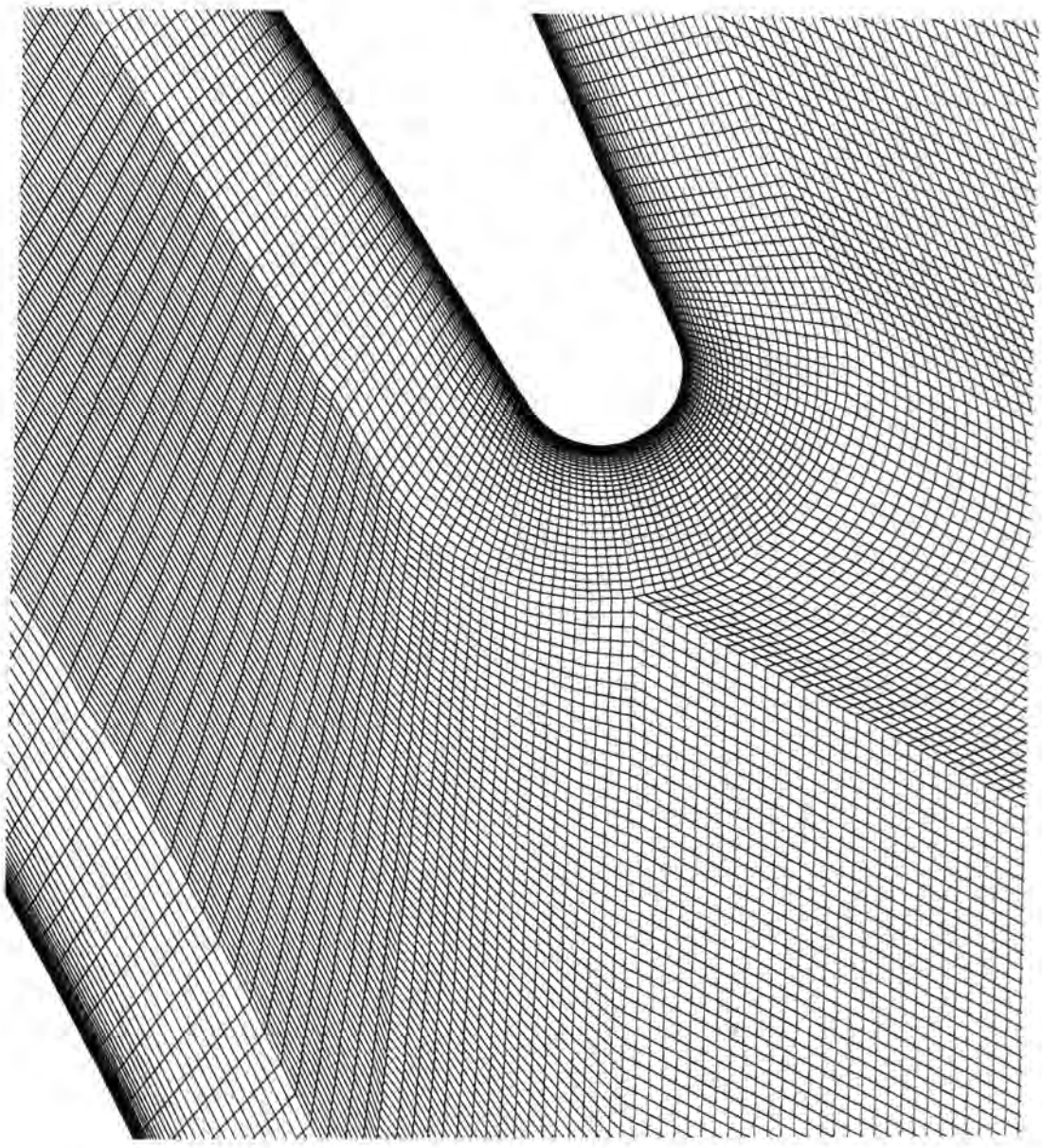

Fig. 6-16 Enlarged View of Computational Mesh around VKI Turbine Blade Trailing Edge

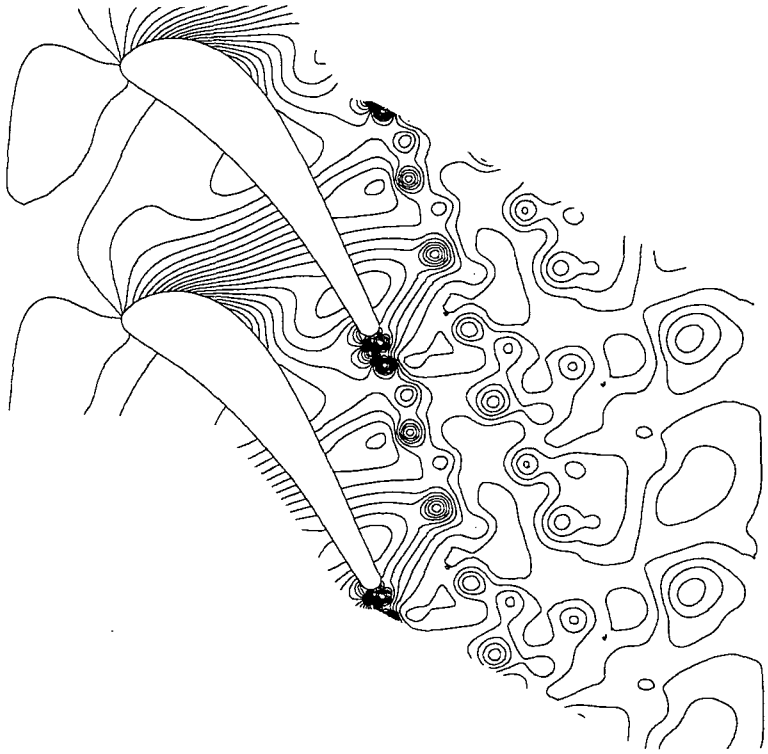

Fig. 6-17 Contours of Instantaneous Static Pressure around Turbine Cascade in a Laminar Flow Case

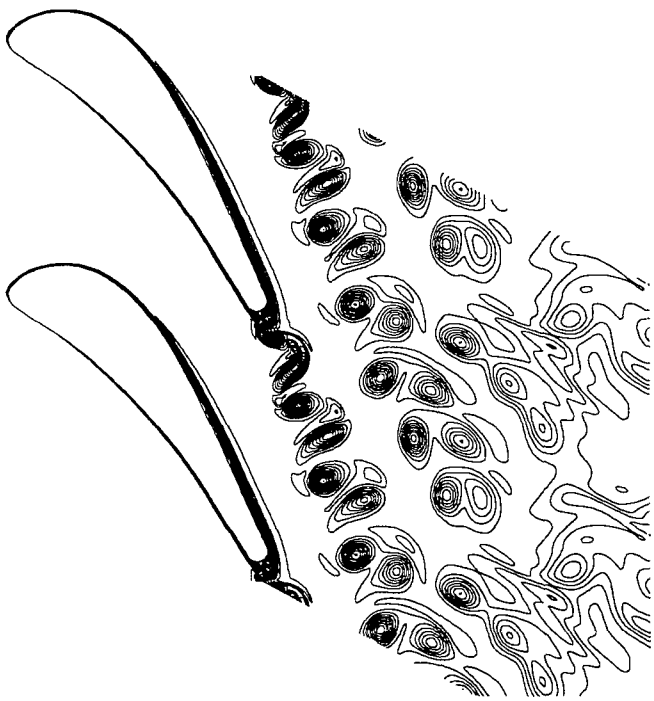

Fig. 6-18 Contours of Instantaneous Entropy around Turbine Blade in a Laminar Flow Case

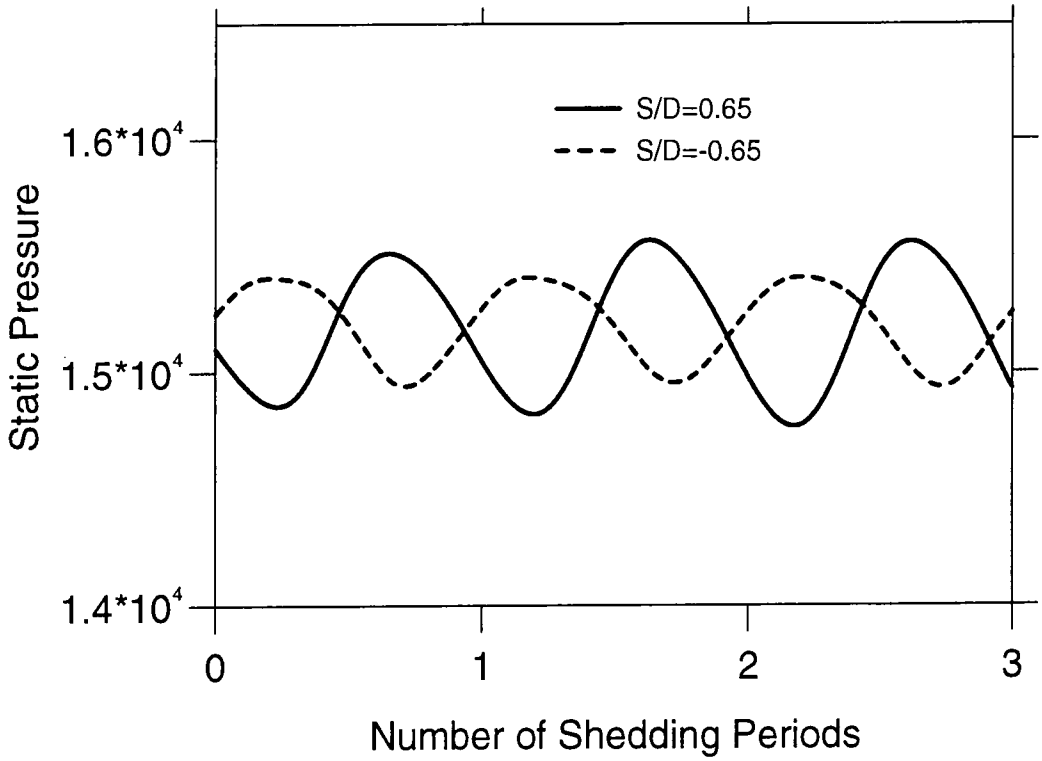

Fig. 6-19 Static Pressure Time Traces at Blade Trailing Edge

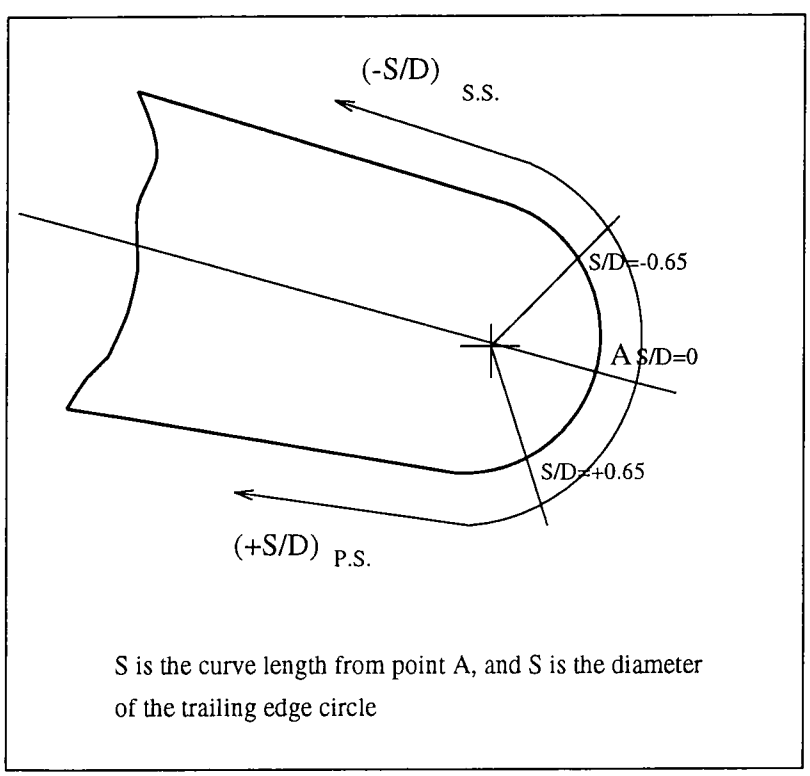

Fig. 6-20 Trailing Edge Reference Coordinate of VKI Turbine Blade

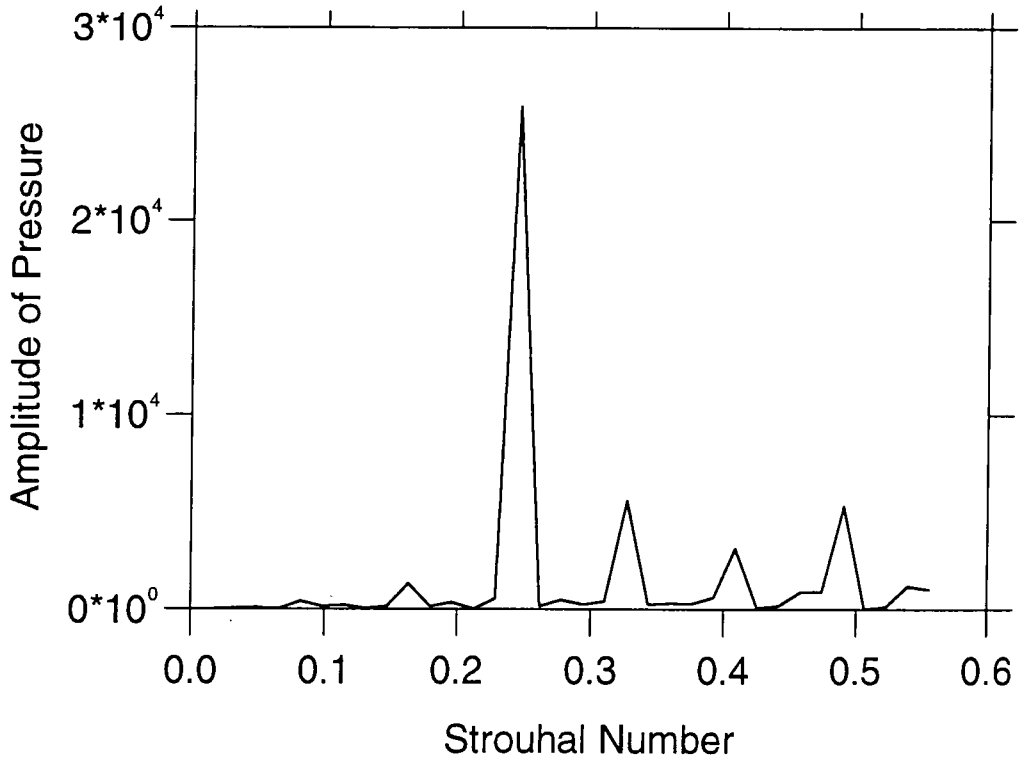

Fig. 6-21 Unsteady Pressure Frequency Spectrum at Blade Trailing Edge

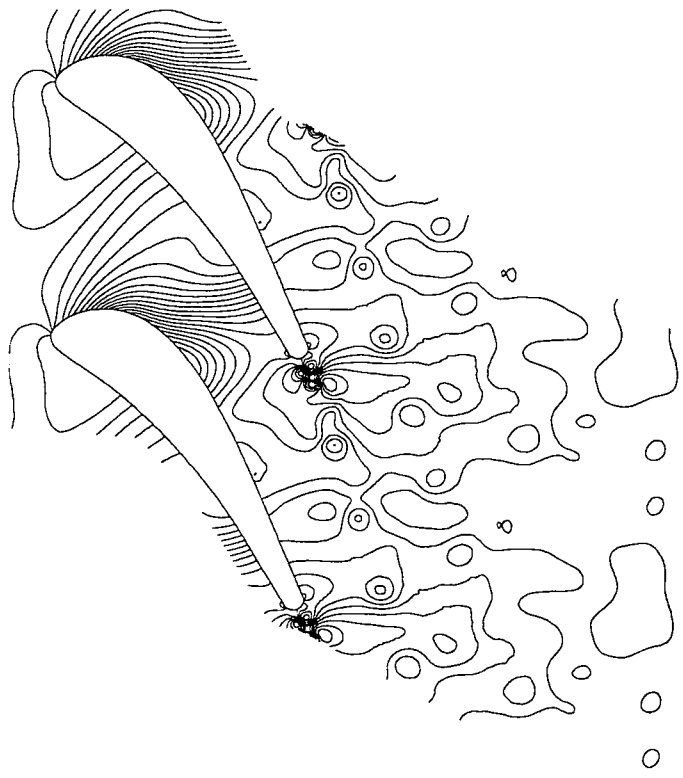

Fig. 6-22 Contours of Instantaneous Static Pressure around Blade in a Turbulent Flow Case

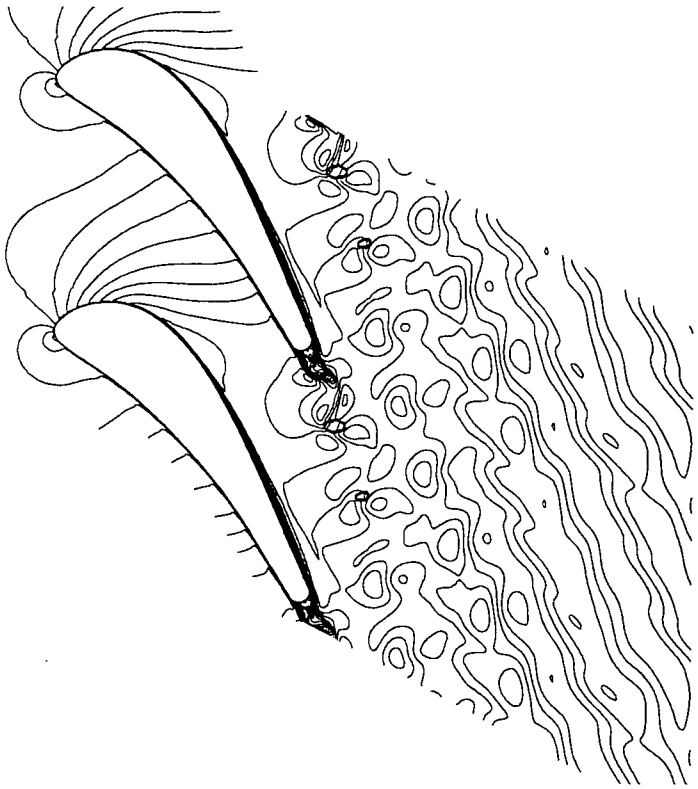

Fig. 6-23 Contours of Instantaneous Mach Number around Blade in a Turbulent Flow Case

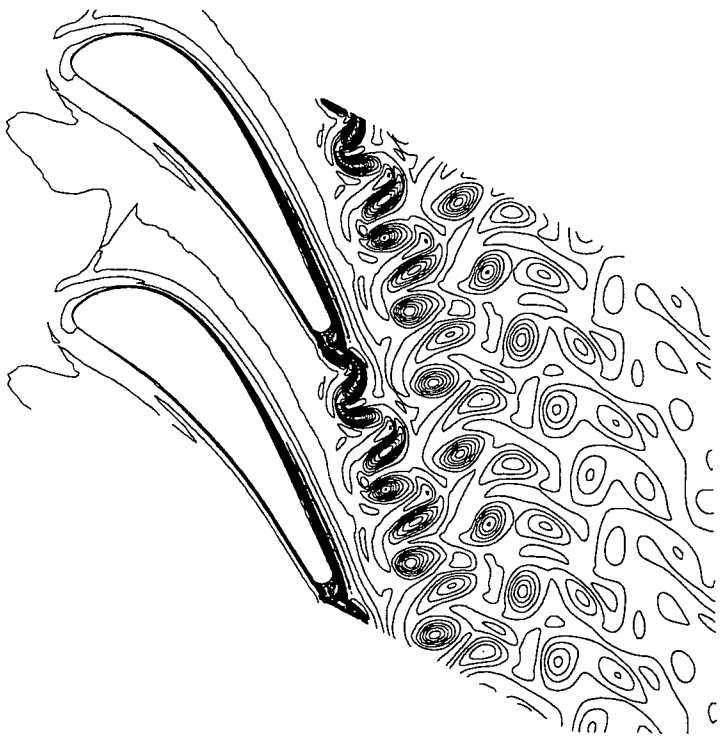

Fig. 6-24 Contours of Instantaneous Entropy around Blade in a Turbulent Flow Case

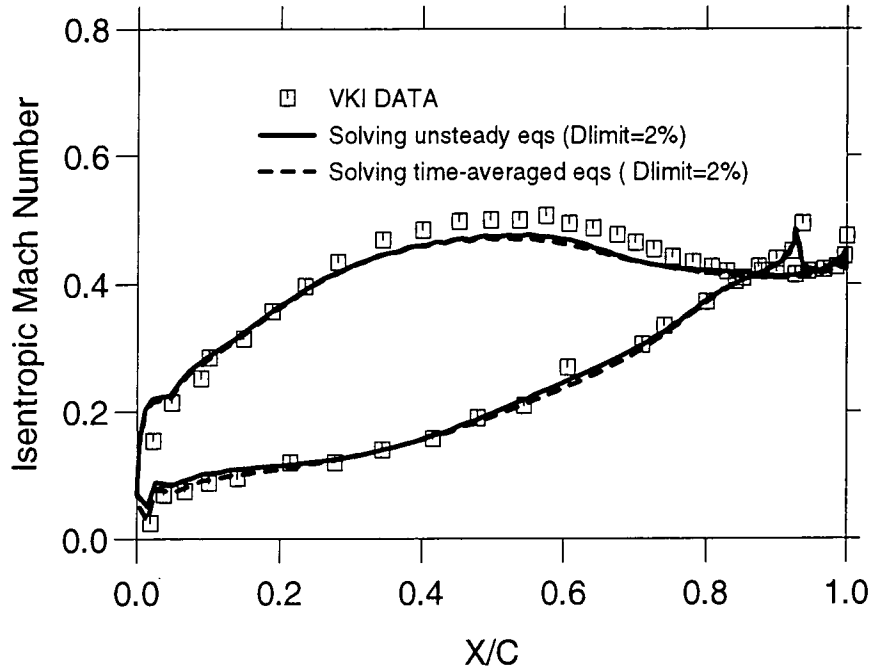

Fig. 6-25 Isentropic Mach Number Distribution on VKI Turbine Blade

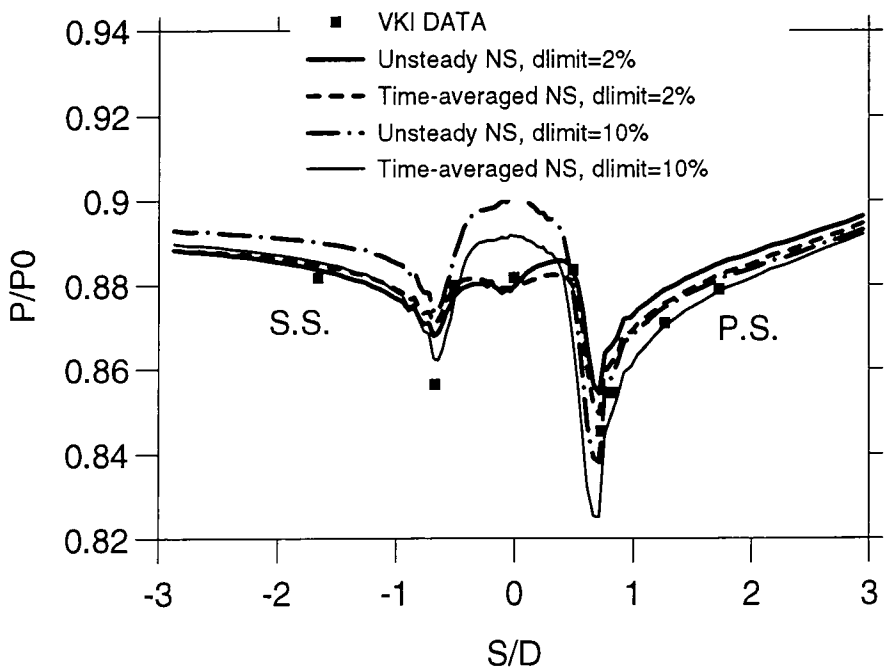

Fig. 6-26 Static Pressure Distribution around Blade Trailing Edge

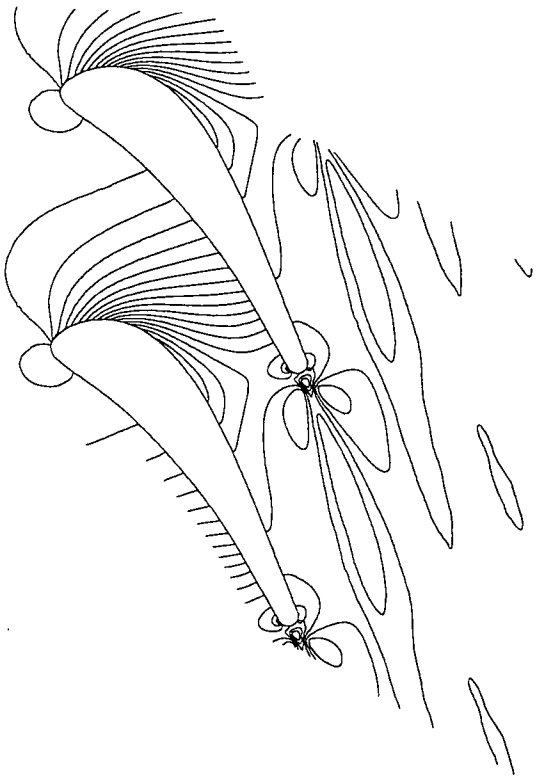

Fig. 6-27 Contours of Time-averaged Static Pressure by Solving Unsteady NS Equations (without Unsteady Stresses)

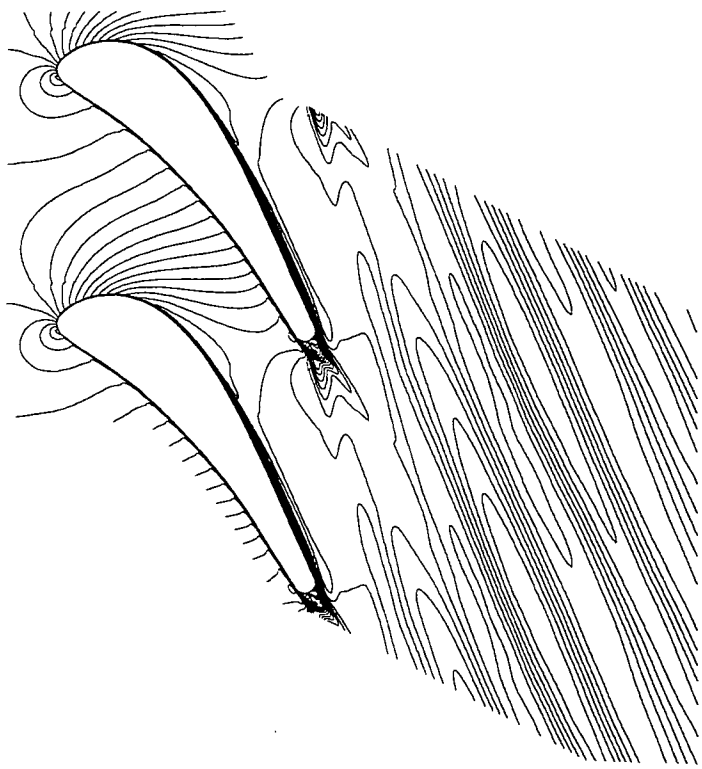

Fig. 6-28 Contours of Time-averaged Static Pressure by Solving Unsteady NS Equations (without Unsteady Stresses)

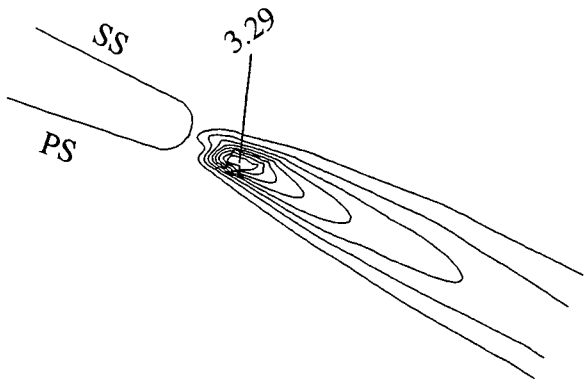

Fig. 6-29 Contours of Unsteady Stress $\overline{(\rho u)'u'}$ of Turbulent Vortex Shedding

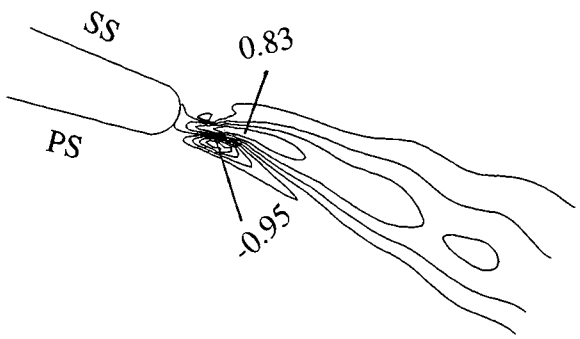

Fig. 6-30 Contours of Unsteady Stress $\overline{(\rho u)'v'}$ of Turbulent Vortex Shedding

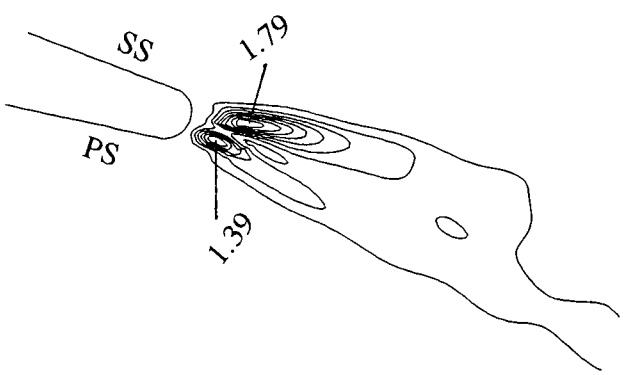

Fig. 6-31 Contours of Unsteady Stress $\overline{(\rho v)'v'}$ of Turbulent Vortex Shedding

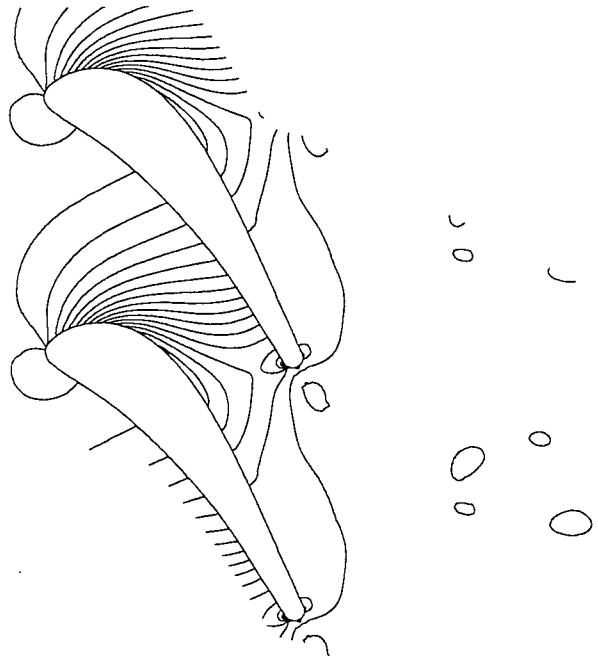

Fig. 6-32 Contours of Static Pressure by Solving Unsteady NS Equation (Dlimit =10%)

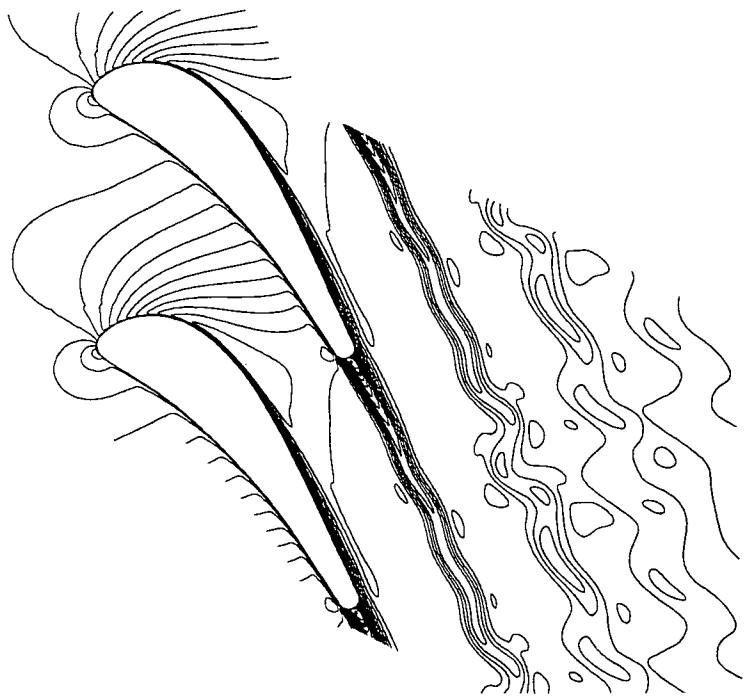

Fig. 6-33 Contours of Mach Number by Solving Unsteady NS Equation (Dlimit =10%)

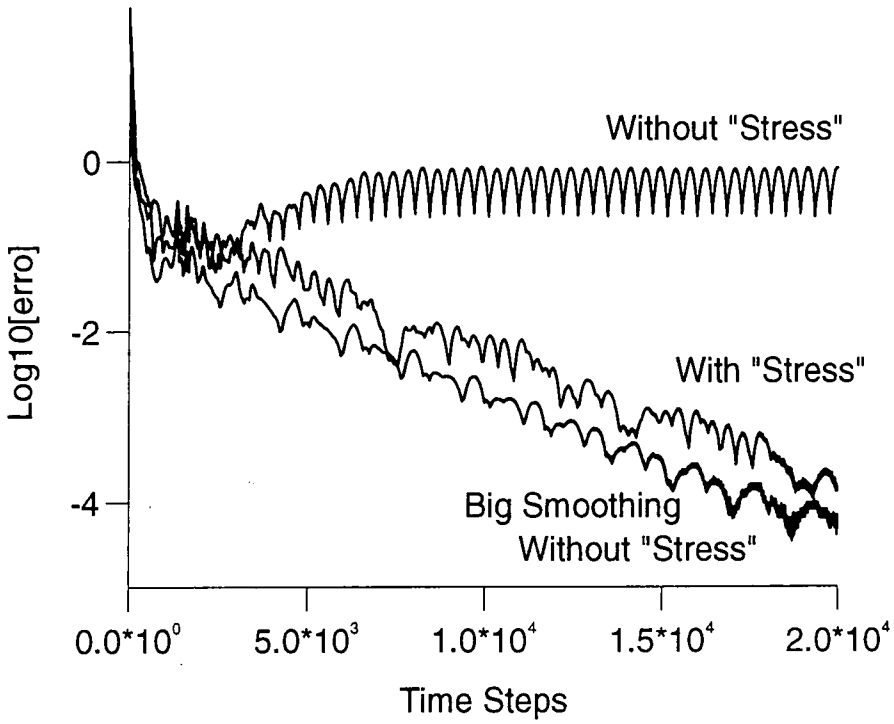

Fig. 6-34 Computational Residual History in Circular Cylinder Case

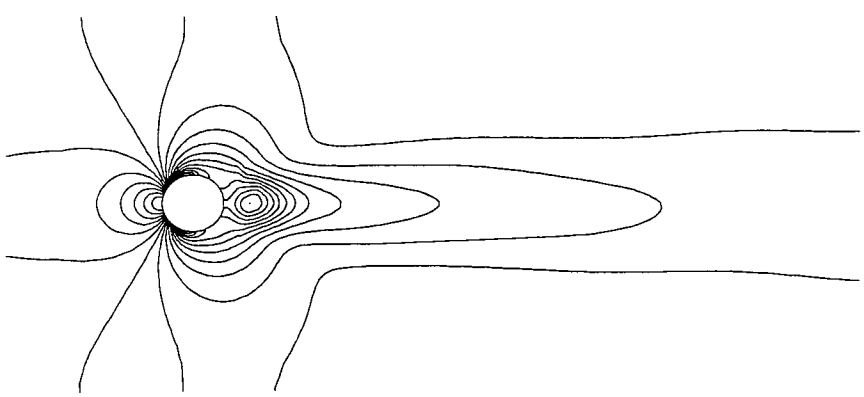

Fig. 6-35 Contours of Static Pressure by Solving Time-averaged Equations

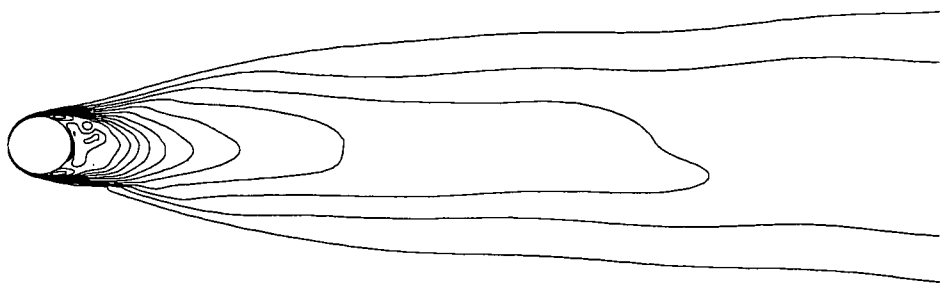

Fig. 6-36 Contours of Entropy by Solving Time-averaged Equation

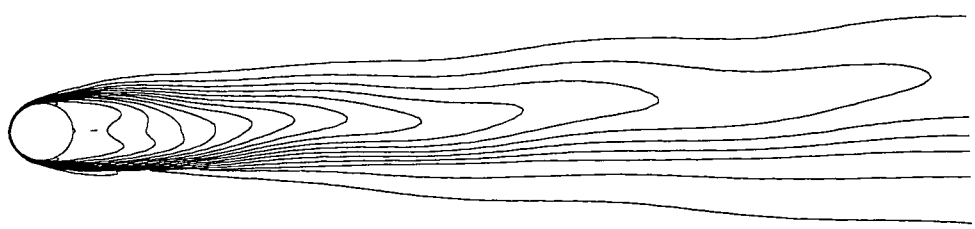

Fig. 6-37 Contours of Entropy by Solving Unsteady NS Equations with Big Artificial Smoothing Coefficients

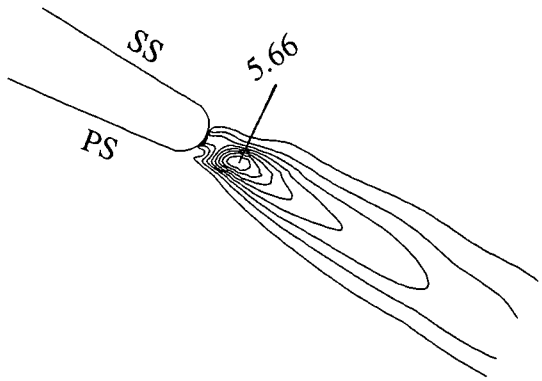

Fig. 6-38 Contours of Unsteady Stress $\overline{(\rho u)'u'}$ of Laminar Vortex Shedding

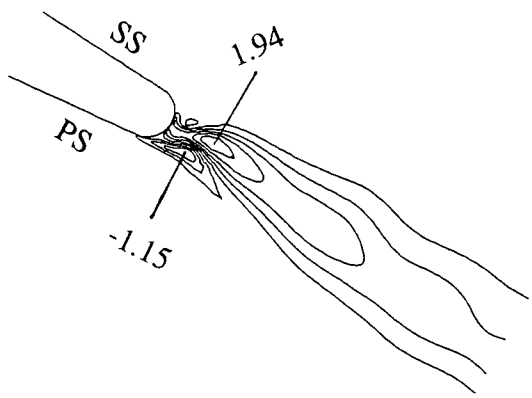

Fig. 6-39 Contours of Unsteady Stress $\overline{(\rho u)'v'}$ of Laminar Vortex Shedding

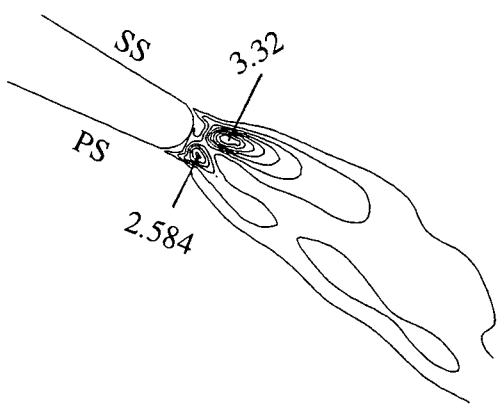

Fig. 6-40 Contours of Unsteady Stress $\overline{(\rho v)'v'}$ of Laminar Vortex Shedding

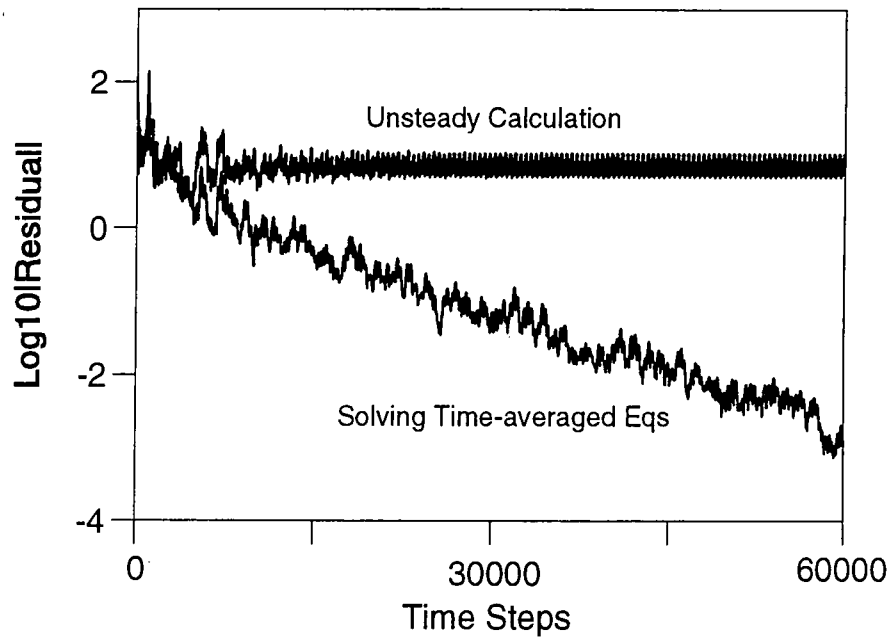

Fig. 6-41 Convergence History of Laminar Flow Case

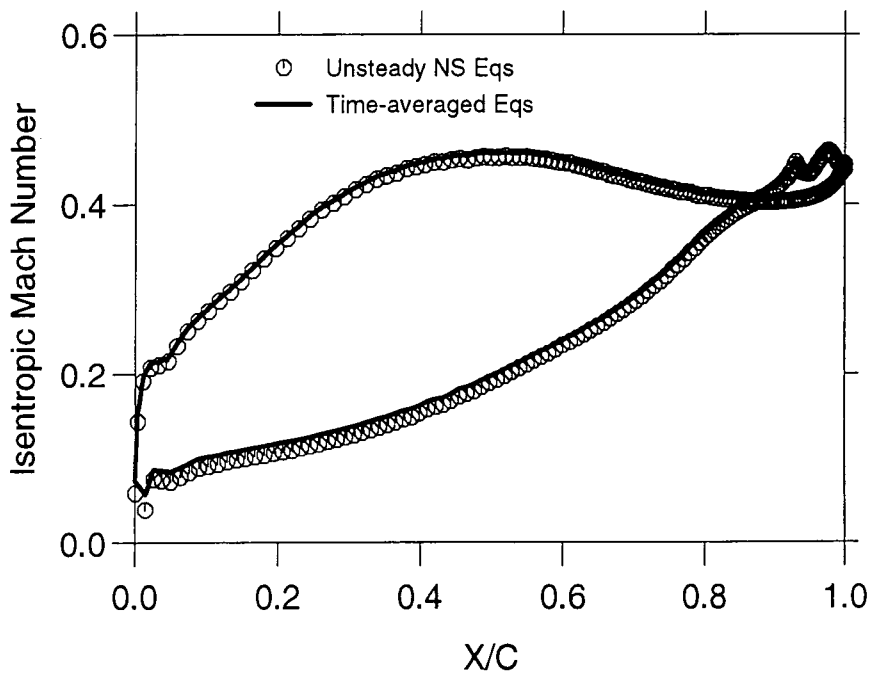

Fig. 6-42 Isentropic Mach Number Distribution on Blade Surface in Laminar Flow Case

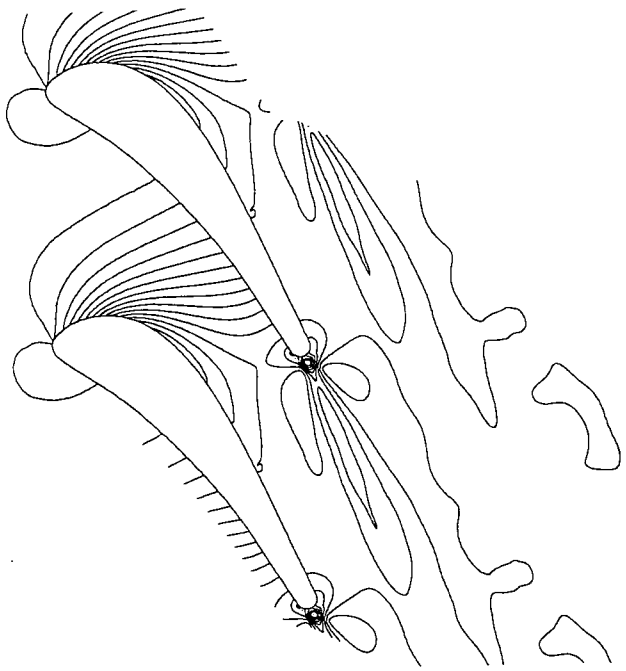

Fig. 6-43 Contours of Static Pressure by Solving Time-averaged NS Equations for Laminar Flow Case

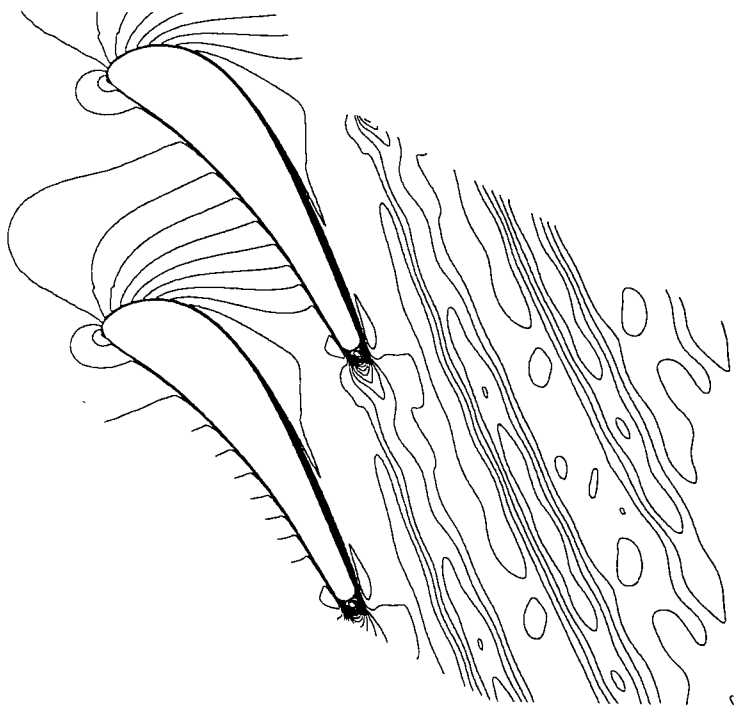

Fig. 6-44 Contours of Mach Number by Solving Time-averaged NS Equations for Laminar Flow Case

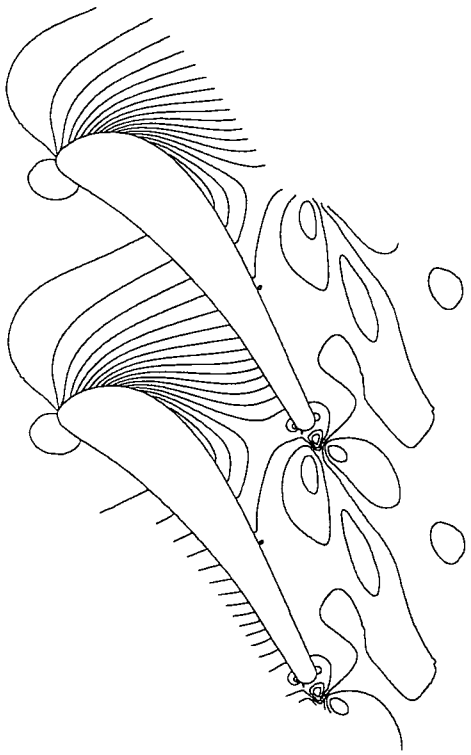

Fig. 6-45 Contours of Static Pressure by Solving Time-averaged NS Equations for Turbulent Flow Case

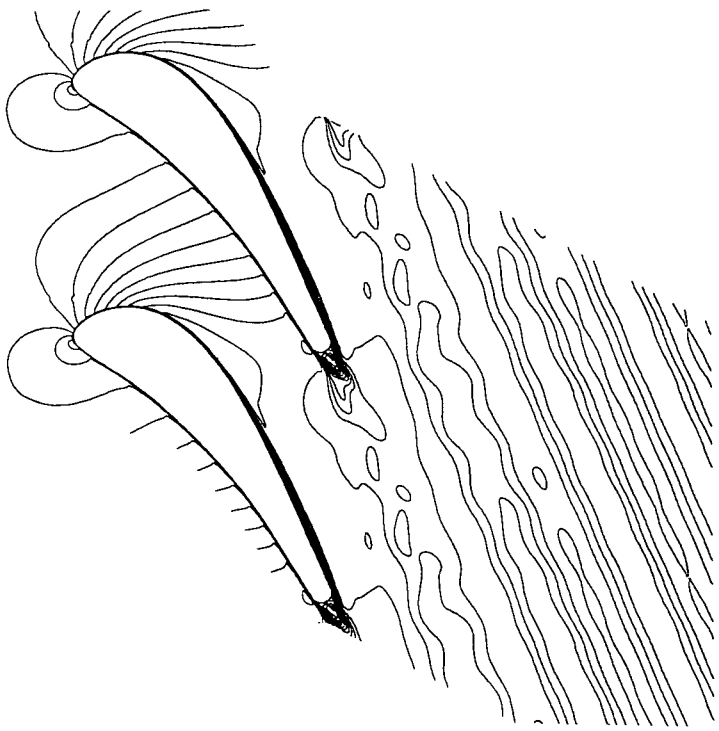

Fig. 6-46 Contours of Mach Number by Solving Time-averaged NS Equations for Turbulent Flow Case